ISSN number 0971 - 9709

The Journal of Indian Geophysical Union

AN OPEN ACCESS BIMONTHLY JOURNAL OF IGU

VOLUME 23, ISSUE 4, I July 2019

EDITORIAL OFFICE

Indian Geophysical Union, NGRI Campus, Uppal Road, Hyderabad- 500 007
Telephone: +91 -40-27012799; 27012734; Telefax:+91-04-27171564
E. mail: jigu1963@gmail.com, website: www.j-igu.in

The Open Access Journal with six issues in a year publishes articles covering
Solid Earth Geosciences; Marine Geosciences; and Atmospheric, Space and Planetary Sciences.

Annual Subscription

Individual ₹ 1000 per issue and Institutional ₹ 5000 for six issues

Payments should be sent by DD drawn in favour of "The Treasurer, Indian Geophysical Union", payable at Hyderabad, Money Transfer/NEFT/RTGS (Inter-Bank Transfer), Treasurer, Indian Geophysical Union, State Bank of India, Habsiguda Branch, Habsiguda, Uppal Road, Hyderabad- 500 007
A/C: 52191021424, IFSC Code: SBIN0020087, MICR Code: 500002318, SWIFT Code: SBININBBHO9.

For correspondence, please contact, Hon. Secretary, Indian Geophysical Union, NGRI Campus, Uppal Road, Hyderabad - 500 007, India; Email: igu123@gmail.com; Ph: 040 27012799, 272012734

ISSN: 0257-7968 (Clarivate Analytics)
ISSN: 0971-9709 (NISCAIR)
Approved as bimonthly ESCI journal by Clarivate Analytics
Cited in Indian Citation Index (ICI), New Delhi
Evaluated by NISCAIR, New Delhi

CONTENTS

Research Articles

Estimating subsurface petro-physical properties from raw and conditioned seismic reflection data: A comparative study

Prabodh Kumar Kushwaha[1*], S.P. Maurya[2], N.P. Singh[2] and Piyush Rai[1]
[1]Department of Mining Engineering, Indian Institute of Technology (BHU), Varanasi-221005, India
[2]Department of Geophysics, Institute of Science, Banaras Hindu University, Varanasi-221005, India
*Corresponding author: prabodhkk.rs.min15@itbhu.ac.in

ABSTRACT

The data conditioning plays an important role in simultaneous seismic inversion process as in some cases, it improves the resolution of the inverted results, while in other cases, it degrades the solution dramatically. Therefore, it needs to be studied carefully. The objective of the present study is to quantify the advantages of performing pre-stack data conditioning, prior to estimation of subsurface petro-physical parameters. In present study, a very simple and straight forward method of testing the effects of data conditioning on simultaneous inversion, have been chosen and inversion is performed over the original processed gathers, as well as the conditioned gathers to measure the difference in intermediate steps of the workflow. In this regard, initially, one trace is inverted and compared with original curve from well log to test the algorithm. The correlation between the two is estimated to be 0.82 for raw gather and 0.87 for conditioned gather. Further, the entire seismic volume is inverted for impedance, density and lamé parameters in inter well region, thereafter, and the cross plots between inverted section are computed. The results of the analysis indicate that the reservoir is devoid of hydrocarbon. The analysis depict that the inversion of conditioned data produces a result, which is of more valuable to an interpreter as compared to the inversion of raw gather.

Keywords: Acoustic Impedance, Seismic Processing, Data Conditioning, Hydrocarbon, Scotian Basin (Canada)

INTRODUCTION

Seismic inversion methods have been widely used to locate potential oil and gas reservoirs, as well as to provide information on the physical properties of the reservoir rocks. Changes in physical properties of the rock such as density, seismic acoustic impedance, cause a significant influence that could be observed in a high quality seismic data. Earlier, only post-stack seismic inversion method was used routinely to estimate acoustic impedance (P- impedance) and characterize the reservoir. However, this approach gives insufficient information about the reservoir, since P- impedance alone is unable to distinguish the effects between lithology and fluid content. Fortunately, this limitation has been overcome by extracting information from the shear impedance (S-impedance) seismic data, to describe the fluid content of the area in a precise manner (Maurya et al., 2018, 2019).

Presently with the advent of new technologies, the prime aim is to increase the resolution of seismic inversion by increasing the signal to noise ratio of seismic gather. Therefore, some researchers tried to use pre-conditioning of gather for improving the signal to noise ratio. However, some other researchers (Chopra and Sharma, 2016; Singleton, 2009) have shown that the pre-conditioning technique degrades inversion results significantly. Therefore, the present study is aimed to demonstrate the effect of data conditioning on simultaneous inversion method for the seismic data from Penobscot, Canada.

The simultaneous inversion method estimates P-impedance, S-impedance, density, V_P/V_S ratio by inverting each partial angle stack data simultaneously, using the extracted wavelet from each angle stack. The inversion results such as Density (ρ), Lambda-rho ($\lambda\rho$) (Incompressibility), and Mu-rho ($\mu\rho$) (Rigidity) are proven useful for reservoir characterization of the prospective area.

The purpose of pre-stack simultaneous inversion is to obtain reliable estimation of P-wave velocity (V_P), S-wave velocity (V_S), and density (ρ) for predicting the fluid and lithological property of Earth is subsurface.

Simmons and Backus (1996) inverted the linearized P-reflectivity (R_P), S-reflectivity (R_S) and density reflectivity (R_D), where

$$R_P = \frac{1}{2}\left[\frac{\Delta V_P}{V_P} + \frac{\Delta \rho}{\rho}\right] \quad (1)$$

$$R_S = \frac{1}{2}\left[\frac{\Delta V_S}{V_S} + \frac{\Delta \rho}{\rho}\right] \quad (2)$$

$$R_D = \frac{\Delta \rho}{\rho} \quad (3)$$

The reflectivity, as given in eqs. 1-3 can be approximated from the Aki-Richards equation which is angle dependent R(θ) (Richards and Frasier, 1976; Maurya and Sarkar, 2016). Density (ρ) and P-wave velocity (V_P) may be associated with the Gardner's relationship (a=0.31, m=0.25; Gardner et al., 1974), as following.

$$\frac{\Delta \rho}{\rho} = \frac{1}{4}\frac{\Delta V_P}{V_P}, \quad (4)$$

On the other hand, the P-wave velocity and S-wave velocity is related to each other by Castagna's equation (Castagna et al., 1985; Maurya and Singh, 2017) in the following way.

$$V_P = 1.16V_S + 1360 \quad (5)$$

Various inversion techniques for evaluating and interpreting reflection seismic data have been utilized since several decades. Some of them are based upon the Zoeppritz and Knott equation (Shuey, 1985; Maurya and Singh, 2015) which has been modified, and Aki and Richards, (1980), give the most common incarnation. This modification reduced 16 equations with 16 unknown parameters to a single equation with three unknown parameters of Knott-Zoeppritz under some assumptions.

In this study, the attempt is made to describe the effect of data conditioning on pre-stack inversion of seismic data from the Penobscot area of Scotian Basin, Canada.

STUDY AREA

The Penobscot area of Scotian Basin (Canada) covers an area of 90.27 km^2 with sediment depth reaching up to 18 km. The survey was conducted in 1992.The seismic data covers an area of 66 km^2 and was acquired in a 12.5 m by 25 m (inline by cross-line) bin size with 60-fold coverage and 2 ms sampling rate. Geologically, the Scotian Basin evolved in the Triassic Period. When the North American plate separated from the African plate, after the break-up of Pangaea, it created interconnected rift basins, including the Scotian Basin. Figure 1 gives better description of the geology of Scotian Basin (Mandal and Srivastava, 2018). The bandwidth of seismic data is 08-40 Hz. In this region, the well Penobscot L-30 was drilled to a depth of 4237m. The Lower Logan Canyon sands in L-30 were considered oil bearing (minor accumulation). In this work, the available seismic data are pre-stack offshore 3Ddata. The seismic survey coverage ranges from Inline 1000 to 1600 and X-line 1161 to 1200 for each volume. The angle stacks (0° - 30°, post-stack) are used. This stack is loaded as post-stack data into the Hampson Russell Software (HRS), before creating pseudo gathers (pre-stack) by extracting a trace from each volume. This seismic loading workflow definitely differs from the conventional workflow of simultaneous inversion, where pre-stack volume is created from given post-stack volumes. A complete well log data per well is needed before proceeding with the simultaneous inversion. The essential data required for the inversion workflow are P-wave sonic, S-wave sonic, density and check shot logs. The cross plot approach is being applied on the L-30 well in order to determine the feasibility of the simultaneous seismic inversion process on the dataset, before proceeding to the full inversion workflow.

METHODOLOGY

In the present study the work of both Buland et al., (1996), Simmons and Backus (2003), has been extended to build an approach that inverts P-impedance ($Z_P = \rho V_P$), S-impedance ($Z_S = \rho V_S$), and density (ρ) through an approximation similar to that of Buland and Omre (2003) and using constraints similar to Simmons and Backus (1996).

The Aki-Richards equation was redefining by (Fatti et al., 1994) for small angle (Niu et al., 2018) as

$$R(\theta) = c_1 R_P + c_2 R_S + c_3 R_D, \quad (6)$$

Where $c_1 = 1 + \tan^2\theta$, $c_2 = -8\gamma\sin^2\theta$, $c_3 = -0.5\tan^2\theta + 2\gamma\sin^2\theta$ and $\gamma = (V_S/V_P)^2$ and the three reflectivity terms are as per eqs. 1, 2 and 3 (Hampson et al., 2005).

For an angle trace $T(\theta)$ we can write

$$T(\theta) = \frac{1}{2}c_1 W(\theta) DL_P + \frac{1}{2}c_2 W(\theta) DL_S + \frac{1}{2}c_3 W(\theta) DL_D \qquad (7)$$

Where $L_S = \ln(Z_S)$ and $L_D = \ln(\rho)$. Eq. (7) could be used for inversion, except that it ignores the relationship between L_P with L_S and L_D. Since in this approach, we deal with impedance and take logarithms, our relationships are different than those given by Simmons and Backus (1996) and are given as

$$\ln(Z_S) = k\ln(Z_P) + k_C + \Delta L_S, \quad (8)$$

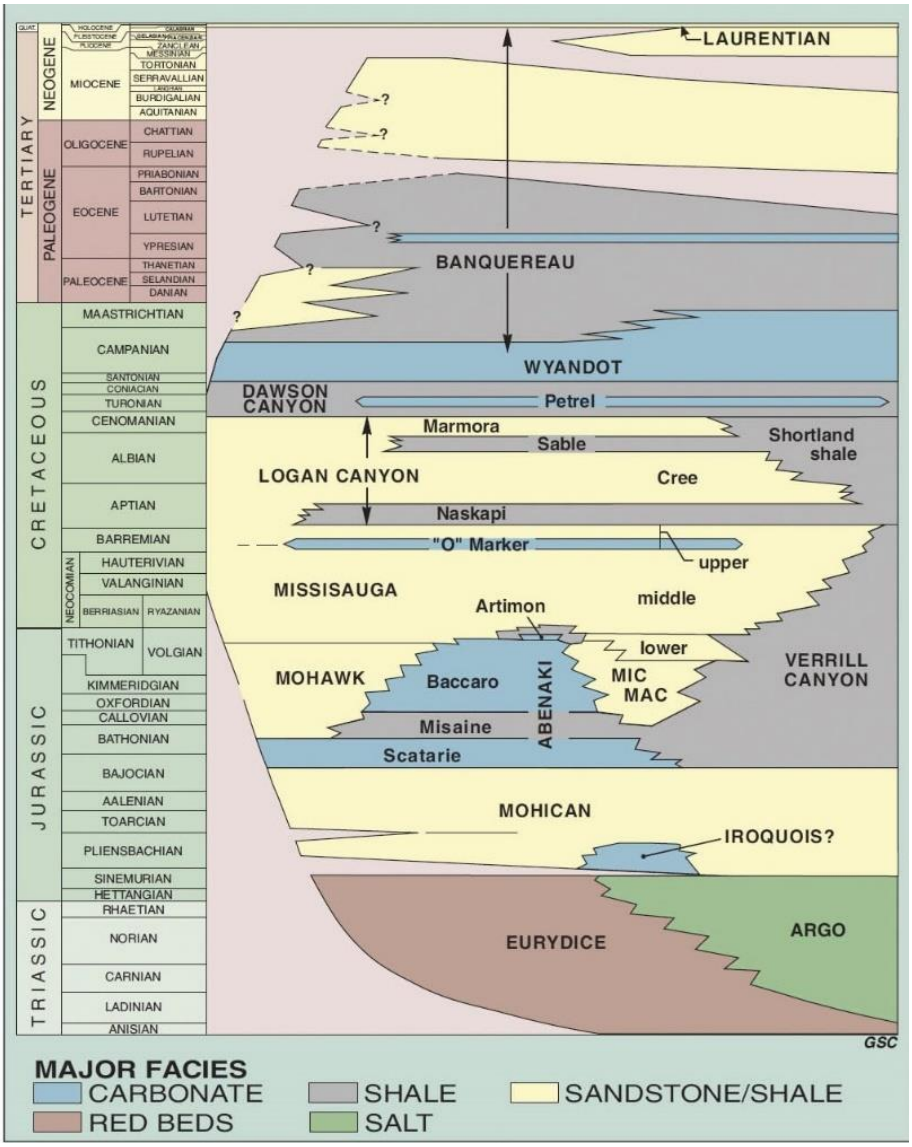

Figure 1. Stratigraphy of Scotian Basin (Mandal and Srivastava 2018).

$$\ln(Z_D) = m\ln(Z_P) + m_C + \Delta L_D, \quad (9)$$

Where coefficients (k, k_C, and m_C) are calculated using well log data in the area, ΔL_S and ΔL_D represent the deviation from background trend due to presence of hydrocarbons.

Now, the simultaneous inversion can be derived. Starting with Fatti's version of the Aki-Richards equations, these equations model the reflection amplitude as a function of incident angle. Using these equations and the previous relationships between the P-

impedance, S-impedance and density changes, the modified Fatti's equation is written as:

$$(\theta) = c'_1 W(\theta) DL_P + c'_2 W(\theta) DL_S + c'_3 W(\theta) DL_D \quad (10)$$

Where: $c'_1 = \frac{1}{2}c_1 + \frac{1}{2}kc_2 + mc_3$, $c'_2 = \frac{1}{2}c_2$, and $c'_3 = c_3$. $W(\theta)$ is the wavelet at angle θ, D is the differentiation derivative operator, and $L_P = \ln(Z_P)$.

Equation (10) can be written in this form of matrix

$$\begin{bmatrix} T(\theta_1) \\ T(\theta_2) \\ \vdots \\ T(\theta_N) \end{bmatrix} = \begin{bmatrix} c'_1(\theta_1)W(\theta_1)D & c'_2(\theta_1)W(\theta_1)D & c'_3(\theta_1)W(\theta_1)D \\ c'_1(\theta_2)W(\theta_2)D & c'_2(\theta_2)W(\theta_2)D & c'_3(\theta_2)W(\theta_2)D \\ \vdots & \vdots & \vdots \\ c'_1(\theta_N)W(\theta_N)D & c'_2(\theta_N)W(\theta_N)D & c'_3(\theta_N)W(\theta_N)D \end{bmatrix} \begin{bmatrix} L_P \\ \Delta L_S \\ \Delta L_D \end{bmatrix} \quad (11)$$

If eq. (11) is solved by matrix inversion methods, the problem of poor resolution of frequency component is encountered. So, a practical approach is to initialize the solution to $[\ L_P \ \ \Delta L_S \ \ \Delta L_D\ ]^T = [\log(Z_P)\ 0\ 0]^T$, where Z_P is the initial impedance model (Larsen, 1999).

In practice, pre-stack inversion involves the following steps:

Note that if the angle is zero then this equation reduces to zero-offset (model-based) inversion. In equation, we invert for L_P, L_S and L_D. In practice, simultaneous inversion involves the following steps by using the Hampson Russell Software (HRS):

1. From CMP gathers, we have the following information:
- A set of N angle traces;
- A set of N wavelets for each angle;
- Initial model values for Z_P.
2. Compute the coefficient values for k and m using well-log data.
3. Start with initial guess model.
   $[L_P \ \Delta L_S \ \Delta L_D]^T = [\log(Z_P)\ 0\ 0]^T$, (12)
4. Apply the inversion.
5. Compute the final values of Z_P, Z_S and ρ using eqs. 13-15.

$$Z_P = \exp(L_P), \quad (13)$$

$$Z_S = \exp(kL_P + k_C + \Delta L_S), \quad (14)$$

$$\rho = \exp(mL_P + m_C + \Delta L_D), \quad (15)$$

Note that the initial model guess representing the initial model of P-impedance, while ΔL_S and ΔL_D are initialized with zero values in this iteration (Maurya and Singh, 2015).

LAMBDA-MU-RHO (LMR TRANSFORM

The LMR (Lambda-mu-rho) transform was originally proposed by Goodway et al., 1997. LMR uses the following relationships between V_P, V_S, ρ and the Lamé parameters - Lambda (λ) and Mu(μ):

$$V_P = \sqrt{\frac{\lambda + 2\mu}{\rho}} \quad (16)$$

and

$$V_S = \sqrt{\frac{\mu}{\rho}} \quad (17)$$

Therefore

$$Z_S^2 = (\rho V_S)^2 = \mu\rho \quad (18)$$

and

$$Z_P^2 = (\rho V_P)^2 = (\lambda + 2\mu)\rho \quad (19)$$

So,

$$\lambda\rho = Z_P^2 - 2\,Z_S^2 \quad (20)$$

Through seismic inversion, the above equations express P-impedance and S-impedance in rock properties. Many scientists claim that λ and μ help to discriminate fluid effects from lithology effects. Further, the Lamé parameters are derived by extracting the P-wave and S-wave reflectivity from pre- stack seismic data and inverting them to P-wave and S-wave impedances (assuming that $V_P / V_S = 2$). Then μρ is estimated by $(V_S)^2$ and λρ is estimated by $(V_P)^2 - 2\mu\rho$.

DATA CONDITIONING

As mentioned before, data conditioning is very important step in simultaneous inversion method. Data conditioning improves signal to noise ratio and hence increases inversion resolution. The data conditioning is applied in the following way: First, if the data is in offset domain and not in the angle domain, it needs to be converted into angle domain. A full offset stack is not modeled by the Aki-Richards equation, as it is a mix of offsets, and cannot be used for pre-stack

inversion (Singleton, 2009). The data conditioning has five major steps, namely: Band pass filtering, Muting, Super gather, parabolic radon transforms and Trim statics. These steps are described in the following sections.

The first step of data conditioning is band-pass filtering. The Bandpass filter process allows applying a band-pass filter to a subset of seismic data. Additionally, the data can be shifted in time or in phase. This filter can suppress noise and does not affect the wavelet shape. This filter is very important because the frequency of seismic signals decrease with seismic time, due to the absorption of the higher frequencies (Yilmaz, 2001).

The Muting is the second step of data conditioning. This option applies to an offset-dependent mute to a range of gathers. Muting removes faulty data from a set of gathers by setting the amplitude for this data to zero, so only the reliable data is used for the inversion. Usually mute is applied after Normal moveout correction (NMO) correction to remove the effect of NMO stretch but can also compensate for other errors, such as refractions and geometric noise (Robinson et al., 1986). The amplitude of the upper part is set to zero.

The super gather process is third step of data conditioning. It forms average CDPs to enhance the signal-to-noise ratio, by collecting adjacent CDPs and adding them together (Mari et al., 1999; Singleton, 2009). The reflectors in the super gathers are more clearly visible.

The Parabolic Radon Filter process is the fourth step of the data conditioning. The process is either multiples elimination or radon noise suppression. The model parameters are set to identify the long-period multiples or the random noise within the data. After the model is created, then Radon Transform subtracts the model of these multiples or noise from the data, leaving a data set that is greatly reduced in noise and optimizes the traces (Yilmaz, 1990). The resulted gathers show high signal to noise ratio (S/N ratio). Radon Transform is generally applied to NMO-corrected data, the key events should have a moveout of about 0ms, while any multiples should have effective moveouts. A primary set of parameters in this procedure is the number of parabolas used and their moveout range.

The multiple attenuation minimizes this object function

$$J = \lambda(mod\ m)^p + [mod(Lm - d)]^2 \quad (21)$$

where l = weight factor, m = model in Radon domain, L = Radon transform operator, d = data and p = range from 0 to 2, where 0 is the sparsest and 2 is normal least squares solution.

The solution that minimizes the object function J is

$$m = (\lambda P^{-1} + L^H L)^{-1} L^H D \quad (22)$$

Where P is a diagonal matrix,

$$P_{\bar{a}} = |m_i|^{2-p} + b \quad (23)$$

This is called the "Prior P".

Since J is minimized in the frequency domain, the solution m is, for each frequency:

$$m(\omega) = (\lambda P^{-1} + L^H L)^{-1} L^H D \quad (24)$$

The prior P can be either frequency dependent:

$$P_{\bar{a}} = |m_i(\omega)|^{2-p} + b \quad (25)$$

Or frequency independent, where P is constructed with an average model over a frequency range:

$$P_{\bar{a}} = |\bar{m}_i|^{2-p} + b \quad (26)$$

The trim statics process is the last step of data conditioning. It fixes migration move-out problems on pre-stack data. It attempts to determine an optimal shift to apply to each trace in a gather. The shift is determined by cross correlating each trace with a reference trace to make the input trace better match with the reference trace (Singleton, 2009). Usually the reference trace is the CDP stacked trace. The resulted gathers show very flat horizons. The high (> 60Hz) and low frequencies (< 10Hz) are removed from seismic data. Figure 2 shows the flowchart of the pre-stack inversion.

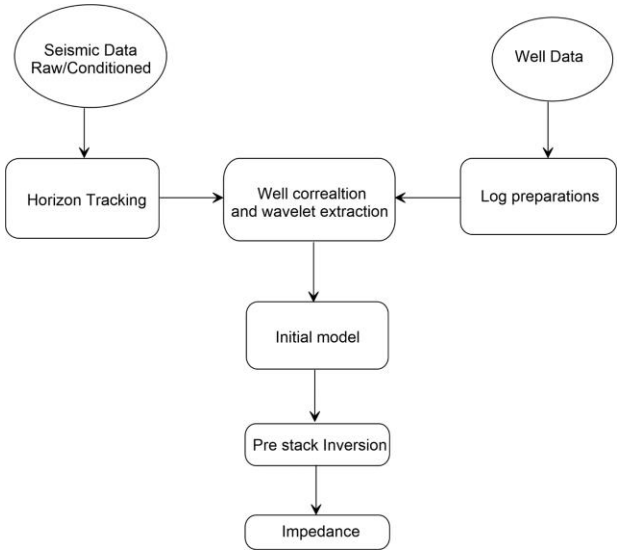

Figure 2. Flow chart of the prestack inversion.

Figure 3 displays the conditioned data gathers step by step. Figure 3a is raw pre stack seismic gather, Figure 3b shows band-pass filtered gather, Figure 3c, 3d, 3e and 3f depict Muted gather, super gather, parabolic radon transforms and Trim static gather respectively. The improved signal to noise ratio zone is highlighted by the arrow and ellipse in the respective figures.

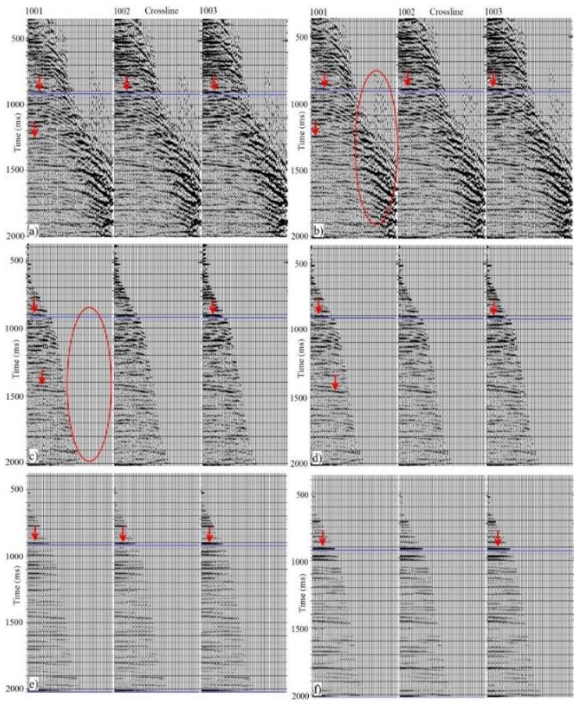

Figure 3. (a) Seismic section, (b) Bandpass section, (c) Mute section, (d) Super gather section, (e) Parabolic radon transform section and (f) Trim Statics section.

SEISMIC TO WELL TIE

Seismic reflection data produces 3D earth image, which is based on large scale P impedance variations and relatively low frequency content in time domain, whereas well logs analysis is executed at higher frequencies, in depth domain. By linking those two information types, it is remains critical to understand the spatial extensions of rock physics properties and therefore to characterize reservoir geometries. The usual method consists in explaining the true time-depth relationship at the well location by producing synthetic seismograms and then correlating them with real seismic traces. Various processes to perform a well-tie have already been suggested (Walden and White, 1984; White and Simm, 2003).

Based on the recorded well logs, a synthetic seismogram aims to reproduce seismic trace data obtained with reflection methods at the well location. A synthetic trace is calculated from the convolutional model below:

$$s(t) = w(t) * r(t) + n(t) \qquad (27)$$

where $s(t)$ is the synthetic trace, $w(t)$ the wavelet which is convolved with the reflectivity log $r(t)$ corresponding to the earth's impulse response obtained from sonic and density logs, and $n(t)$ is the random ambient noise which can be neglected. The seismic-well tie technique is used to correlate well log data to the seismic volume in the vicinity of the well. Then, the synthetic seismogram is compared to the nearest seismic traces of the well trajectory. The standard of the matching is depending on (i) the frequency content, (ii) the correlation of high amplitudes and (iii) transparent zones with low reflectivity (Newrick, 2012). A time-depth relationship either based on the check shots and/or the sonic log calibration is assigned to the well. If some mismatches are observed, various processes are known. Sometimes a simple time shift can be sufficient. Apart from that, a stretch and squeeze can be applied to the synthetic trace. That is yet a controversial method and the geophysicist has to apply it very carefully.

RESULTS AND DISCUSSIONS

The seismic inversions of raw gather and conditioned gather are performed and discussed in this paper. The Figure 3 shows data conditioning steps. The Figure 4 shows comparison of extracted wavelets from raw gather and conditioned gather. In this figure amplitude of trim gather is less in comparison of raw gather due to effect of data conditioning. The abnormal frequency has been removed from the raw gathers. After preparation of data, simultaneous inversion is performed to the seismic data first for composite trace and then for entire seismic gather. Figure 5 shows seismic to well tie analysis for pre-stack simultaneous inversion. Similarly, Figure 6 shows comparison to inverted trace for composite trace and well log curve. It shows comparison of inverted P-impedance (Track 1), S-impedance (Track 2), Density (Track 3) and Vp/Vs ratio (Track 4) with well curves show in green, model curve shown in black, inverted impedance from raw gather shown in red trace, and inverted curve from trim gather shown by blue trace. From the figure, it is noticed that all the inverted curves closely follow the trend of the original curve from well log. It is also noticed that the inverted curves from the trim gather is much closer to the real curve from the well log as compared to the raw gather, which may be attributed to the data conditioning. The correlation coefficient is estimated to be 0.82 and 0.87 for raw gather and trim gather (conditioned gather) respectively.

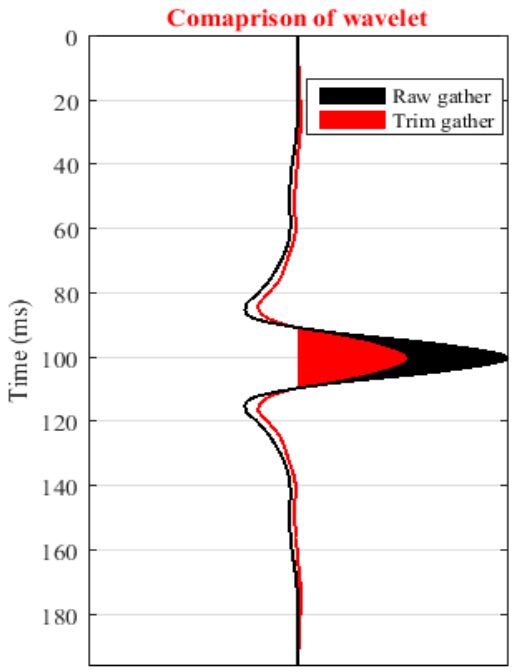

Figure 4. Comparison of wavelets.

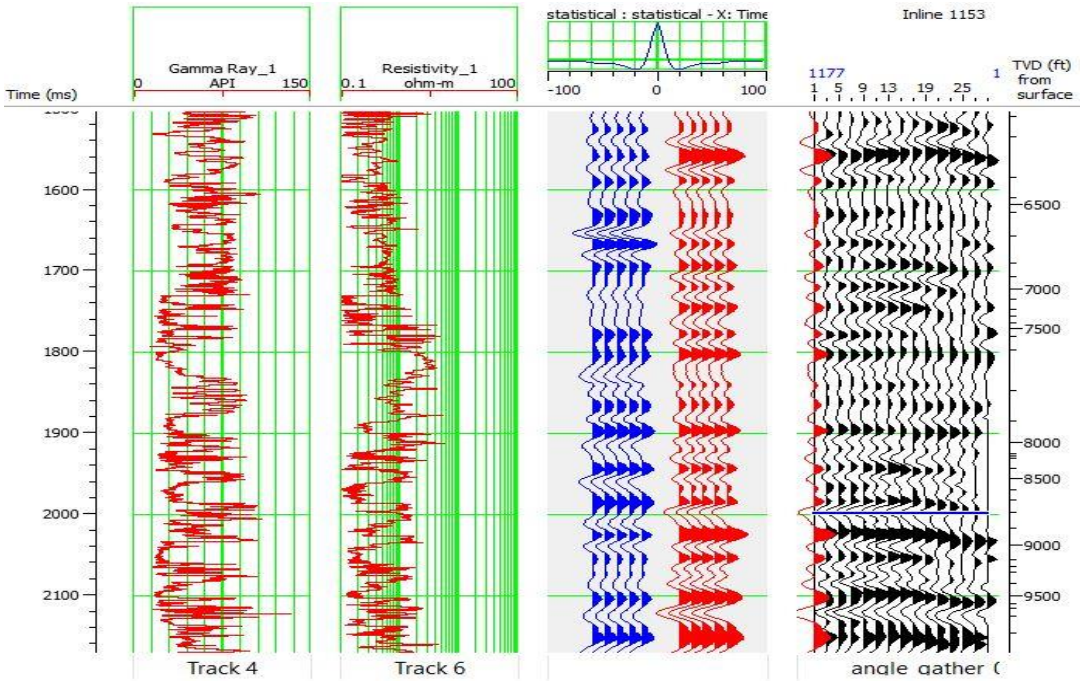

Figure 5. Seismic to well tie.

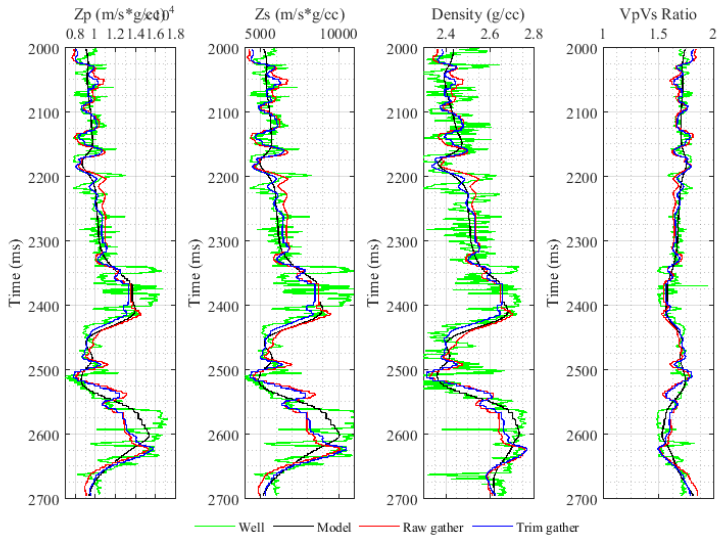

Figure 6. The inverted P-impedance (Track 1), S-impedance (Track 2), Density (Track 3) and Vp/Vs ratio (Track 4) from well (green), model (black), raw gather (red) and trim gather (blue) for composite trace.

Figure 7 shows crossplot between original curves versus inverted curves for quality check of the inverted results. Figure 7a shows crossplot of original and inverted Zp whereas Figure 7b, 7c and 7d depict crossplot of original S-impedance, density and Vp/Vs ratio respectively. It is noticed that the scatter points lie very close to the best-fit line for all cross plot and indicates good performance of the algorithm for both the cases (conditioned and raw gather). The conditioned gather results show slightly more closeness with the best-fit line as compared to the raw gather, which is obvious as the conditioned gather shows slightly better results for the composite trace. Figure 8 shows initial model of parameters for pre-stack inversion.

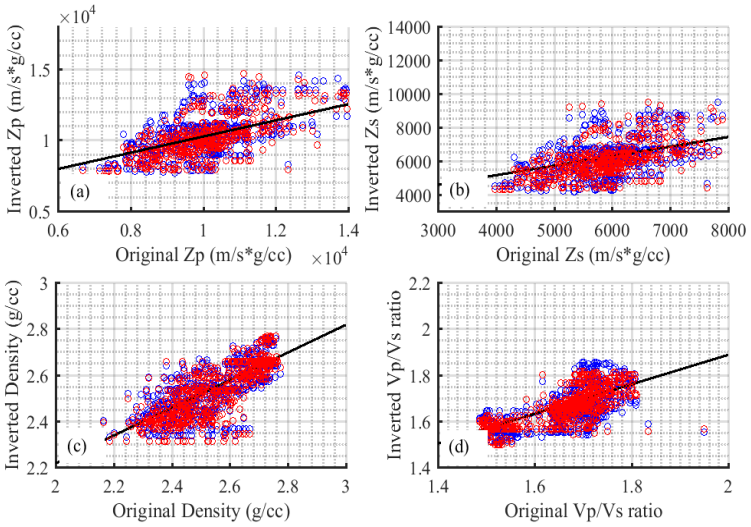

Figure 7. (a) Cross plot between Original Zp and Inverted Zp, (b) Cross plot between Original Zs and Inverted Zs, (c) Cross plot between Original Density and Inverted Density and (d) Cross plot between Original Vp/Vs and Inverted Vp/Vs (For both raw gather and trim gather).

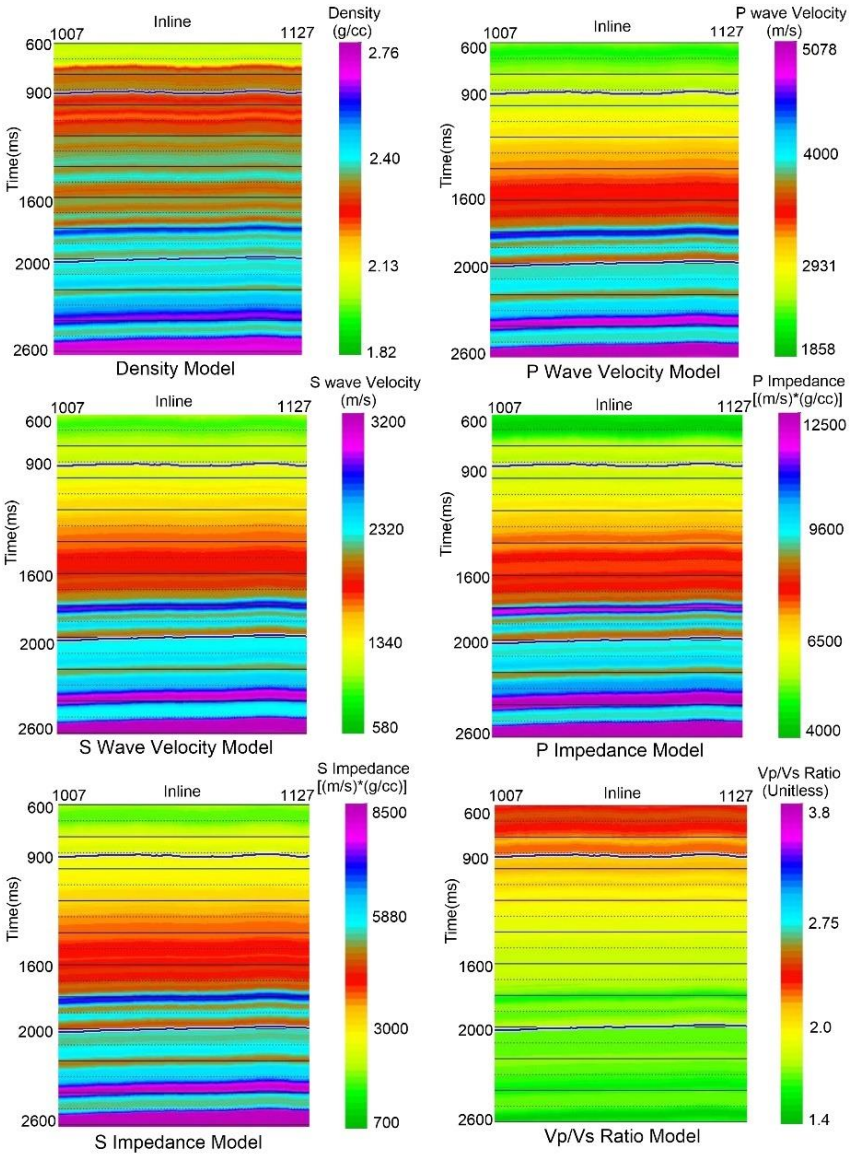

Figure 8. Initial model for pre stack inversion.

After getting satisfactory results from the composite trace for both the cases, the algorithm is applied to the entire seismic sections to estimate subsurface petro-physical parameters in inter well region. Figure 9 shows cross-section of inverted density. Figure 5a shows inverted density section estimated from the conditioned gather, Figure 9b shows inverted density section estimated from the raw gather and Figure 9c shows difference between Figure 9a and Figure 9b. The figure shows that the density varies from 1.8 to 2.8 g/cc for both the cases. The figure further shows continuous variation of density in the subsurface and absence of any anomalous zone in form of any major reservoir. This is preliminary interpretation of the inverted sections. The major changes in the density section from both the cases are highlighted by green to yellow color in Figure 9c. The maximum changes are found near to 700ms time interval due to presence of high amplitude seismic traces, which creates larger differences in both the gathers.

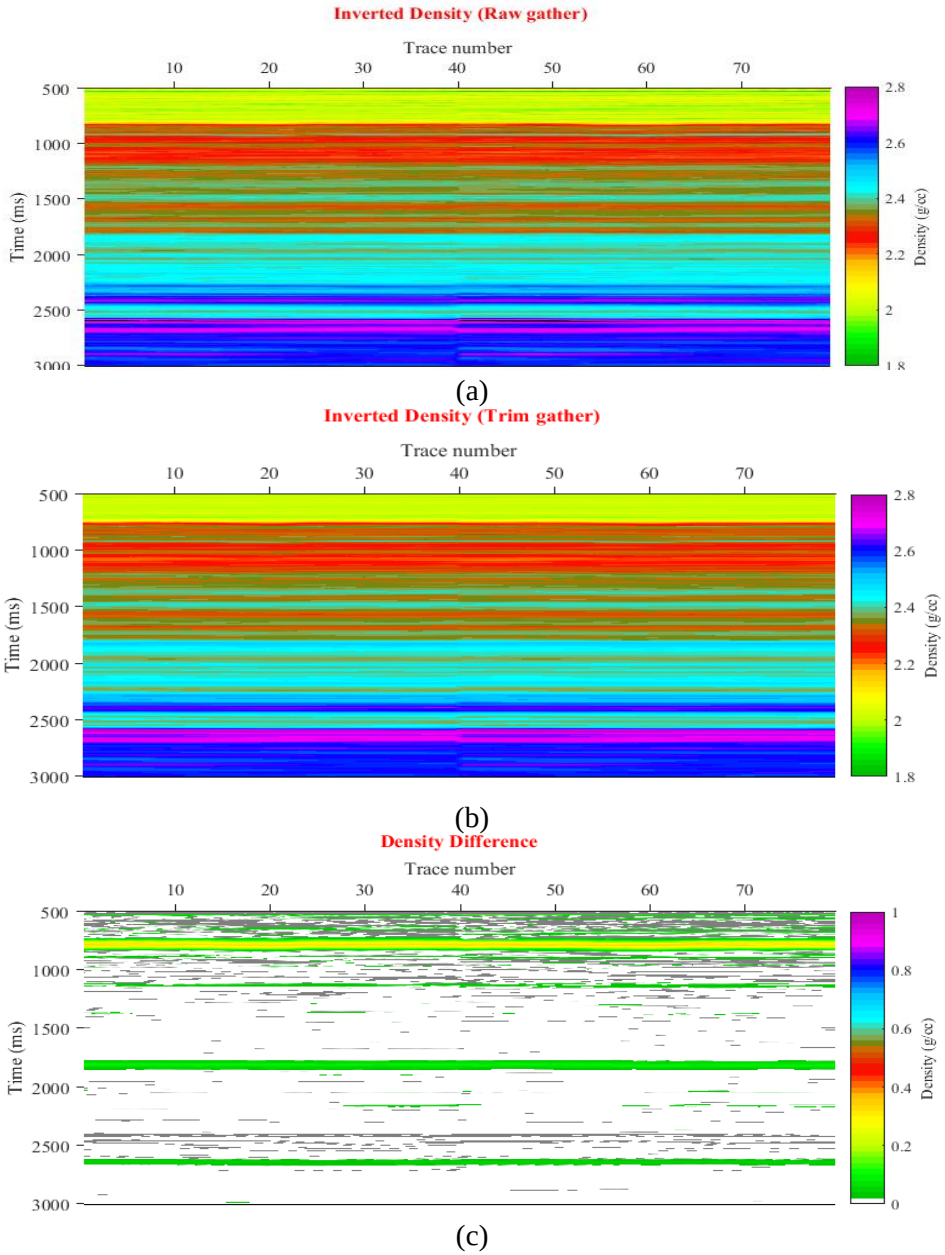

Figure 9. (a) Inverted Density from raw data, (b) Inverted density from conditioned data, (c) Difference between inverted density from raw data and inverted density conditioned data.

Figure 10 depicts cross-section of inverted P-wave velocity. Figure 10a depicts inverted P-wave velocity section estimated from the conditioned gather, Figure 10b depicts inverted P-wave velocity section estimated from the raw gather and Figure 10c shows difference between Figure 10a and Figure 10b. The interpretation of inverted velocity section shows continuous variation and there is no presence of any anomalous zone. The major changes in both the section are highlighted in Figure 10c.

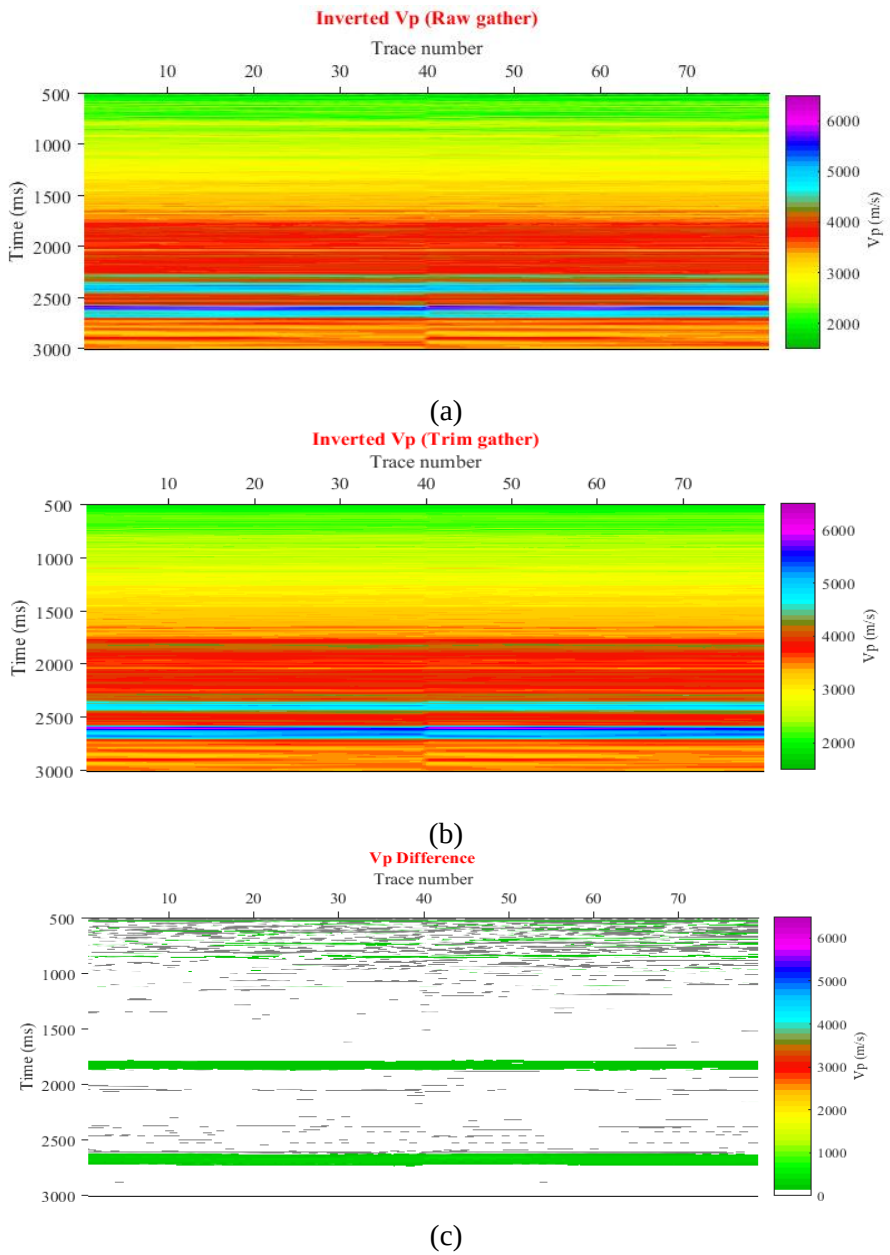

Figure 10. (a) Inverted P-wave velocity from raw data, (b) Inverted P-wave velocity from conditioned data and (c) Difference between inverted P-wave velocity from raw data and inverted P-wave velocity from conditioned data.

Similarly, Figure 11 shows cross-section of inverted S-wave velocity, Figure 12 depicts cross-section of P-impedance, Figure 13 depicts cross-section of S-impedance, Figure 14 depicts cross-section of Vp/Vs ratio, Figure 15 shows cross-section of lambda-rho and Figure 16 shows cross-section of mu-rho. In these figures, the first plot(top) shows petro-physical parameters estimated from the conditioned gather (trim statics) and the middle plot shows section estimated from the raw gather and the bottom plot describe the changes found between these two cases. In all the figures, the major changes are highlighted.

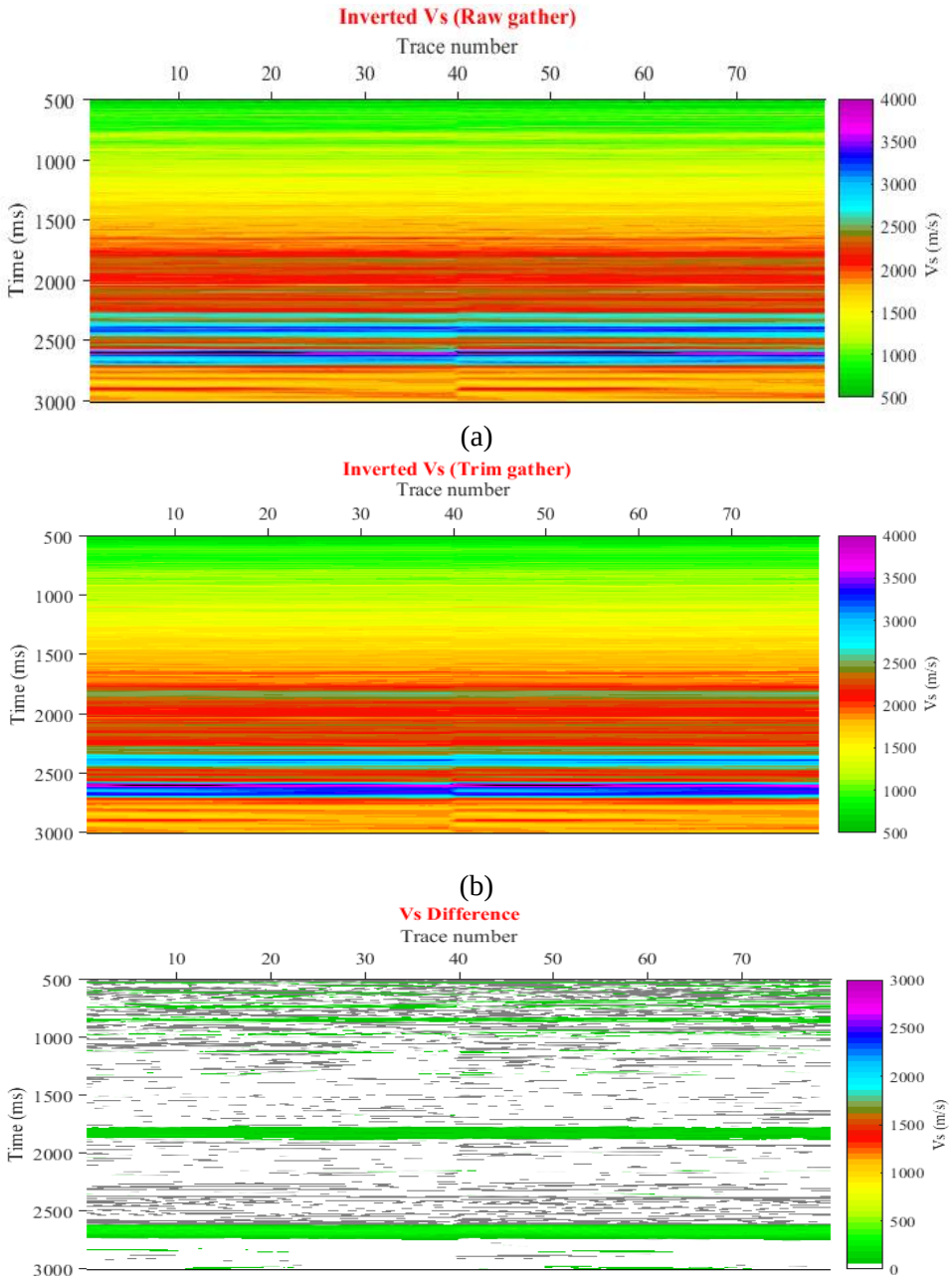

Figure 11. (a) Inverted S-wave velocity from raw data, (b) Inverted S-wave velocity from conditioned data and (c) Difference between inverted S-wave velocity from raw data and inverted S-wave velocity from conditioned data.

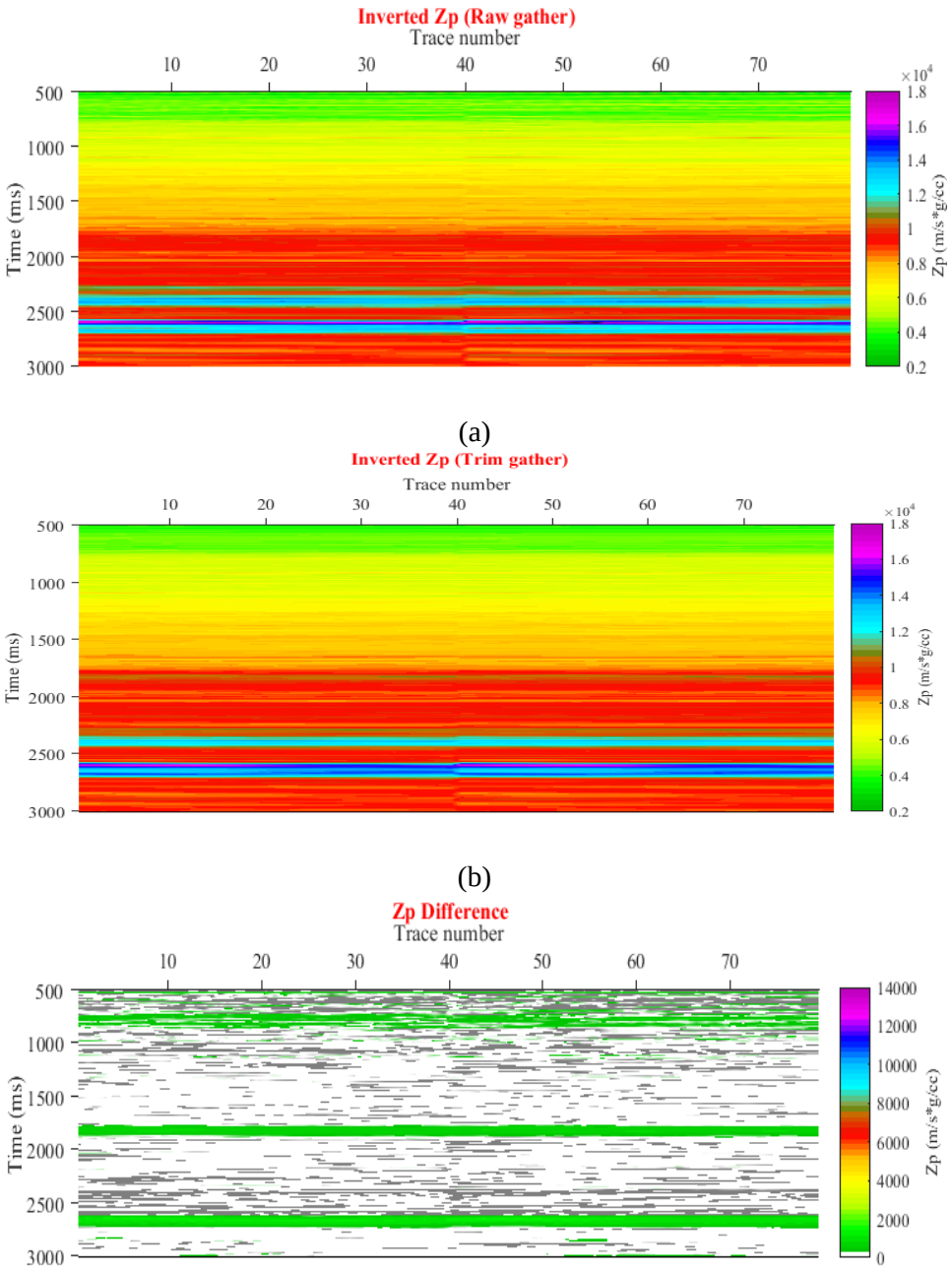

Figure 12. (a) Inverted P-impedance from raw data, (b) Inverted P-impedance from conditioned data and (c) Difference between inverted P-impedance from raw data and inverted P-impedance from conditioned data.

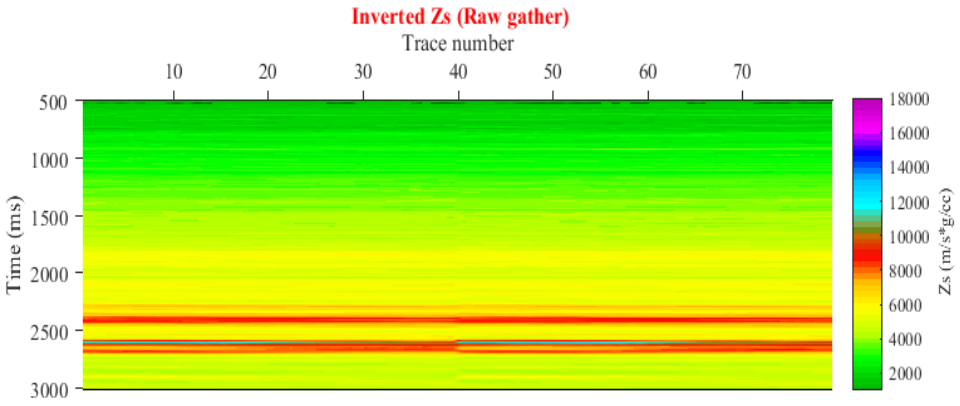

(a)

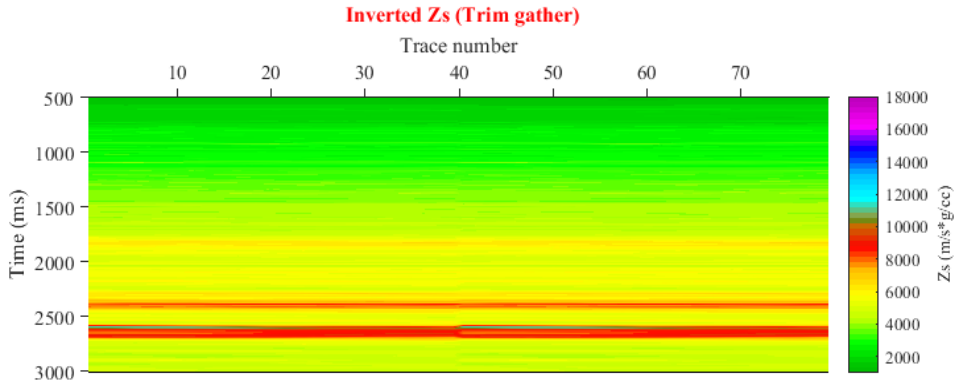

(b)

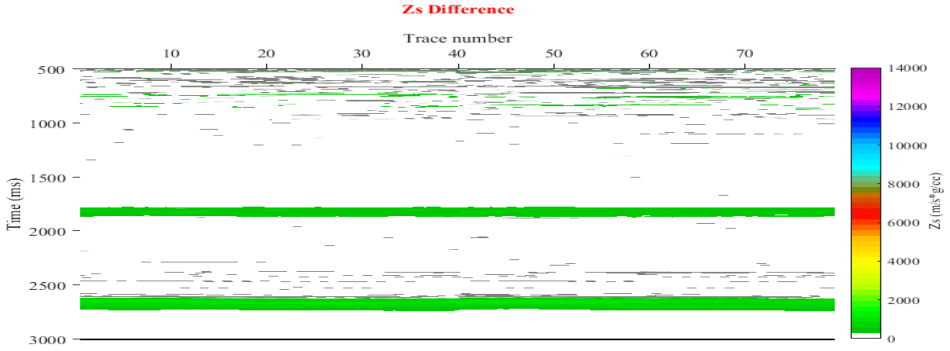

(c)

Figure 13. (a) Inverted S-impedance from raw data, (b) Inverted S-impedance from conditioned data and (c) Difference between inverted S-impedance from raw data and inverted S-impedance from conditioned data.

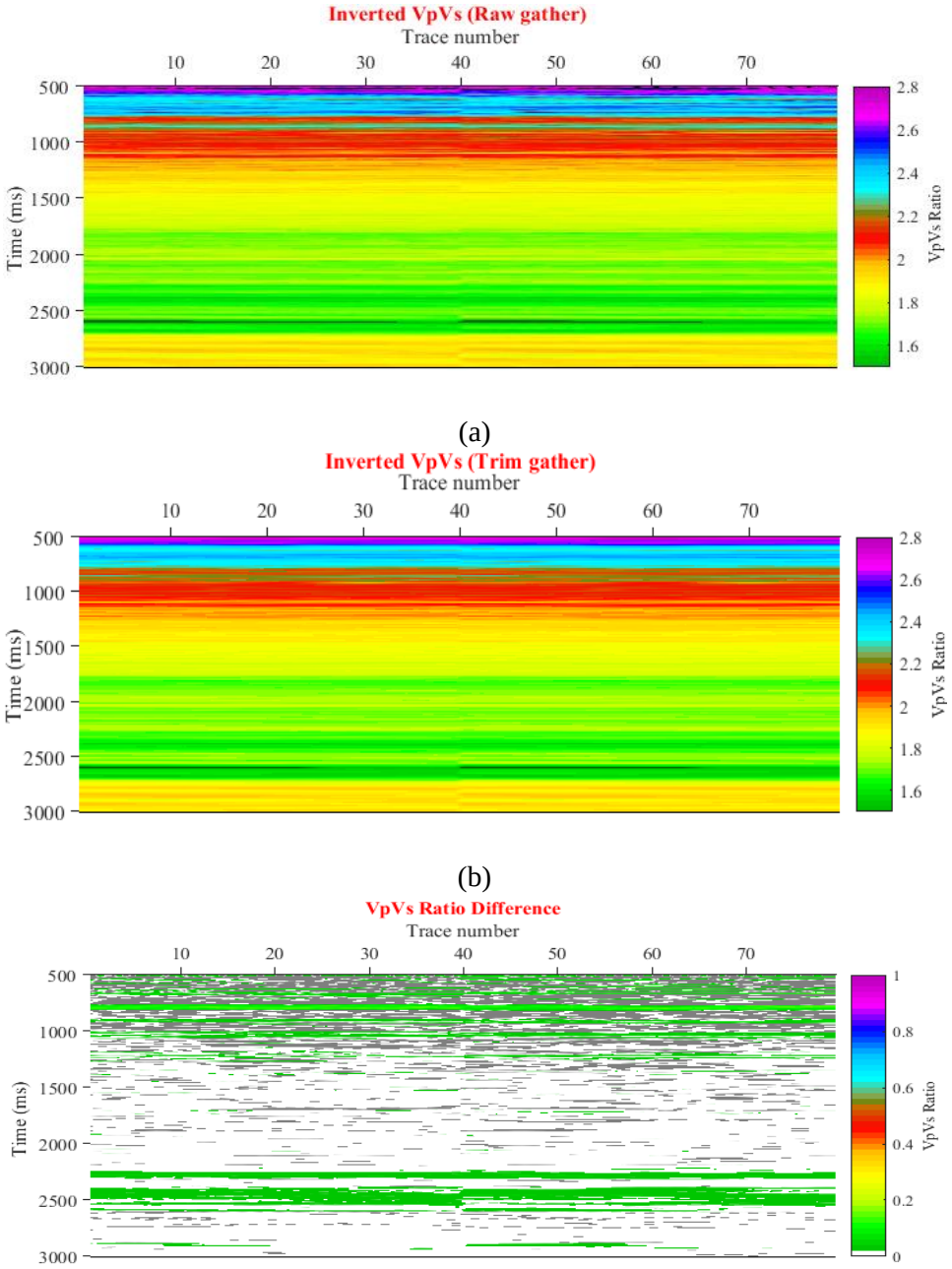

Figure 14. (a) Inverted Vp/Vs ratio from raw data, (b) Inverted Vp/Vs ratio from conditioned data and (c) Difference between inverted Vp/Vs ratio from raw data and inverted Vp/Vs ratio from conditioned data.

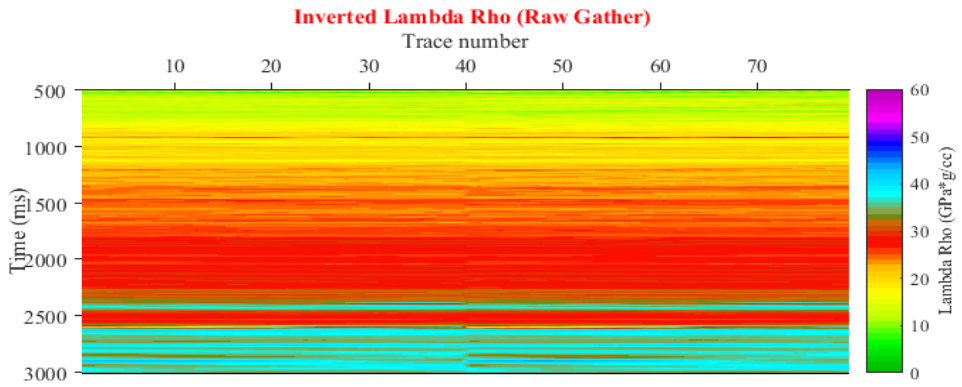

(a)

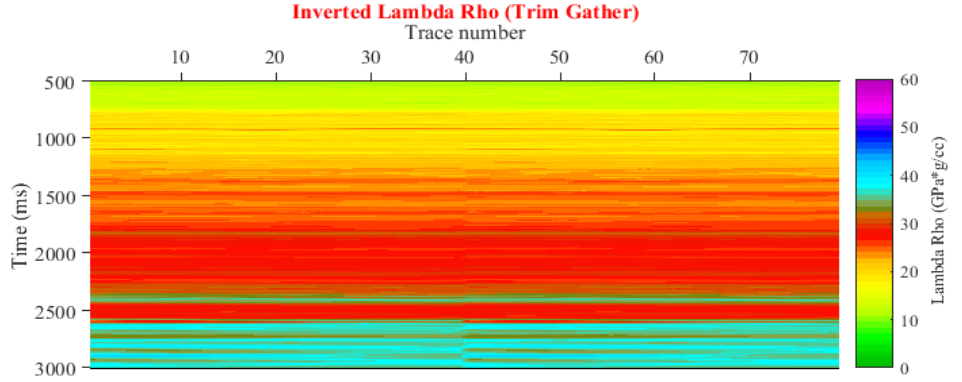

(b)

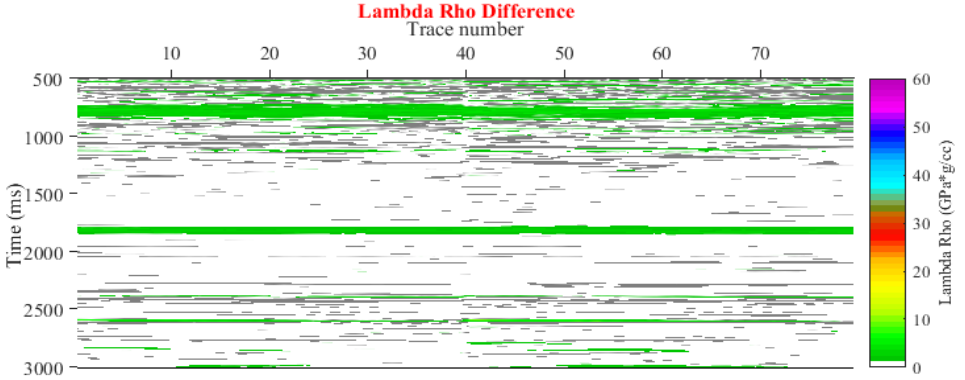

(c)

Figure 15. (a) Inverted lambda rho from raw data, (b) Inverted lambda rho from conditioned data and (c) Difference between inverted lambda rho from raw data and inverted lambda rho from conditioned data.

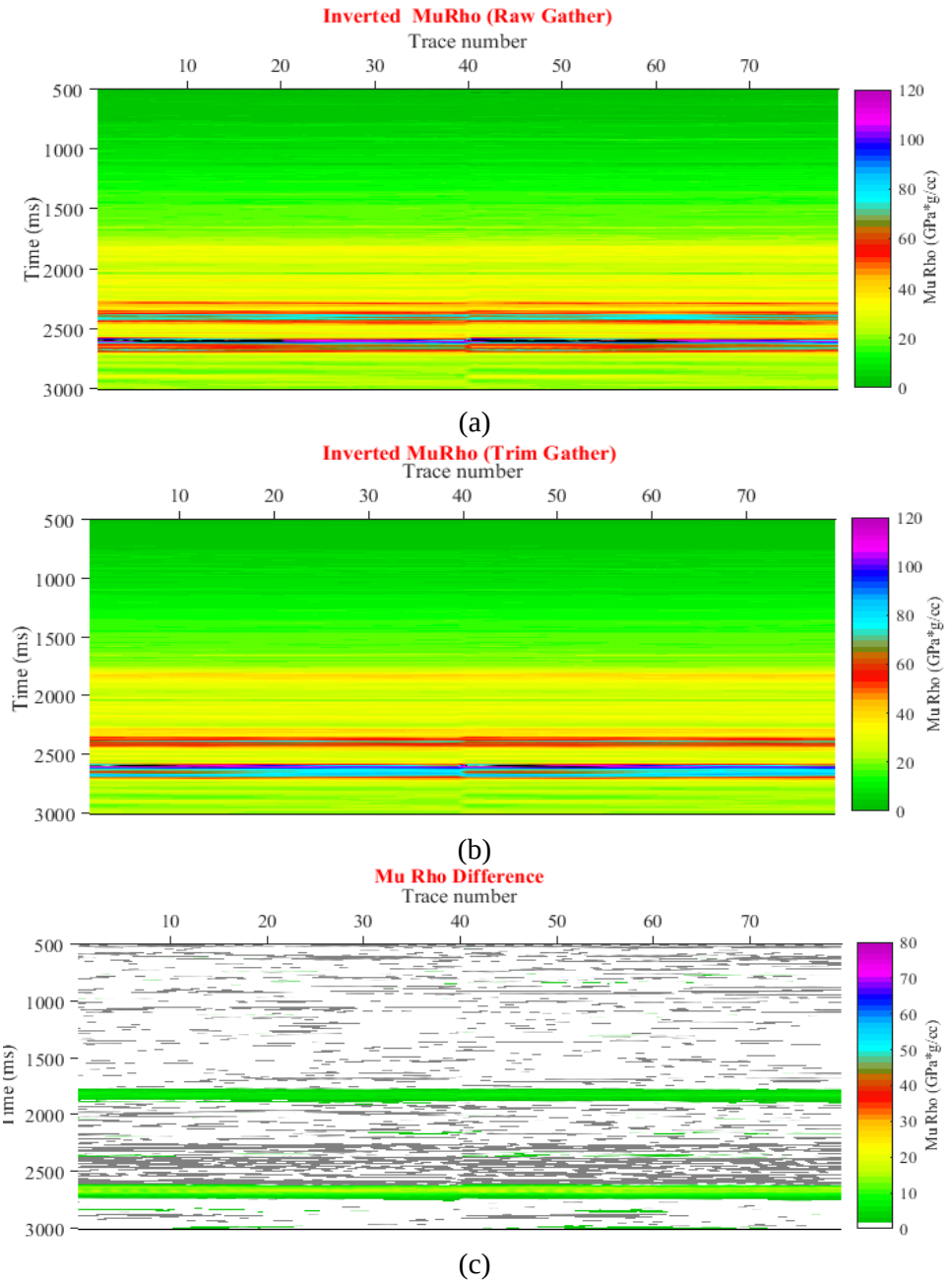

Figure 16. (a) Inverted mu rho from raw data, (b) Inverted mu rho from conditioned data and (c) Difference between inverted mu rho from raw data and inverted mu rho from conditioned data.

The interpretation of all the above discussed petro-physical parameters reveals smooth variation of petrophysical parameters and hence point towards the non-existence of any prospective zone. However, these results are presented for only small datasets of the region. The interpretations of the inverted results also indicate slightly high resolution of the conditioned gather as compared to the raw gather. This high resolution can be seen in the inverted section where thinner layer can be identified from the inverted section of the conditioned gather as compared to the raw gather.

Thereafter, crossplot among inverted sections were generated to estimate relationship between the petro-physical parameters. Figure 17 shows cross plot among the inverted petrophysical parameters and gives relationship among them, which is very useful to estimate petrophysical parameters directly in this region. Both sections (raw and conditioned gather) show slightly different relationship, but an average equation of both cases is given below.

$$V_S = 0.8V_P - 850 \quad (28)$$

$$Z_S = 0.74Z_P - 15500 \quad (29)$$

$$Z_P = -8200\frac{V_P}{V_S} + 24000 \quad (30)$$

Figure 18 shows horizontal slices comparison for raw and conditioned data.

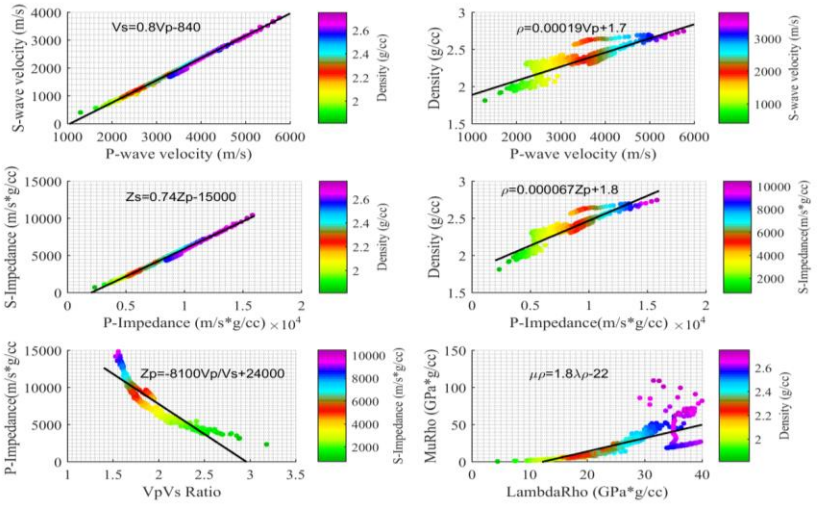

(a)

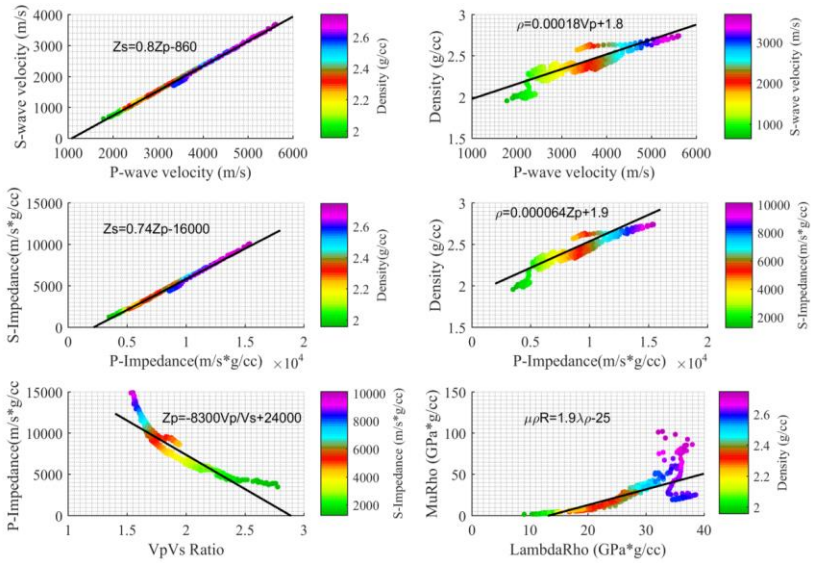

(b)

Figure 17. (a) Crossplots from raw gather and (b) Crossplots from conditioned gather.

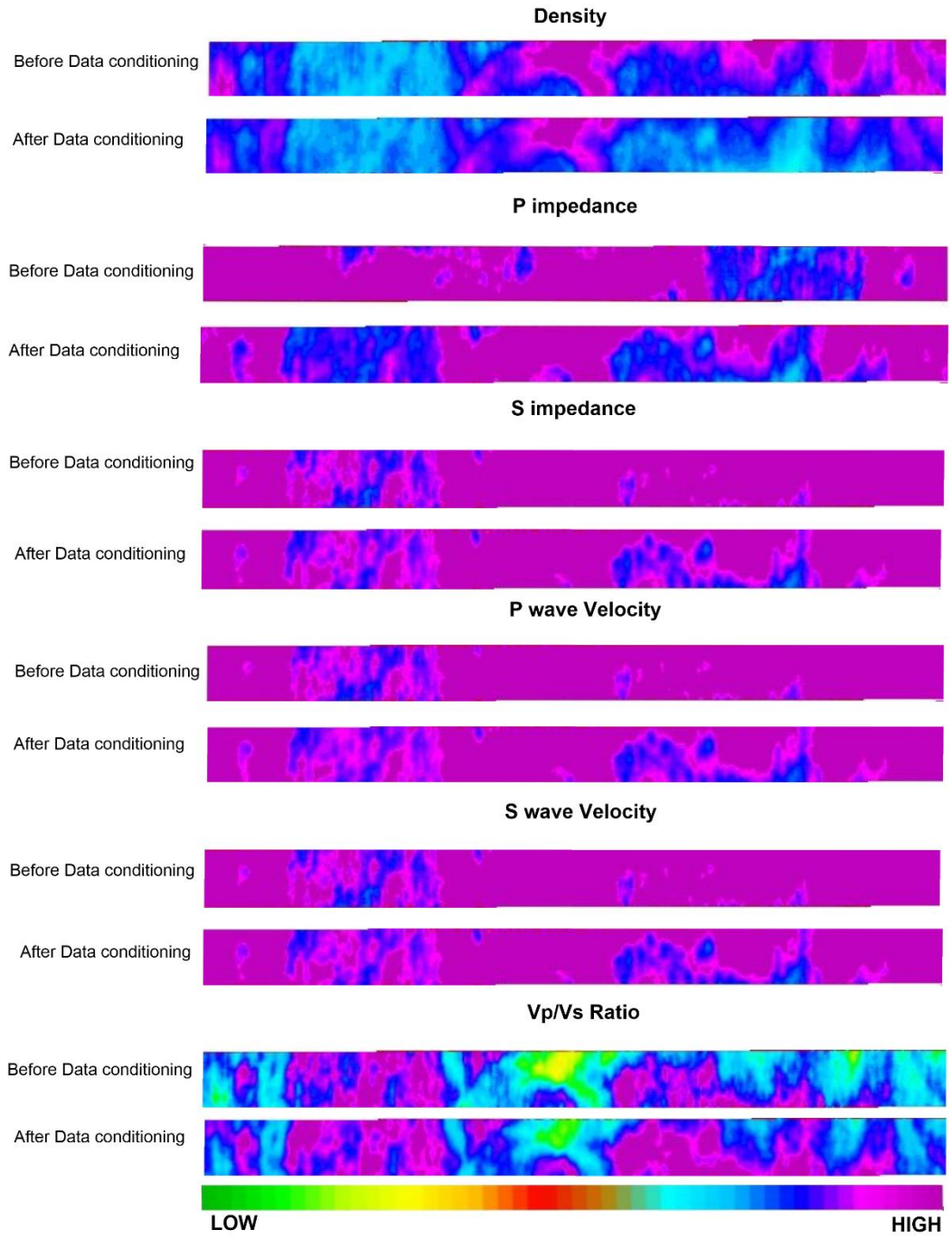

Figure 18. Horizontal slices comparison.

CONCLUSIONS

In present study, a variety of petro-physical parameters i.e. impedance, density, velocity, Vp/Vs ratio, lame parameters are estimated from inversion of conditioned and raw gathers and their comparison is also illustrated. In the first step, one composite trace is extracted from both the gather and simultaneous inversion is applied to estimate petro-physical parameters. The comparison of inverted petro-physical parameters with original parameters from the well logs, pointed the good performance of the algorithm for both the cases. The findings show slightly better results for the

conditioned gather as compared to the inversion results for the raw gather. The correlation coefficients also justify it as it is 0.82 for raw gather and 0.87 for the conditioned gather. Thereafter, entire seismic section is inverted and a variety of petro-physical parameters are estimated and compared in inter well region from both the gather. The interpretation of inverted results for both the cases, indicates non-existence of any prospective zone and all the inverted sections show smooth variation of petro-physical parameters. The results also show slightly higher resolution of inverted results for the conditioned gather as compared to the raw gather in which comparatively thinner reflector can be easily identified. The horizontal slices show good effect of data conditioning.

ACKNOWLEDGEMENTS

We thank CGG Veritas for providing the HRS software, Matlab and Opendtect seismic repository for providing data. We are also grateful to some of our colleagues for the support and fruitful discussions.

Compliance with Ethical Standards

The authors declare that they have no conflict of interest and adhere to copyright norms.

REFERENCES

Aki, K. and Richards, P., 1980. Quantitative seismology: Theory and methods. WH Freeman and Co., 1.

Buland, A., Landry, M., Andersen, M. and Dahl, T., 1996. Avo inversion of troll field data; Geophysics, 61(6), 1589-1602.

Buland, A. and Omre, H., 2003. Bayesian linearized avo inversion. Geophysics, 68(1), 185-198.

Castagna, J.P., Batzle, M. L. and Eastwood, R.L., 1985. Relationships between compressional-wave and shear-wave velocities in clastic silicate rocks. Geophysics, 50(4), 571-581.

Chopra, S. and Sharma, R.K., 2016. Preconditioning of seismic data prior to impedance inversion. Geophysical Corner, AAPG Explorer, January 2016 issue, 41(3).

Fatti, J.L., Smith, G.C., Vail, P.J., Strauss, P.J. and Levitt, P.R., 1994. Detection of gas in sandstone reservoirs using avo analysis: A 3-D seismic case history using the geostack technique; Geophysics, 59(9), 1362-1376.

Gardner, G., Gardner, L. and Gregory, 1974. A formation velocity and density-the diagnostic basics for stratigraphic traps, Geophys., 39(6),770-780.

Goodway, B., Chen, T. and Downton, J., 1997. Improved avo fluid detection and lithology discrimination using lame petro-physical parameters; "λρ", "μρ", & "λ/μ fluid stack", from P and S inversions. 67th annual international meeting, expanded abstracts, Soc. Expl., 183-186

Hampson, D.P., Russell, B.H. and Bankhead, B., 2005. Simultaneous inversion of pre-stack seismic data. In 2005 SEG Annual Meeting. Society of Exploration Geophysicists.

Larsen, J.A., 1999. Avo inversion by simultaneous PP and PS inversion. M.Sc. Thesis, University of Calgary.

Mandal, A. and Srivastava, E., 2018. Enhanced structural interpretation from 3D seismic data using hybrid attributes: New insights into fault visualization and displacement in Cretaceous formations of the Scotian Basin, offshore Nova Scotia. Marine and Petroleum Geology, 89, 464-478.

Mari, J.L., Glangeaud, F., Coppens, F. and Painter, D., 1999. Signal processing for geologists & geophysicists. Technip.

Matlab and Statistics Toolbox Release 2015. The Math Works Inc., Natick, Massachusetts, United States.

Maurya, S. and Singh, K.H., 2015. LP and ML sparse spike inversion for reservoir characterization- a case study from Blackfoot area Alberta Canada. 77th EAGE Conference and Exhibition, Madrid, Spain.

Maurya, S. P. and Sarkar, P., 2016. Comparison of post stack seismic inversion methods: a case study from Blackfoot Field. Canada. Int. J. Scientific & Engineering Res., 7(8), 1091-1101.

Maurya, S. P. and Singh, K.H., 2017. Band Limited Impedance Inversion of Blackfoot Field, Alberta, Canada; J. Geophys, 38(1), 57-61.

Maurya, S.P., Singh, K.H., Kumar, A. and Singh, N.P., 2018. Reservoir characterization using post stack seismic inversion techniques based on real coded genetic algorithm; J. Geophysics, 39(2), 95-103.

Maurya, S.P., Singh, K.H. and Singh, N.P., 2019. Qualitative and quantitative comparison of geostatistical techniques of porosity prediction from the seismic and logging data: A case study from the Blackfoot Field Alberta Canada. Mar. Geophys. Res., 40(1), 51-71.

Newrick, R., 2012. Well tie basics. Well tie perfection, 52, 104-107.

Niu, L., Geng, J. and Wu, X., 2018. Linearized AVO Inversion with Modified Aki-Richards' Approximation. In *80th EAGE Conference and Exhibition 2018*.

Richards, P.G. and Frasier, C.W., 1976. Scattering of elastic waves from depth-dependent in homogeneities, Geophys., 41(3), 441-458.

Robinson, E.A., Durrani, T.S. and Peardon, L.G., 1986. Geophysical signal processing. Prentice-Hall, Inc.

Shuey, R., 1985. A simplification of the zoeppritz equations. Geophysics, 50(4), 609-614.

Simmons, J.L. and Backus, M.M., 1996. Waveform-based avo inversion and avo prediction error. Geophysics, 61(6), 1575-1588.

Simmons, J. and Backus, M., 2003. An introduction multicomponent. The Leading Edge., 22(12) ,1227- 1262.

Singleton, S., 2009. The effects of seismic data conditioning on pre-stack simultaneous impedance inversion. The Leading Edge, 28(7), 772-781.

Walden, A.T. and White, R.E., 1984. On errors of fit and accuracy in matching synthetic seismograms and seismic traces. Geophys. Prosp., 32(5), 871-891.

White, R.E. and Simm, R., 2003. Tutorial: Good practice in well ties. First Break., 21(10).

Yilmaz, Ö., 2001. Seismic data analysis; Society of exploration geophysicists Tulsa, OK.,1. https://library.seg.org/doi/abs/10.1190/1.9781560801580

Yilmaz, Ö., 1990. Seismic data processing; Society of Exploration Geophysicists.

Received on: 25.1.19; Revised on: 6.4.19; Accepted on: 9.5.19

Efficacy of the gravity and magnetic methods in mapping the subsurface features in the NE part of Madhya Pradesh (India)

R. Kumar* and A.K. Singh
Geological Survey of India, Central Region, Nagpur-440006, Maharashtra, India
*Corresponding author: rajan.08.ism@gmail.com

ABSTRACT

This study brings out the efficacy of the gravity and magnetic methods in delineating the subsurface features, such as fault/ tectonic contact and basin boundaries in parts of Singrauli and Sidhi districts of Madhya Pradesh (India). The Bouguer gravity and magnetic anomaly map, which was subjected to several filtering and processing techniques, clearly reflected the inferred structural features, which in turn correlate well with the geological features trending in E-W and NE-SW direction. Magnetic anomaly of higher amplitudes in the northwestern part, coincides with the presence of metabasalt, biotite schist and BIF, whereas in the northeastern part, it is due to the concentration of the magnetite grains in biotite schist and phyllite. The regional gravity low observed in central, northeastern and southwestern parts of the area is ascribed to sedimentary rocks belonging Gondwana formation. The residual gravity map shows several local gravity anomalies with amplitude and direction. Similarly, the residual magnetic anomalies reveal various shapes with the direction of extensions and orientations. The inferred boundary/ contact zone (F1-F1' and F3-F3') and faults like Amsi-Jiawan (F5-F5') and Jamui-Markundi (F6-F6'), are clearly brought out in the Total Horizontal Derivative (THDR) and Tilt derivative (TDR) maps of gravity data. The THDR of the magnetic data shows magnetic maxima over the Mahakoshal formation and also at various scattered locations in the northeastern and central parts of the map. The TDR of the magnetic data depicts anomalies close to zero magnetic values that coincide with edges or boundaries of the inferred faults like Amsi-Jiawan (F5-F5') and Jamui-Markundi (F6-F6'). The majority of Euler solutions fall at the contact between two litho-units faults/ contacts, with varying depth of 0.5 to 2.5km.

Keywords: Amsi-Jiawan fault, Jamui-Markundi fault, Singrauli, Gravity and magnetic studies, Total Horizontal Derivative (THDR), Tilt derivative (TDR).

INTRODUCTION

The integrated geophysical methods play a key role in the delineation of the subsurface features (inferred fault/ tectonic contact, cavity detection, regional and global tectonics and basin boundaries), which in turn, provide clues for the exploration of bulk mineral deposits. The study area located in parts of Singrauli and Sidhi districts of Madhya Pradesh, is bounded by the latitude 24º 00´N to 24º 30´N and longitude 81º 45´E to 82º 45´E (Figure 1). The objective of the study is to map the subsurface structures, (inferred fault/ tectonic contact and basin boundaries) from integrated gravity and magnetic studies. Two main faults, Amsi-Jiawan and Jamui-Markundi, has also been delineated from the study area.

GEOLOGY

Geologically, the area is represented by Vindhyan Supergroup, Sidhi gneiss group, Chotanagapur gneissic complex group, Mahakoshal Group, Gondwana Supergroup and Deccan Traps (Figure 2). The Vindhyan Supergroup is represented by Semri and Kaimur group of rocks. The Semri Group lies unconformably over the older granite gneiss and Mahakoshal Group of rocks. The Mahakoshal Group of rock are affected by the tectonic disturbances forming the weaker planes, which are later occupied by quartz veins. The granites belonging to Barambaba granite formation of Palaeoproterozoic age, occur as isolated outcrops and found dominantly exposed in northwestern part of the study area. Similarly, the

Chhotanagpur gneissic complex is represented by quartzite, biotite schist and granite gneiss. The Lower Gondwana Supergroup in the studied area is represented by Talchir, Barakar, Barren Measure and Pali formations, which consists mainly of ferruginous sandstone and sandstone. Besides, the rocks of Chhotanagpur gneissic complex and Lower Gondwana Group of rocks are intruded by basic and ultra-basic intrusive, syenite, quartz veins and pegmatite. The contact between the rocks of Gondwana and Deccan traps, is represented by basaltic rock (Pandhare, 1972; Subramanyam et al., 1972; Subramanyam et al.,1975; Jha et al., 1980; Majumdar, 1980; Jha and Devarajan, 2002a,b; Kumar and Punekar, 2018).

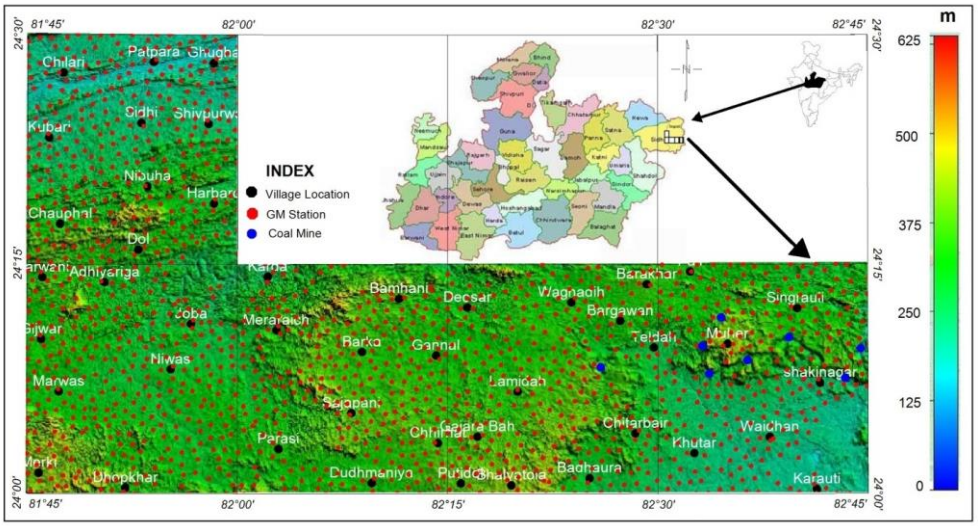

Figure 1. Gravity and magnetic stations overlaid on Digital Elevation Model.

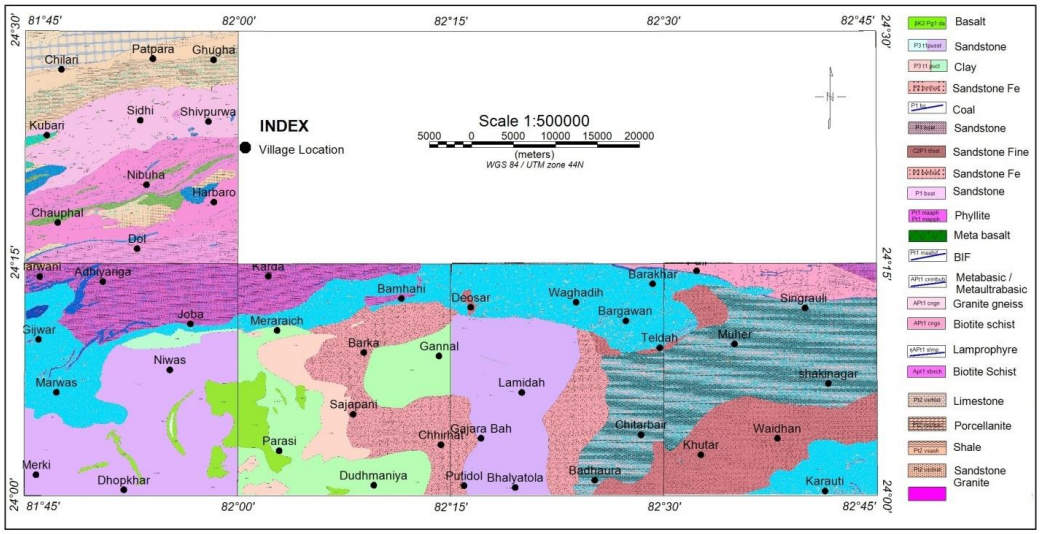

Figure 2. Geology of the area (Source: Geological Survey of India (GSI), India**).**

METHODOLOGY

Gravity and magnetic survey

Gravity, magnetic and Differential Global Positioning System (DGPS) data were collected by employing the CG-5 Autograv gravimeter, GSM-19T magnetometer and DGPS 1200, respectively. The gravity and magnetic (GM) surveys were carried out with a station interval of 1 observation per 2.5 sq km in an area of about 3500 sq km. The elevation from mean sea level (MSL) of each gravity stations was obtained by tying the GPS base to triangulation point of Survey of India using DGPS. The gravity data was reduced following the standard corrections of gravity data and the

Bouguer gravity anomaly over the study area was computed for a mean crustal density of 2.67 gm/cc. International gravity formula 1980 was used to account for the latitude correction. The magnetic observations (total field) were corrected for the diurnal variation and International Geomagnetic Reference Field (IGRF) correction, using IGRF coefficients for 2015 epoch to evaluate the magnetic anomaly at each station. Leica Geo Office, Surfer 9 (Golden software) and Geo-Soft Oasis Montaj software version 9.1 were used for processing and preparing the geophysical maps (Bharati et al., 2016; Gorle et al., 2016; Kumar and Punekar, 2018).

RESULTS AND DISCUSSION

Bouguer Gravity Anomaly map

The Bouguer gravity anomaly map shows a variation of 68 mGal from -84 mGal to -16mGal (Figure 3). The general trend of the Bouguer gravity contours varies from E-W to NE-SW directions. The gravity gradient (F1-F1') trending in NW-SE direction passing from Pali to Singrauli in northeastern part of the area is inferred as boundary/ contact zone between Mahakoshal Group and Lower Gondwana group, as shown in the geological map (Figure 2). The gravity gradient (F3-F3') trending in SW-NE direction from Marwas to Joba villages, continues up to Bargawan in approximately E-W direction. It is inferred as the boundary between the Chhotanagpur gneissic complex group (granite gneiss) and Lower Gondwana group, correlating with the feature shown in geological map (Figure 2). The gravity gradient (F4-F4') observed near Karda in NE-SW direction, clearly reflects the contact between Mahakoshal Group (Phyllite) and Chhotanagpur gneissic complex group (granite gneiss), well correlating with the features in the geological map (Figure 2). The high gravity anomaly 'H1 and H2', with swelling and pinching recorded near Karada and Chauphal, Nibuha, Harbaro and Dol, respectively over the Mahakoshal Group (Phyllite), is due to the density variation caused by the frequent grading of metamorphism in Mahakoshal formation. Similarly, the NW-SE gravity gradient (F2-F2'), passing from Waghadih to Khutar, may be inferred as fault/ contact in between two low gravity anomaly zones (L1 and L2) over the coal mine areas (Figure 1). In contrast, the NE-SW gravity gradient (F5-F5') from Chauphal to Shivpurwa, is inferred as fault/ contact between Sidhi gneiss group (granite gneiss) and Mahakoshal Group, which is known as Amsi-Jiawan fault. The NE-SW trending gravity gradient (F6-F6') observed in northwestern part passing from Kubari to Ghugha, is also inferred as a fault/ contact, between Semri Group (sandstone) and Sidhi gneissic group (granite gneiss), which is known as Jamui-Markundi fault.

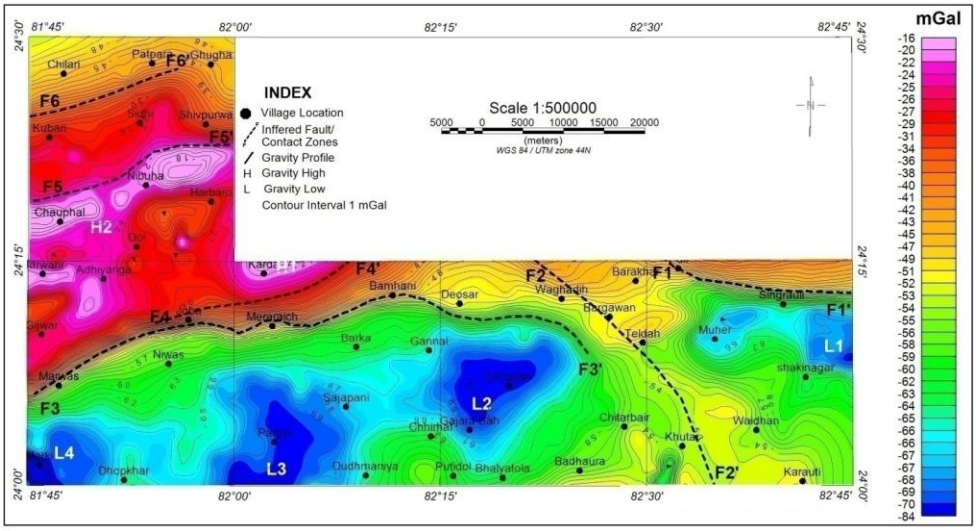

Figure 3. Bouguer gravity anomaly contour map (Kumar and Punekar 2018).

Magnetic Anomaly (T.F.) map

The Magnetic anomaly values vary from a minimum of -1685nT to a maximum of 2484nT, with an overall variation of 4169nT (Figure 4). Few bipolar anomalies with different amplitudes are recorded in the northeastern part of the area over granite gneiss. Based on the high and low intensity magnetic anomaly contour pattern, the study area is divided into three major domains, viz., domain 'I', 'II' and 'III'. The domain 'I' is represented by high intensity anomaly varying between 395 to 2484 nT in the southwestern part around Chaupha, Harbaro, Nibuha, Karda and Dol over Sidhi gneiss group (Granite gneiss), Mahakoshal (Phyllite) and Chhotanagpur gneissic (Granite gneiss). The domain 'II' is characterized by moderate anomalies in the range of 225 to 395 nT in the central part, characterized by sedimentary rocks belonging to Gondwana formation. The low intensity magnetic anomalies in the range of -1685 to 225 nT marked as domain 'III', are observed near the northwestern part around Kubari, Chilari, Patpara, Sidhi, Shivpurwa and Ghugha, that contain sandstone, limestone, shale and porcellanite rocks of Vindhyan Supergroup and also over the quartzite and dolomite rocks of Mahakoshal Group.

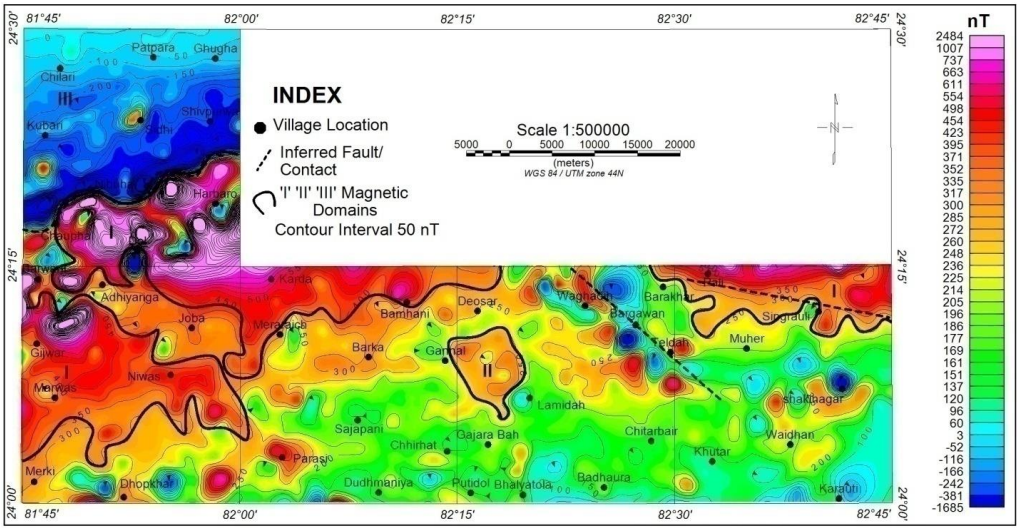

Figure 4. Magnetic anomaly contour map.

Regional gravity and residual gravity anomaly map

The regional gravity and magnetic anomaly maps are prepared using low pass filter, while the residual gravity and magnetic anomalies are prepared using regional-residual separation technique. Regional gravity anomaly map (Figure 5) reveals a regional gravity low in the northeastern, central and southwestern parts of area due to presence of sedimentary rock (Gondwana formation), as also observed in the Bouguer gravity anomaly map. The regional gravity high in northwestern part of the area indicates the deeper causative sources of these anomalies.

The residual gravity anomaly map with various amplitude and direction (Figure 6) is obtained by removing regional from the Bouguer gravity anomaly, using regional-residual separation technique. The NW-SE local gravity anomaly from Pali to Singrauli in the northeastern part of the area, may be related to the inferred shallow fault/ contact zone (F1-F1' in Figure 3) in between Mahakoshal Group and Lower Gondwana group of rocks, whereas, the gravity field (SW-NE and E-W) from Marwas to Bargawan, is inferred as the boundary (F3-F3' in Figure 3) between the Chhotanagpur gneissic complex group (granite gneiss) and Lower Gondwana group. The NE-SW local gravity anomaly near Chauphal to Shivpurwa in northwestern part of the area, may be related to the shallow fault (F5-F5' in Figure 3) in between Sidhi gneiss group (granite gneiss) and Mahakoshal Group, known as Amsi-Jiawan fault, whereas, the local gravity

(NE-SW) from Kubari to Ghugha is inferred as the boundary (F6-F6' in Figure 3) between Semri Group (sandstone) and Sidhi gneiss group (granite gneiss), which has also been reported earlier (Auden,1933; Chaubey, 1970), and is known as Jamui-Markundi fault.

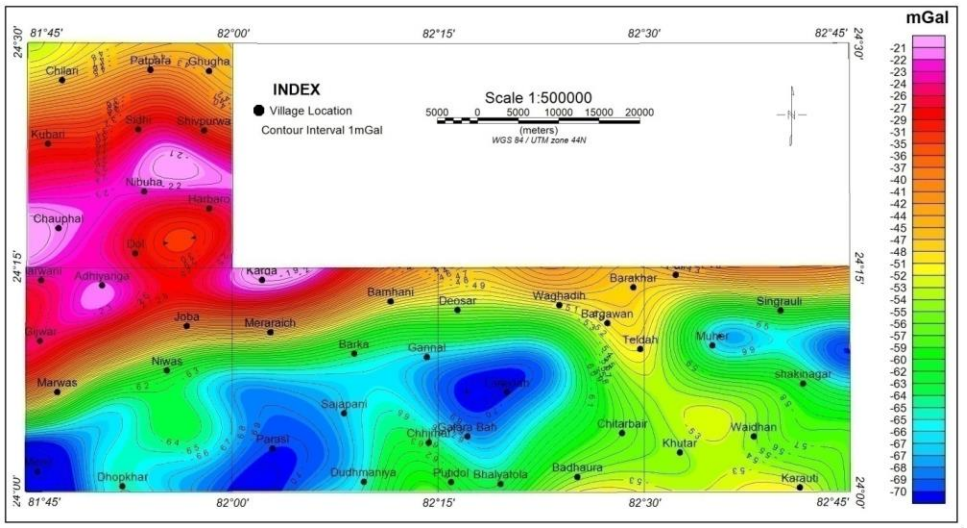

Figure 5. Regional Bouguer gravity anomaly contour map.

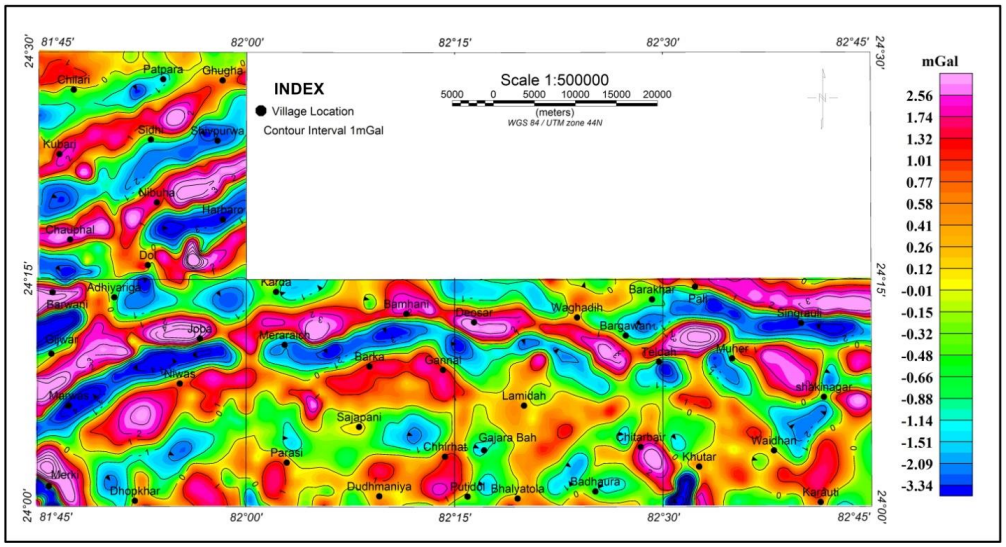

Figure 6. Residual Bouguer gravity anomaly contour map.

The regional magnetic map prepared using low pass filter resembles the original magnetic anomaly map (Figure 7). The low pass filter suppresses high frequency magnetic anomaly due to the near surface causative bodies, while the deeper sources are better resolved. The high regional magnetic anomaly is observed from northwestern to central and northeastern parts. The residual magnetic map using regional-residual separation technique, shows a number of local magnetic anomalies with different polarities and orientations (Figure 8). Several NE–SW magnetic anomalies are clearly shown in the northwestern part while NE-SW and NW-SE and E–W trending local anomalies appear enhanced over the rest of the area.

The total horizontal derivative and the tilt derivative

The derivative (total horizontal and tilt derivative) of potential field data is a powerful tool for identifying edges or boundary/ contact zone of formations, such as faults or igneous bodies (Awady et al., 2016, Lahti and Karinen, 2010). The total horizontal derivative appears

as a peak over the edges, while it is zero over the body (Awady et al., 2016, Miller and Singh, 1994). The total horizontal derivative (THDR) can be calculated using the standard formula of Verduzco et al. (2004) for potential field data:

$$THDR = \sqrt{\left(dT/dx\right)^2 + \left(dT/dy\right)^2} \qquad (1)$$

Where, T is the total intensity of the potential field data.

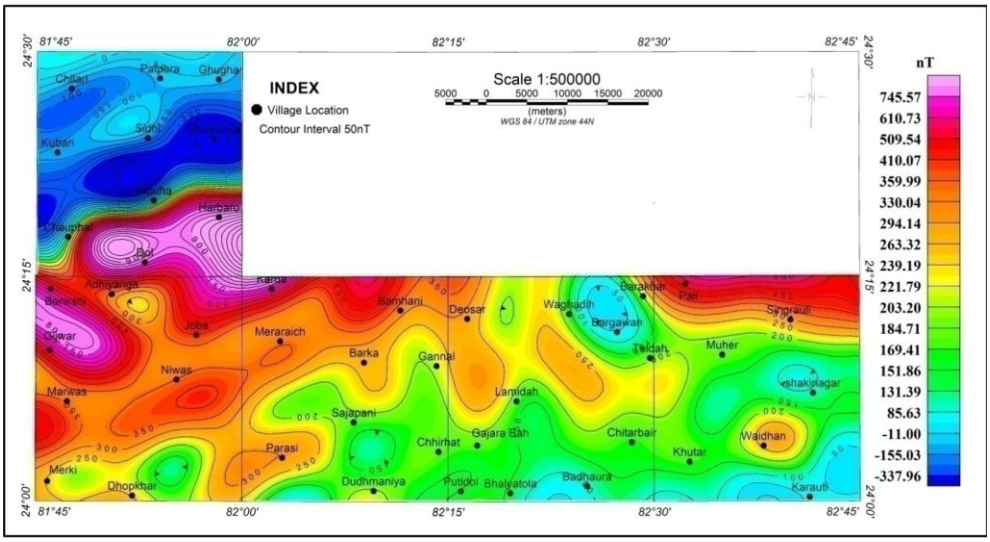

Figure 7. Regional Magnetic anomaly contour map.

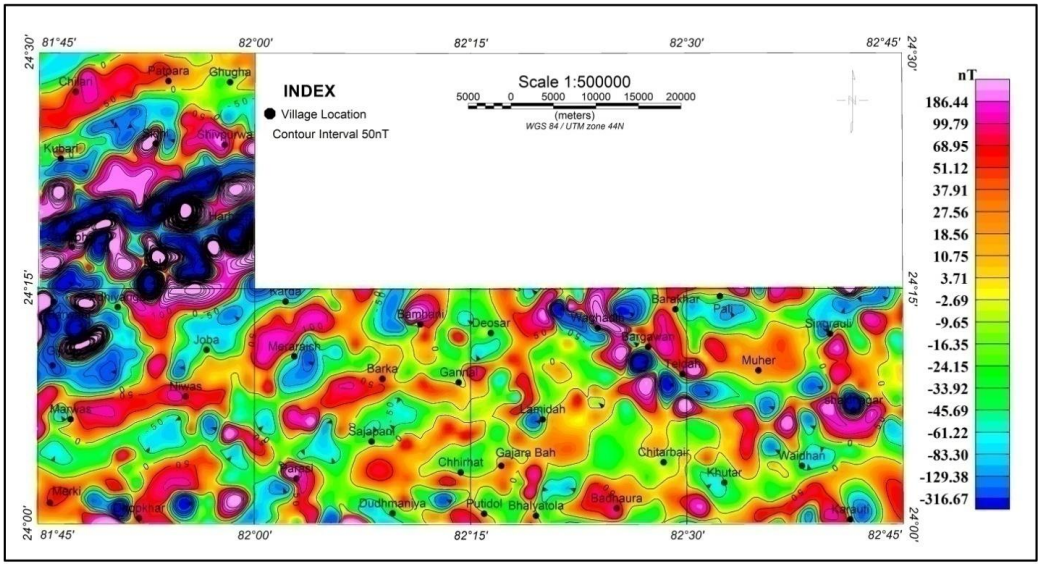

Figure 8. Residual Magnetic anomaly contour map.

The tilt derivative of the potential field is defined as the ratio of the first vertical derivative to the total horizontal derivative of the field. The tilt derivative (TDR) is positive over the source and close to zero at the edge, while it is negative outside the source. The method has a unique advantage over the other edge detectors in that it responses equally to shallow and deep sources (Awady et al., 2016, Miller and Singh, 1994).

The tilt derivative technique was applied to the gravity and magnetic data using the standard formula of Verduzco et al. (2004):

$$TDR = \tan^{-1}\left(VD/THD\right) \qquad (2)$$

The inferred fault/ contact zones (F1-F1' and F3-F3'), Amsi-Jiawan (F5-F5') and Jamui-Markundi (F6-F6'), are clearly reflected in THDR and TDR maps of gravity data shown in Figures 9 and 11. The THDR of the magnetic data shows magnetic maxima over the Mahakoshal formation and also at various scattered locations in the northeastern and central parts of the map (Figure 10). The map of the TDR of the magnetic data depicts close to zero magnetic values that coincide with edges or boundaries of inferred faults, such as Amsi-Jiawan (F5-F5') and Jamui-Markundi (F6-F6'), as shown in Figure 12.

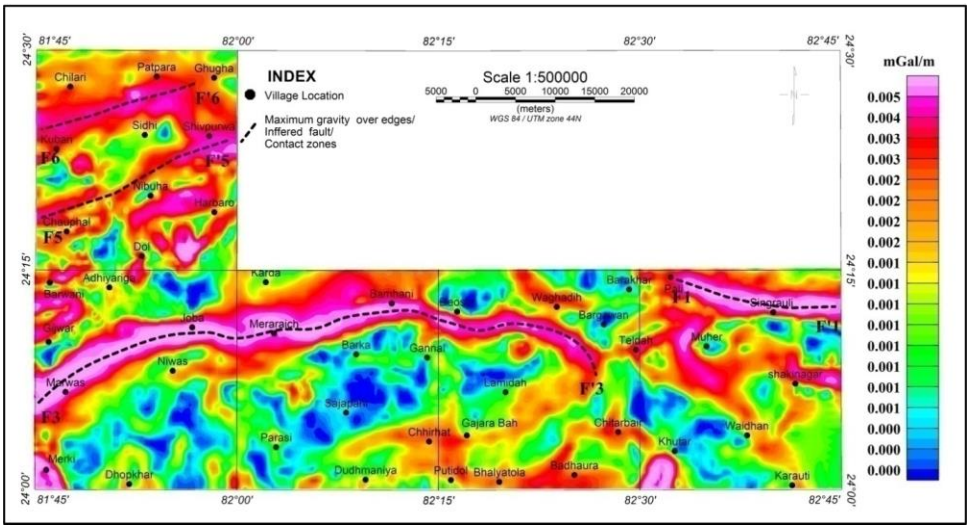

Figure 9. Total horizontal derivative of gravity data.

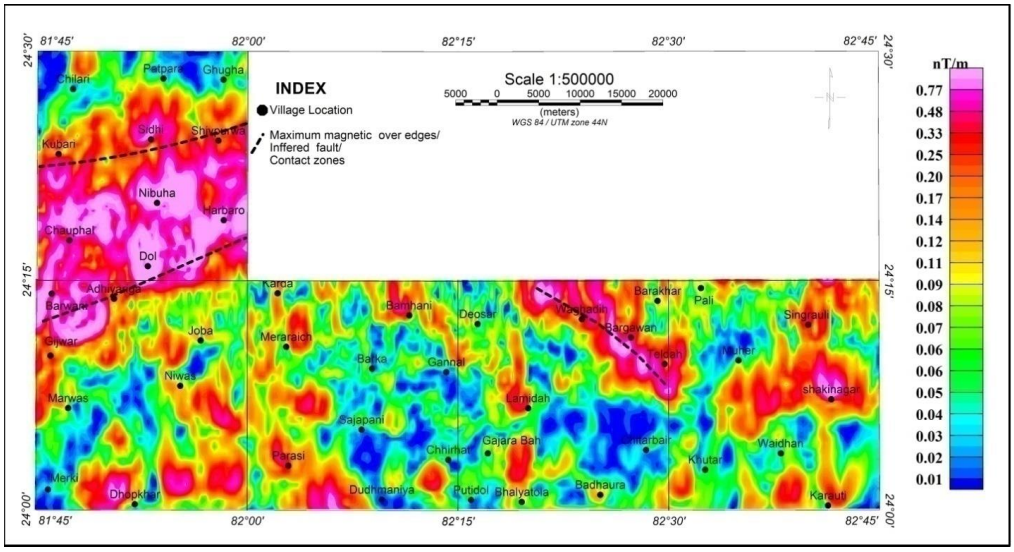

Figure 10. Total horizontal derivative of magnetic data.

Euler 3D Depth Solutions

Euler deconvolution can be used to estimate the depth for wide geological features such as faults, contacts and dykes. The method is best suited for anomalies, caused by isolated and multiple anomalous sources (El Dawi et al., 2004). The standard Euler 3D deconvolution method is based on Euler's homogeneity equation that helps to estimate the depth of causative sources, obtained from potential field data. The structural index (SI) is based on the geometry of the potential field data and is a measure of the rate of change of the anomaly with distance from the source. The cluster of Euler solutions around the perimeter of the bodies in a horizontal plane, provides estimates of the depth of causative sources (Thompson 1982).

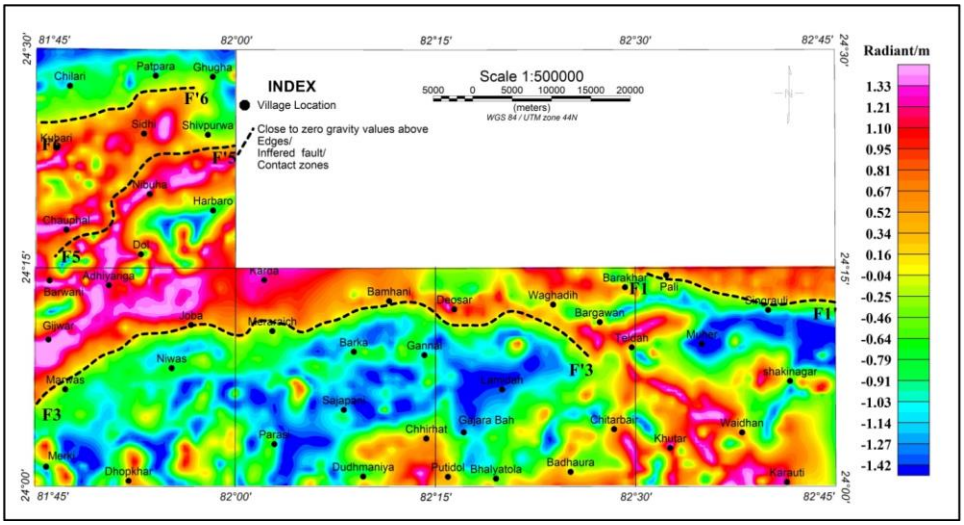

Figure 11. Tilt derivative of gravity data.

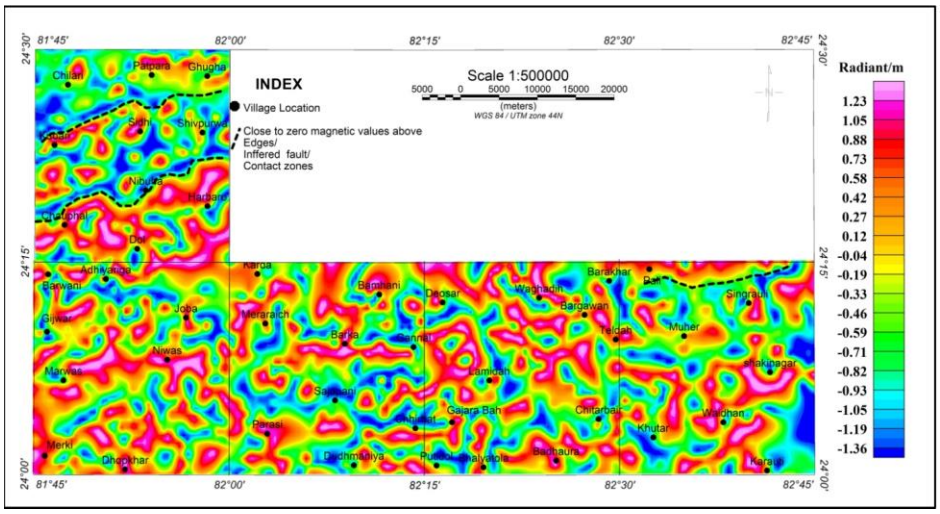

Figure 12. Tilt derivative of magnetic data.

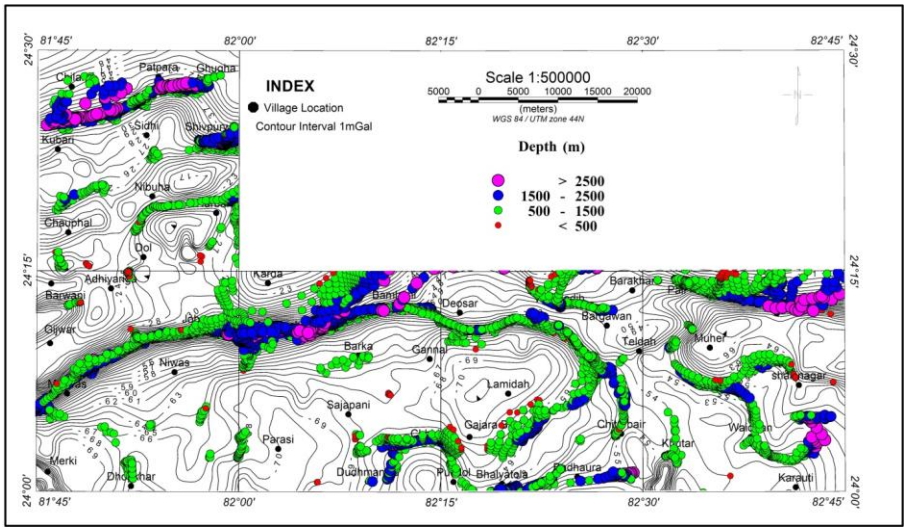

Figure 13. Euler 3D depth solutions of gravity data for SI = 0 (Kumar and Punekar 2018).

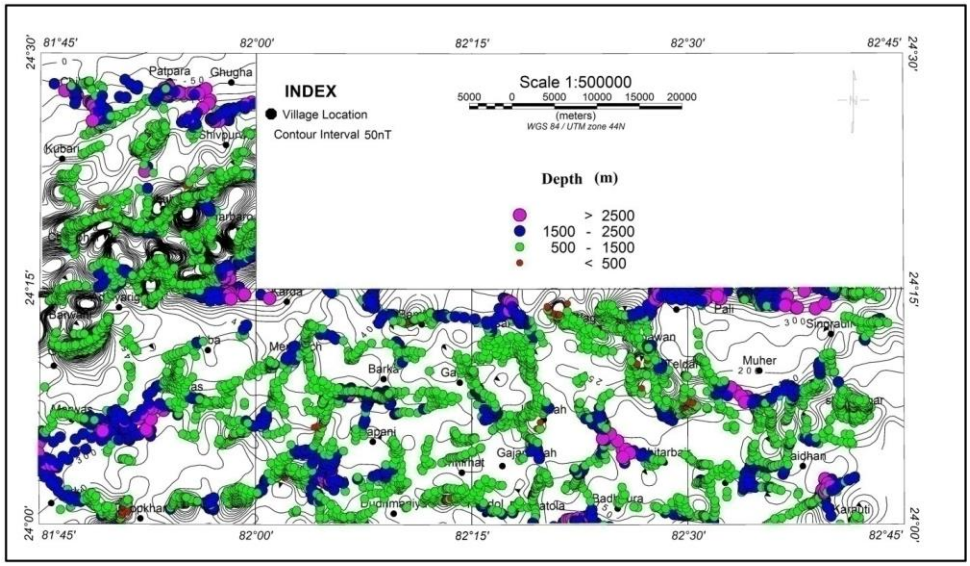

Figure 14. Euler 3D depth solutions magnetic data for SI = 1.

Euler solutions were determined using a window length of 5 km and SI = 0 for gravity and SI = 1 for magnetic data in order to emphasize the contacts and faults. The Euler depth solutions have yielded depths less than 0.5 km, 0.5 to 1.5 km, 1.5 to 2.5 km and beyond 2.5 km of gravity and magnetic data respectively, as shown in Figures 13 and 14. The majority of solution fall at contact between two litho-units varying depth from 0.5 to 2.5 km.

CONCLUSIONS

The structural features (inferred fault/ lineament/ contact zones) revealed in Bouguer gravity anomaly map, show a good correlation with the geological map. Magnetic anomalies of higher amplitudes are observed in northwestern part over metabasalt, biotite schist and banded iron formation (BIF), whereas magnetic anomaly of higher amplitude in the northeastern part is due to the concentration of the magnetite grains in biotite schist and phyllite. The regional gravity low is observed in northeastern, central and southwestern parts, covering sedimentary rocks of Gondwana formations. The high regional magnetic anomaly is observed from northwestern to central and northeastern parts. The inferred fault/ contact zone (F1-F'1 and F3-F3') and Amsi-Jiawan and Jamui-Markundi, are clearly reflected in THDR and TDR maps of gravity data, which correlate well with several gravity maps. The THDR of the magnetic data shows magnetic maxima over the Mahakoshal formation and also scattered pockets in the northeastern and central part of the map. The map of the TDR of the magnetic data, depicts close to zero magnetic values that coincide with edges or boundaries of inferred fault like Amsi-Jiawan and Jamui-Markundi. The Euler depth solutions corroborate well with the inferred structural features.

ACKNOWLEDGEMENT

The authors express their sincere gratitude to Shri S. Natesan, Additional Director General and HOD, Geological Survey of India, Central Region, Nagpur for providing all logistics to carry out the work. We are thankful to senior of Geophysics Division for the support and suggestions. We are thankful to the reviewers, Publication Division of GSI, CR, Nagpur who have given critical and thoughtful suggestions.

Compliance with Ethical Standards

The authors declare that they have no conflict of interest and adhere to copyright norms.

REFERENCES

Auden, J.B., 1933. Vindhyan sediments in the Son valley, Mirzapur district, Mem. Geol. Surv. India, 62(2), 141-250.

Awady, M.M., Badrawy, H.T., Abuo, A.M., Solimaan, M.R., Alrefaee, H.A. and Elbowab, M., 2016. Integrated geophysical studies on the area east of Abu Gharadig basin, southern Cairo, Egypt, using potential

field data, NRIAG Journal of Astronomy and Geophysics, 5, 351–361.

Bharati, S.K., Ramachandrappa, and Hanmanthu, D., 2016. A Report on geophysical mapping in Toposheet nos. 64L/1, 2, 3, 4, and 64H/15, parts of Raipur, Dhamtari Districts, Chhattisgarh, Unpub. Report, GSI, CR.

Chaubey, V.D., 1970. Narmada Son line. Thrust, the Great Boundary Fault along the southern margin of Vindhyan basin, Central India, West commemoration volume. Today and Tomorrow's Printers and Publishers Faridabad, 420-438

El Dawi, M.G., Tianyou, L., Hui, S. and Dapeng, L., 2004. Depth estimation of 2-D magnetic anomalous sources by using Euler deconvolution method. Am. J. Appl. Sci., 1(3), 209–214.

Gorle, R., Anusha, Y. and Hanmanthu, D., 2016. A Report on geophysical mapping in toposheet nos. 64H/6, 9, 10, 13, and 14, parts of Raipur, Districts, Chhattisgarh, Unpub. Report, GSI, CR, 2016.

Jha, D.K., Banerjee, S.K. and Narain, A., 1980. Systematic geological mapping of the area around Dudhamaniya, Singrauli Tehsil, Sidhi district, M.P, Unpub., Report, GSI, India, 1980.

Jha, D.K. and Devarajan M.K., 2002a. The large scale mapping and regional geochemical sampling of the area around Chanariya gold prospect, Sidhi district, M.P., Unpub., Report, GSI, India.

Jha, D.K. and Devarajan, M.K., 2002b. Preliminary exploration for gold in Chakariya block, Sidhi district, M.P., Unpub., Report, GSI, India.

Kumar, R. and Punekar D.V., 2018. Significance of regional gravity survey in parts of Sidhi and Shahdol districts, M.P., J. Indian Geophys. Union, 22(5), 478-484.

Lahti, I. and Karinen, T., 2010. Tilt derivative multiscale edges of magnetic data. Lead. Edge 29, 24–29.

Majumdar, M., 1980. Geology of Sarai-Bharsera area, north western part of Singrauli coalfield, Sidhi district, Madhya Pradesh, Unpub., Report, GSI, India, 1980.

Miller, H.G. and Singh, V., 1994. Potential field tilt—a new concept for location of potential field sources. J. Appl. Geophys., 32, 213–217.

Pandhare, S.A., 1972. The systematic geological mapping in parts of Gopad-Banas Tahsil, Sidhi district, M.P., Unpub., Report, GSI, India, 1972.

Subramanyam, B., Sankaram, S.P. and Ghatak, S.K., 1972. Geophysical investigations for Sulphide ores in Guriara area, Sidhi district, M.P., Unpub., Report, GSI, India.

Subrahmanyam, B., Sankaram, S.P., Ghatak, S.K. and Khotpal, A.S., 1975. Geophysical investigations for sulphide ores in Byria-Bahertola area Sidhi district, M.P., Unpub., Report, GSI, India.

Thompson, D.T., 1982. EULDPH: A new technique for making computer Assisted depth estimates from Magnetic data, Geophysics, 47, 31-37.

Verduzco B., Fairhead J.D., Green C.M. and MacKenzie C., 2004. New insights into magnetic derivatives for structural mapping. Lead. Edge, 23, 116–119.

Received on: 21.1.19; Revised on: 15.5.19; Accepted on: 18.5.19

The growth of magnetization minerals with a rise in temperature

Victor V. Onufrienok

Krasnoyarsk Agrarian University, E. Stasova Street, 44. Krasnoyarsk, Russian Federation

Email: VOnufriynok@yandex.ru

ABSTRACT

Magnetic properties of iron sulfides in a metastable phase state were investigated. During heating of iron sulfides of the composition $Fe_{0.901}S$ up to ~150°C, a magnetization increase was observed. It was shown that the observed effect is not the known γ- transition and that it results from the redistribution of vacancies of iron ions in basal planes of the crystal structure of the NiAs type. A theoretical model was proposed which explains qualitatively this effect.

Keywords: molecular-field model, exchange interactions, magnetization, magnetic field.

INTRODUCTION

Chalcogenides are of some interest from the point of view of studying vacancies. The number of vacancies in their structure is determined by the composition, namely the formula unit. For example, the formula for pyrrhotite is represented as Fe_{1-n} S, where n is the number of vacancies, that is, the average number of vacancies per one iron atom (the density of vacancies). In addition, chalcogenides can be used to study the ordering of vacancies in a structure, with a long-range magnetic order. Magnetic properties in nonstoichiometric ferrimagnets are closely related to the distribution of cation vacancies in the structure [Schwars and Vaughan, 1972, Onufrienok, 2005, Makovicky, 2006, Mashukov et al., 2007]. For example, in the structure of pyrrhotite, a ferromagnet spin ordering is realized in the basal planes and an antiferromagnet order is realized in the neighboring planes.

In natural minerals of the composition $Fe_{0.875}S$—$Fe_{0.909}S$ (pyrrhotines), the temperature dependence of magnetization exhibits a series of specific features. For instance, the γ- transition manifests itself in a sharp change of magnetization at temperatures 220-280°C (Schwars and Vaughan, 1972). Low temperature (T = 45 K) changes of magnetization were observed in synthetic iron sulfides (Zvegintsev et al., 1982). In ferrimagnetic iron sulfides, one observes the so-called temperature magnetic hysteresis, i.e., the difference between the magnetization before and after thermal treatment. Such a behavior of magnetization is determined not only by the γ transition but also by other, hitherto still little studied, phenomena (Onufrienock et al., 1981).

The magnetization of a ferrimagnets often behaves strangely when it is heated. It can, for example, increase over a certain temperature range, with no changes in the structure occurring. For example, Zvegintsev and Onufrienok (1981), Onufrienock and Zvegintzev (1981), Onufrienok (1991), Rickard and Luther (2007) described the anomalous magnetization behavior during growth temperatures for various reasons, related to crystallization and exchange interactions. Natural pyrrhotite $FeS_{1.14}$ is a heavily-doped [Onufrienok et al., 1982, Wang and Salveson, 2005, Dorogina, et al., 2015] ferrimagnet semiconductor with a distorted NiAs structure, in which successive planes perpendicular to the c-axis are occupied exclusively by iron atoms with their magnetic moments antiferromagnetically aligned. The iron vacancies are ordered in every second plane forming a superstructure (Kuzmin and Onufrienok, 1983, Lilies and de Villiers, 2012) and making the compound ferrimagnetic. As a result of X-ray studies, it is established that the crystal structure remains hexagonal of the NiAs type (Ward, 1970, Koto, et al. 1975, Morimoto, et al. 1975, Onufrienok 2013). Since antiferromagnetic spin ordering is realized in adjacent basal planes, the effect of increasing magnetization on the ordering of vacancies in even (odd) basis planes is practically obvious, but this is not noted in these experiments. We note that the total magnetic moment consists of the sum of the moments of the sublattices.

The aim of this work is to investigate the temperature changes of magnetization of pyrrhotines in a metastable phase state, which exhibit a temperature magnetic hysteresis, and also to explain these changes within the framework of existing theoretical models. Also describe the growth of the magnetization of ferrimagnetic materials with increasing temperature within the framework of the molecular field model. The anomalous behavior of the magnetization is explained by the change in the magnitude of the magnetic field and the corresponding values of the integrals of the exchange interaction and the spin operators.

SAMPLES AND METHODOLOGY

The sample for the study were obtained both by the method of dry synthesis (series A) and by decomposition in vacuum of pyrite (FeS_2) at different temperatures (series B). Following synthesis, the samples were annealed at different temperatures, quenched, and investigated with a thermoballistic apparatus in a field of 1 kOe. The chemical composition and the crystal structure of the samples were analyzed with a DRON-3 x-ray diffractometer according to the procedures described in the literature (Schwars et al., 1972).

The objects of the research were pyrrhotites, obtained as a result of high-temperature decomposition of environmental monocrystal pyrite, in a low vacuum condition (10^{-2} Pa). Samples were made by calcinating pyrite in quartz ampoules. Calcination of pyrite was carried out at the temperature from 400 to 1200°C for 1 hour. Two series of samples were studied. Samples of the A series after annealing were quenched in running water, and the samples of the B series were slowly cooled at a rate of 20 min to 20°C.

Nuclear Gamma Resonance spectra were recorded on a spectrometer with a uniformly moving source of Cr (^{57}Co) activity of about 20 μCi in the temperature range 77-300 K. The crystal structure of the samples was studied by X-ray fluorescence analysis and X-ray photoelectron spectroscopy, using Co (K_α) radiation, as well as various thermomagnetic methods. The speed of the diffraction patterns was 1 min in continuous mode and 0.001 sec in discrete mode. The diffraction pattern was taken using a β-radiation filter from iron.

RESULTS AND DISCUSSION

Typical curves at different temperatures are presented in figure 1. The dependence of I/I_o on T of a sample from series B with composition $Fe_{0.875}S$ is shown in Figure 1. Curves 1 and 2 correspond respectively to heating and cooling the sample at the rate of 10°/min. It is clear from Figure 1 (curve 1), that some increase of the relative magnetization occurs at ~150°/min. We note that the observed change differs from the familiar γ- transition in the shape of the λ- peak and in the low-temperature behavior, and is observed only in iron sulfides in a metastable phase state. The sample was obtained at 950°C followed by quenching to 0°C. It was subsequently annealed at 350°C, quenched again, and kept at room temperature for seven days.

An increase in the relative magnetization (I/I_0) occurs in the temperature range of 0-150°C with heating of the pyrrhotite of the composition $Fe_{0.875}S$ (Zvegintsev, et al. 1982). The peak on this curve at 150°C can be explained within the framework of the molecular-field model. This phenomenon will be observed in more detail later on.

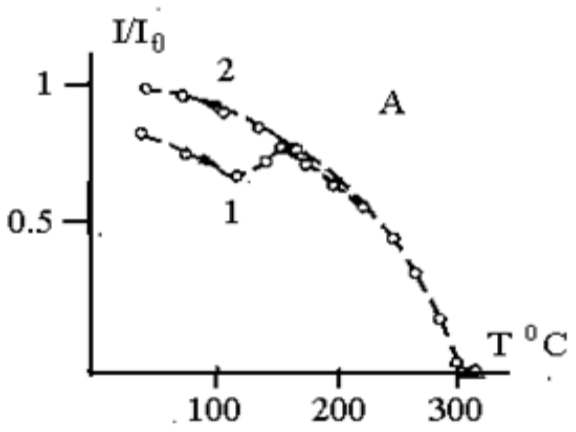

Figure 1. The growth of magnetization of a ferrimagnetics with a rise in temperature.

The NGR spectrum of pyrrhotite $Fe_{0.875}S$ in both the initial (A) and final (B) states, consists of four partially resolved sixtuplets (Figure 2), with field values on the nuclei of four sublattices equal to 24032, 21884, 20053, 18064 A/m. These field values are close to those calculated for the positions of iron ions without vacancies, with one, two, and four vacancies in the second coordination sphere, respectively. Such a configuration of a vacancy arrangement corresponds to an ordered state of vacancies in the even basis planes of the structure, however, the occupancy of the positions in the initial (A) and final state (B) is different. The final state (B) is characterized by a greater degree of ordering of vacancies.

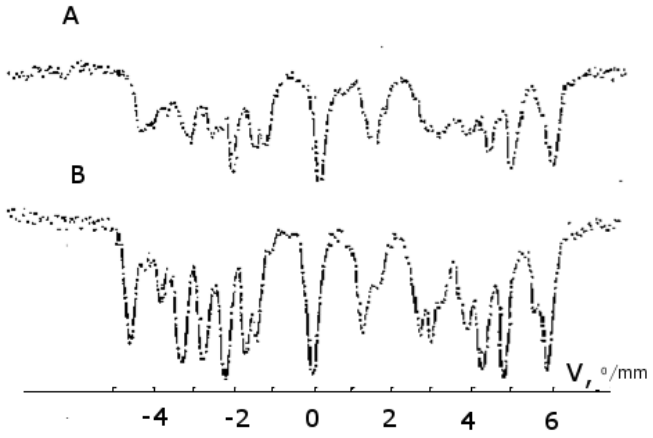

Figure 2. NGR spectra of pyrrhotite in the initial state (A) and after heat treatment (B)

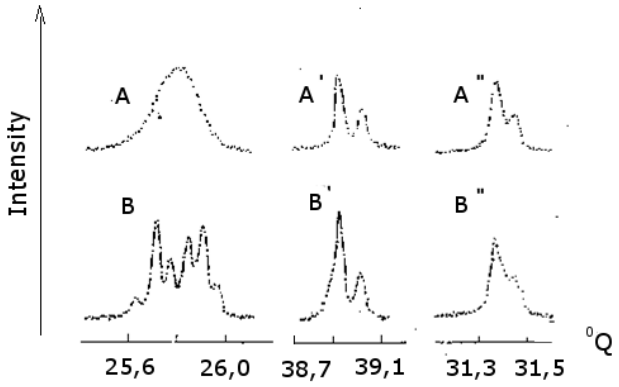

Figure 3. X-ray spectra reflexes with Miller indices (102), (004) and (110) of pyrrhotite in the initial state (A, A´, A") and after up to 300°C (B, B´, B").

The crystal structure (Figure 3) in this region of modes changes hexagonal (A) to monoclinic (B).

To explain the results, we use the quantum-mechanical model of a four-sublattice ferrimagnet. In a two-sublattice ferrimagnet, part of the ions near which the vacancies are located, have a local magnetic field value different from the rest of the ions in the node. This is due to the fact that in the formation of a superstructure, these ions are ordered in a certain way on account of the cation vacancies ordering. Consequently, a two-sublattice ferrimagnet can already be considered as a three-, four-, and so on, sublattice ferrimagnet, depending on the type of the vacancy ordering. Such a ferrimagnet will have a number of significant differences from the ordinary two-sublattice ferrimagnet. For example, interactions between sublattices may be missing or may be very small.

For further analysis of the magnetization behavior, it is necessary to consider separately the exchange interaction between cations in a nonstoichiometric ferrimagnet. We can clearly see that in this case, it is necessary to take into account not only in which plane the atom is located, but also the first coordination sphere of the given atom crystal structure. Thus, it is necessary to consider at least four types of exchange interaction. We apply to the algorithm described in (Tyablikov, 1975).

Let us denote by f, g, k, l the nodes of the first, second, third and fourth sublattices.

The quantities related to the first, second, third, and fourth sublattices will be denoted by 1, 2, 3, and 4.

We denote by N_i , S_i , μ_i the number of atoms in the sublattice, the magnitude of the spin, and the magnetic moment of the type i atom.

In general case

$$N_1 \neq N_2 \neq N_3 \neq N_4, \qquad S_1 \neq S_2 \neq S_3 \neq S_4, \qquad \mu_1 \neq \mu_2 \neq \mu_3 \neq \mu_4, \tag{1}$$

so that the magnetic moments of the sublattices are different.

We write the Hamiltonian system in the form:

$$\begin{aligned}\tilde{H} = {} & \mu_1 \sum(H, S_f) - \mu_2 \sum(H, S_g) - \mu_3 \sum(H, S_k) \\ & - \mu_4 \sum(H, S_l) \\ & - \frac{1}{2}\sum I(f_1 - f_2)\left(S_{f_1}, S_{f_2}\right) \\ & - \frac{1}{2}\sum I(g_1 - g_2)\left(S_{g_1}, S_{g_2}\right) \\ & - \frac{1}{2}\sum I(k_1 - k_2)\left(S_{k_1}, S_{k_2}\right) \\ & - \frac{1}{2}\sum I(l_1 - l_2)\left(S_{l_1}, S_{l_2}\right) \\ & - \sum I(f - g)\left(S_f, S_g\right) \\ & - \sum I(k - l)\left(S_k, S_l\right) - \sum I(g - k)\left(S_g, S_k\right) - \\ & \sum I(f - k)\left(S_f, S_k\right) - \sum I(f - l)\left(S_f, S_l\right) - \\ & \sum I(g - l)\left(S_g, S_l\right)\end{aligned} \tag{2}$$

where S_f, S_g, S_k, S_l are the spin atom operators of the first, second, third and fourth sublattices.

Taking into account the condition for a minimum in free energy.

$$F = -\vartheta \ln Q \tag{3},$$

the statistical sum is given by

$$Q = \sum_n e^{-E_n/\vartheta} = Sp\left(e^{-\frac{H}{\vartheta}}\right) \tag{4}$$

where E_n is the n eigenvalue of Hamiltonian $\tilde{H}$, considering that the magnitude of the canonical distribution is $\vartheta = \kappa T$, k is the Boltzmann constant, T is the temperature.

Passing on to the operators

$$S_f^Z, S_g^Z, S_k^Z, S_l^Z, S_f^{\pm}, S_g^{\pm}, S_k^{\pm}, S_l^{\pm} \tag{5}$$

and applying the Holstein-Primakov-Izyumov representations for spin operators in terms of second quantization operators

$$S_f^+ = \sqrt{2S}\varphi(n_f)a_f^-,$$

$$S_f^- = \sqrt{2S}\varphi(n_f)a_f^+ \tag{6}$$

$$S_f^Z = S - n_f, \tag{7}$$

$$\varphi(n_f) = \left(1 - \frac{n_f}{2S}\right)^{\frac{1}{2}} \tag{8}$$

$$n = a_f^+ a_f^- \tag{9}$$

the operators a^+ and a^- – satisfy the Bose commutation relations.

Assuming that the spins in either sublattice are parallel to each other, we obtain the set or molecular-field equations:

$$\begin{aligned}\alpha_1 &= \mu_1 H + J_{11}S_1\sigma_1 + |J_{12}|S_2\sigma_2 + |J_{13}|S_3\sigma_3 + |J_{14}|S_4\sigma_4 \\ \alpha_2 &= \mu_2 H + J_{22}S_1\sigma_1 + |J_{12}|S_2\sigma_2 + |J_{23}|S_3\sigma_3 + |J_{24}|S_4\sigma_4 \\ \alpha_3 &= \mu_3 H + J_{33}S_1\sigma_1 + |J_{32}|S_2\sigma_2 + |J_{13}|S_3\sigma_3 + |J_{34}|S_4\sigma_4 \\ \alpha_4 &= \mu_4 H + J_{44}S_1\sigma_1 + |J_{42}|S_2\sigma_2 + |J_{43}|S_3\sigma_3 + |J_{14}|S_4\sigma_4\end{aligned} \tag{10}$$

The relative magnetization of the Fe ions in the four sublattices is given by

$$\sigma_1 = 1 - S_1^{-1} B_{S_1}\left(\frac{\alpha_1}{Q}\right)$$
$$\sigma_2 = 1 - S_2^{-1} B_{S_2}\left(\frac{\alpha_2}{Q}\right)$$
$$\sigma_3 = 1 - S_3^{-1} B_{S_3}\left(\frac{\alpha_3}{Q}\right) \qquad (11)$$
$$\sigma_4 = 1 - S_4^{-1} B_{S_4}\left(\frac{\alpha_4}{Q}\right)$$

The system of equations represents the required equations of the molecular field for a four-sublattice isotropic ferrimagnet, where B_{Si} is the Brillouin function, and σ_i is the relative magnetization per site in the i -th sublattice.

Resultant magnetization:

$$M^Z = M_1^Z + M_2^Z + M_3^Z + M_4^Z \qquad (12)$$

$$M_i = N_i S_i \mu_i \sigma_i \qquad (13)$$

where σ_i is a fractional magnetization per one node in the sublattice.

The exchange integrals for the pyrrhotite were calculated in the molecular-field approximation, and its relative magnetization was determined as a function of temperature. Thus, within the framework of this model, it is easy to explain the behavior of the magnetization, if we take into account the values of the magnetic field and the corresponding integrals of the exchange interactions in the equations, as well as the spin operator.

It can be taken that $S_1 = S_2 = S_3 = S_4$ and $\mu_1 = \mu_2 = \mu_3 = \mu_4$.

Figure 4 presents two curves whose sum characterizes the behavior of the observed sample magnetization. Each of these two curves, in turn, is the sum of the magnetization of two sublattices with antiferromagnetic spin ordering. It is interesting that each of the curves presented in Figure 4 resembles the usual Weiss-type curve, while the total curve has features.

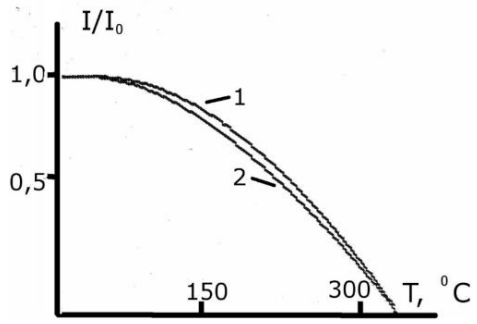

Figure 4. The magnetization curve 1 is the I (T) sum magnetization of 2x sublattices, with a larger value of the exchange integrals. Curve 2 represents the sum magnetization of two sublattices, for which the integrals of the exchange interaction are smaller than for curve 1.

Figure 5 shows the dependence of the sum magnetization 4^x-sublattice nonstoichio metric ferrimagnetics. Curve 1- 4 shows in originally ferrimagnet state corresponds to samples state with different ordering vacancies on the sublattices. As a result of different ordering of vacancies, the magnetic moments of the samples are different. Curve 5 is shown originally for an antiferromagnetic state with ordering vacancies on the sublattice. As the temperature increases, the sample converts to a ferrimagnet state in a certain region, and the ordering vacancies remains unchanged.

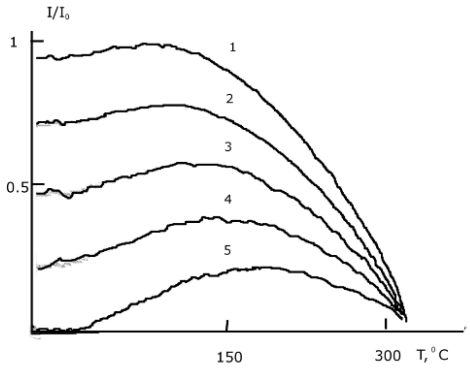

Figure 5. Resultant of magnetization of a sample increase in a certain region with increasing temperature.

CONCLUSION

In the framework of the four-sublattice ferrimagnet model, it was shown that the sample magnetization can increase with increasing temperature. This makes it possible to predict the magnetic properties of chalcogenides, containing point defects in the crystal structure. Within the framework of the molecular field approximation, a theoretical explanation is given for the dependence of the magnetization on the temperature of magnetically ordered compounds containing cationic vacancies in the crystal structure. On the basis of the proposed model of the behavior of vacancies, the theoretically possible dependences of the magnetization on temperature were presented.

Compliance with Ethical Standards

The author declares that he has no conflict of interest and adheres to copyright norms.

REFERENCES

Dorogina, G.A., Gulyaeva, R.I., Selivanov, E.N. and Balakirev, V.F., 2015. Thermal and thermomagnetic properties of pyrrhotites, Russian Journal of Inorganic Chemistry, 60, 349, (in Russian)

Koto, K., Morimoto, N. and Guybu, A., 1975. The superstructure of the intermediate pyrrhotite, Acta Cryst., B 31, 2759-2771.

Kuzmin, E.V. and Onufrienok, V.V., 1983. Magnetization of pyrrotine type non-stoichiometric compounds with the different vacancy concentration, Fizika Tverdogo Tela, 25, 2321-2326, (in Russian).

Lilies, D.C. and de Villiers, J.P.R., 2012. Redetermination of the structure of 5C pyrrhotite at low temperature and at room temperature, American Mineralogist, 97, 257-261.

Mashukov, A.V., Onufrienok, V.V. and Mashukova, A.E., 2007. The model of the four-sub-grate ferrimagnetic. Geochimica et Cosmochimica Acta. 71, A632-A632.

Makovicky, E., 2006. Crystal structures of sulfides and other chalcogenides, Reviews in Mineralogy and Geochemistry, 61, 7-125.

Morimoto, N., Gyobu, A., Mukaiyama, H. and Izawa, E., 1975. Crystallography and stability of pyrrhotites, Economic Geol., 70, 824-833.

Onufrienock, V.V. and Zvegintzev, A.G., 1981. Temperature magnetic hysteresis of pirrotines, Geomagnetizm i Aeronomiya, 21, 575-577, (in Russian).

Onufrienok, V.V., 2005. Metastable iron sulfides. Inorganic materials. 41, 650-653.

Onufrienok, V.V., 2013. Antagonism of phases in multi-component mixtures, Vestnik of SibGAU, 1, 162-166, (in Russian).

Onufrienok, V.V., 1991. Phase relationships of iron sulfides in the metastable state, Solid State Physics, 33, 2213-2215, (in Russian).

Onufrienok, V.V. and Zvegintsev, A.G., 1982. Magnetic-properties and crystal-structure of iron sulfides in the composition range FeS-$FeS_{1.18}$, Inorganic Materials, 18, 301-304, (in Russian).

Rickard, D. and Luther, G., 2007. Chemistry of Iron Sulfides, Chem. Rev., 107, 514-565.

Schwars, E.J. and Vaughan, D.I., 1972. Magnetic phases relationship of pyrrhotite, Geomagn.Geoel., 24, 4-41.

Tyablikov, S.V., 1975. The quantum theory methods of magnetism. M., Nauka., 188, (in Russian).

Zvegintsev, A.G. and Onufrienok, V.V., 1981. Peculiarities of magnetic-properties of pirrotites, formed as a result of pirit decomposition, Geomagnetizm i Aeronomiya, 21, 763-765, (in Russian).

Zvegintsev, A.G., Onufriyenok, V.V. and Petrov, M.I., 1982. The effect of the synthesis conditions and heat-treatment on the magnetic-behavior of iron sulfide. Izvestiya Akademii Nauk SSSR Fizika Zemli, 4, 83-87.

Wang, H. and Salveson, I., 2005. A review on the mineral chemistry of the non-stoichiometric iron sulphide, $Fe_{1-x}S$ ($0 \leq x \leq 0.125$): polymorphs, phase relations and transitions, electronic and magnetic structures, Phase Transitions, 78, 547-567.

Ward, J.C., 1970. The structure and properties of some iron sulfides, Rev. Pure. Appl. Chem., 20, 175-191.

Received on: 7.2.19; Revised on: 23.5.1; Accepted on: 28.5.19

Multivariate Statistical Approach for Evaluating Groundwater Quality in Sathyavedu Area, Chittoor District (Andhra Pradesh, India)

G. Veeraswamy[1*], E. Balaji[1], A. Nagaraju[1], and Brijesh Kumar Yadav[2]

[1]Department of Geology, Sri Venkateswara University, Tirupati, Andhra Pradesh,
[2]Department of Hydrology, IIT Roorkee, Roorkee – 247667 (Uttarakhand),
*Corresponding author: veeraswamygolla33@gmail.com

ABSTRACT

The aim of the present study is to identify the geochemical processes and source of contaminants in Sathyavedu area using statistical methods such as factor analysis (both Q and R-modes) and hierarchical cluster analysis. A total of 39 groundwater samples were collected and analyzed for various physicochemical parameters. R-mode analysis refers to the correlation between the variables whereas; Q-mode refers to the linkage between the numbers of samples. Factor analysis has given nine factors and among all, the first five factors, was considered as they explain the possible sources of variance in the data sets, which were mainly attributed to the weathering process, rock-water interaction and the dissolution of sulphates and chlorides due to fertilizers and agricultural activities. Whereas, cluster analysis in R-Mode has 5 classes which are attributed to silicate weathering, overall impact of rock-water interaction and dissolution of chlorides and sulphates. The Gibb's diagram shows that all the samples fall in the rock-water interaction area. Hydrochemical facies (piper) indicates that about 90% of the samples belong to mixed Ca-Mg-Cl and the remaining 10% belongs to in Ca-Cl facies type. The normalized bivariate plot shows that the groundwater is influenced by the silicate weathering processes.

Keywords Factor Analysis (Q and R-modes), Gibbs diagram, Cluster analysis-R mode, Hydrogeochemistry, Piper diagram, Normalized bivariate plots, Chittoor district (Andhra Pradesh)

INTRODUCTION

Water is prerequisite for all the biotic components on the earth's surface. The biotic components depend on either surface or subsurface water (Veeraswamy et al., 2018). Groundwater is a renewable resource and while infiltrating into the ground, it can interact with the different kind of rocks, mineral, and soils. Some of the chemicals, easily disintegrated in water, leads to the form the aquifer pollutants and health hazards (National Research Council, 2000). As the name would suggest, multivariate analysis forms a set of techniques dedicated to the analysis of data sets with more than one variable. The origin and source of the pollutants in the groundwater can be a tool for reliable water resource management as well as remedies for the pollutants in the study area (Halim et al., 2010; Rahman and gagnon et al., 2014; Bhuiyan et al., 2015: Molla et al., 2015; Md. Bodrud-Doza, 2016; Veeraswamy., 2017; Nagaraju et al., 2017). The present study deals with the chemical quality of groundwater, contaminated by various factors, such as agriculture activity, household refuse, the residence time of groundwater, mixing of groundwater with saline water and anthropogenic impacts (Howladar et al., 2017). In fact, the study area is highly contaminated with the saline water due to salt water interaction with the fresh water apart from silicate weathering.

STUDY AREA

Sathyavedu is one of the important mandal in Chittoor District of Andhra Pradesh state (Figure 1).It is situated on the east coast towards the Bay of Bengal side and is bounded by Bangarupalem, Adhum, Appaihpalem, and Nagari mandals. This area is covered by survey of

India (SOI) toposheet No's. 57 O/14, O/15, 66 C/2, and C/3. It is located in between 13°20' N and 13°33' N latitudes 79°50' E and 79°59' E longitudes. According to the 2011 census, the Sathyavedu area has a population of 52,979. The majority of people of the study area depend on Arani River for potable water usage. The mean annual rainfall in the mandal is about 1187.8 mm. Lithologically, the rocks of Gondwana unconformable overlies the peninsular gneissic complex in the study areas which is represented by Sathyavedu formation (upper Gondwana) and comprised of mottled quartzite's and conglomerates. Laterite cappings occurring in Gondwana sandstones are also observed in the study area.

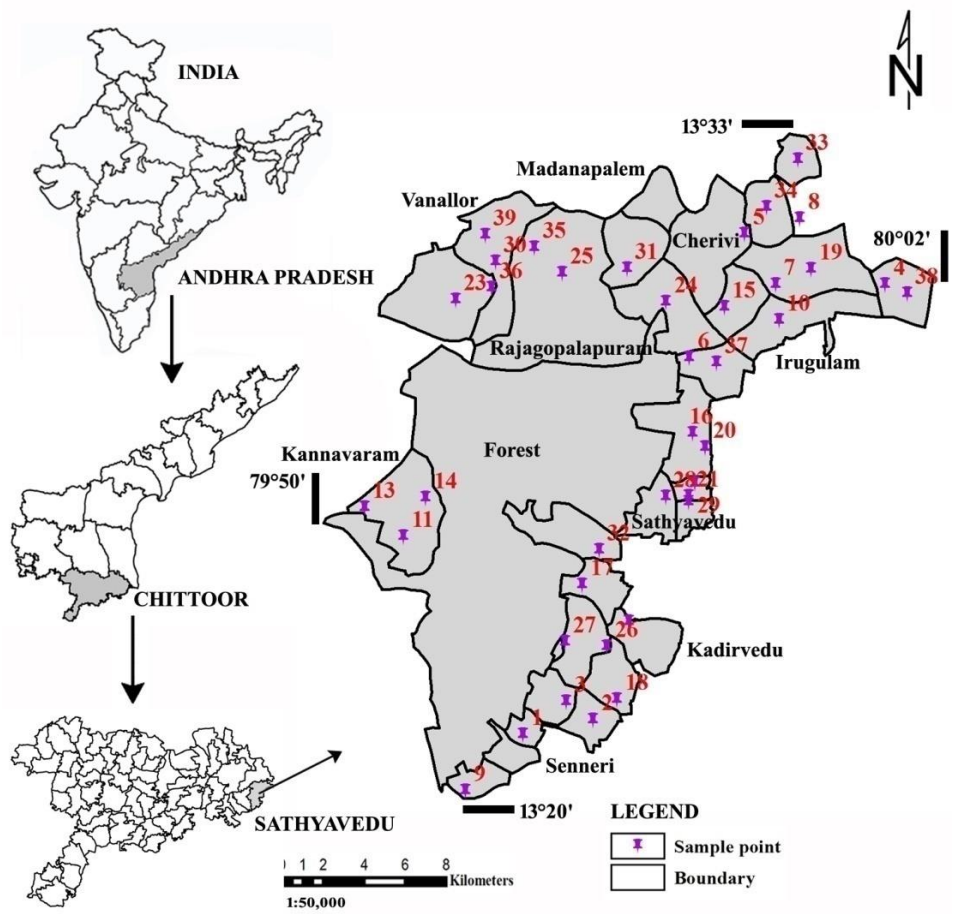

Figure 1. Location map of the study area

METHODOLOGY

The location map was prepared from the toposheet No's 57 O/14, O/15, 66 C/2 and C/3, with the help of ArcGIS10.1 software. The collected 39 water samples were analyzed for physicochemical parameters and major ion chemistry, such as pH, EC, TDS, TH, TA, $Ca^{2+,}$ Mg^{2+}, K^{+}, Na^{+}, HCO_3^{-}, CO_3^{2-} and F^{-}, using standard procedures (APHA, 2012). The outcome of the data was exported to the XL STATISTIC software to processes factor analysis (R-mode and Q-mode) and cluster analysis in R-mode. Moreover, Gibb's diagram, piper plot and bivariate plots were also prepared to know the key factors controlling the hydro geochemistry of the study area (table1).

Table 1. Minimum, maximum, standard deviation and average values of different constituents of water samples

S. No.	Constituents	Min	Max	Average	S.D	S.E
1	**Calcium (Ca^{2+}) (mg/l)**	16.00	180.00	79.70	43.40	6.14
2	**Magnesium (Mg^{2+}) (mg/l)**	9.00	408.00	83.98	70.00	9.90
3	**Sodium (Na^{+}) (mg/l)**	75.00	157.00	98.75	21.32	3.02
4	**Potassium (K^{+}) (mg/l)**	2.00	10.00	4.38	1.93	0.27
5	**Bicarbonate (HCO_3^{-}) (mg/l)**	35.00	125.00	75.92	26.92	3.81
6	**Carbonate (CO_3^{2-}) (mg/l)**	1.00	12.00	3.86	2.17	0.31
7	**Sulphate (SO_4^{2-}) (mg/l)**	2.00	80.00	37.23	22.71	30.00
8	**Chloride (Cl^{-}) (mg/l)**	23	510	148.905	112	15.82
9	**Fluoride (F^{-}) mg/l**	0.01	0.97	0.35	0.24	0.03
10	**Total dissolved solids (mg/l)**	66.95	923.65	437.89	249.66	35.31
11	**Hardness as $CaCO_3$ (mg/l)**	36.00	556.00	264.10	255	18.46
12	**Alkalinity as $CaCO_3$ (mg/l)**	40.00	600.00	278.85	240	22.46
13	**pH**	6.00	7.85	7.06	0.43	0.06
14	**Specific conductance (µmhos/cm)**	103.00	1421.00	673.68	384.10	54.32
21	**Gibbs ratio-I**	0.28	0.96	0.70	0.15	0.02
22	**Gibbs Ratio-II**	0.32	0.85	0.55	0.14	0.02

Processing of Data

The factor analysis was generated through XL STATISTICAL software. This procedure renders new rotated varimax factor. In that, each factor is interpreted as variables. From the factor analysis, it is found that the positively loaded variables are affected whereas negatively loaded factors are unaffected in the study area. Dalton and Upchurch (1978) have shown that factors can be related to the intensification of the chemical processes described by each factor. The high value of negative numbers (< -1) reflect the areas essentially unaffected by the process and positively score (> +1) indicates the high efficiency. The zero values show the average effect of the chemical process.

RESULT AND DISCUSSION

Factor analysis in R-Mode and Q-Mode

The first Factor (F1) shows a variance of 23.86%. It is positively loaded with EC, Ph, HCO3-, CO32-, Cl-, SO42-, F-, TDS, hardness and alkalinity. The variables are highly distributed in samples 7, 8, 9, 29, 31. The high concentrations of above parameters are due to rock-water interaction (granites, laterites), agriculture activities, household refuses (SO42-), and weathering of carbonate minerals. The main reason for salinity increase is due to saltwater intrusion in the study area (Rahman and Gagnon, 2014).

The Factor (F2) shows a variance of 13.560% and it's positively loaded with HCO3-, F-, Ph and alkalinity,

which were highly spread in samples 2, 34, 35, 38. The source of F2 is granite weathering and geogenic influence (Omo-Irabor et al., 2008; Veeraswamy et al., 2019). The main reason for elevated fluoride is due to the presence of the peninsular gneissic complex (PGC) and, apatite mineral which widely occurs here as an accessory mineral (Davis and Dewiest, 1966).

The Factor (F3) shows a total variance of 10.25 % and is positively loaded with Cl- only. The chloride is highly spread in samples 19, 20, 21 and 22.The main reason of elevated Cl- in groundwater is saltwater intrusion as the study area is located on the coast of Bay of Bengal.

The Factor (F4) shows a total variance of 8.361% and is positively loaded with Fluoride (F-), hardness and alkalinity. It is highly distributed in17, 18 and 23 samples. The main reason for this contamination is geogenic influence (Beaulieu and Savage, 2005; Levins and Gosk, 2008). The highlighted factor values are indicates strongly positive, negative commonality between variable in table 2, samples in table 3 and represents the source of pollution and ion's exchange processes .The minimum, maximum and average values of water quality parameters are given in Table 1.

Table 2. R-mode factor analysis - Eigen values and percent variability

Variables	**F1**	**F2**	**F3**	**F4**	**F5**
EC	0.650	**-0.661**	-0.334	-0.010	-0.157
pH	0.306	**0.503**	0.247	-0.217	-0.262
Ca	-0.250	**-0.259**	0.230	-0.026	-0.013
Mg	-0.204	0.040	0.198	0.131	**-0.796**
Na	**-0.617**	-0.402	0.131	0.205	0.113
k	0.036	0.175	**-0.491**	0.255	0.096
HCO3	0.387	**0.522**	-0.497	-0.379	-0.034
CO3	0.018	0.194	**-0.342**	-0.175	-0.086
Cl	**0.557**	-0.167	0.472	-0.333	0.061
SO4	**0.495**	-0.058	0.339	-0.379	0.201
F	0.315	0.348	-0.019	**0.514**	0.087
TDS	0.650	**-0.661**	-0.334	-0.009	-0.157
Hardness	**0.811**	0.079	0.264	0.463	0.028
Alkalinity	**0.673**	0.204	0.170	0.301	0.025
Eigenvalues					
	F1	**F2**	**F3**	**F4**	**F5**
Eigenvalue	3.341	1.898	1.436	1.171	0.836
Variability (%)	23.861	13.560	10.255	8.361	5.973
Cumulative %	23.861	37.421	47.675	56.037	62.010

Table 3. Q- Mode analysis of water samples

No of water samples	F1	F2	F3	F4	F5
1	1.279	-0.300	**-1.477**	0.642	-0.180
2	0.280	**1.323**	-0.321	0.702	0.032
3	-0.505	0.270	0.881	-0.983	**1.396**
4	0.173	0.816	0.949	**-1.582**	0.583
5	0.567	0.822	-0.078	**-1.307**	0.058
6	0.208	0.256	0.783	**-0.950**	0.610
7	**1.299**	-0.127	-0.601	0.069	-0.274
8	**1.800**	0.267	-0.467	-1.488	-0.216
9	**1.968**	0.996	0.015	0.650	0.814
10	-0.393	-0.733	-0.294	-0.521	**-0.803**
11	**-2.223**	-0.944	-0.301	-0.058	1.148
12	**-1.681**	0.258	0.418	0.520	-0.059
13	**-1.968**	-0.675	-0.527	-0.085	0.265
14	-0.359	-1.229	**-1.324**	0.135	0.199
15	-0.723	**-1.749**	-1.183	-0.204	0.159
16	1.048	**-1.880**	-0.566	0.733	-0.371
17	0.050	1.337	1.660	**1.943**	0.498
18	0.906	-1.302	0.652	**2.531**	-0.410
19	0.547	-1.486	**1.645**	-0.014	-0.154
20	-0.746	0.395	**1.613**	1.008	0.002
21	-0.720	0.093	**1.346**	1.039	-0.127
22	0.429	-1.745	**1.976**	-1.744	-0.375
23	-0.863	0.512	0.654	**1.292**	0.115
24	-0.935	-0.263	0.644	0.497	**1.359**
25	-1.195	-0.176	-1.141	**-1.395**	-0.664
26	**-1.262**	1.114	0.247	-0.307	-0.552
27	-0.167	0.522	**-0.560**	0.072	-0.325
28	0.582	**-0.727**	-0.536	0.300	-0.155
29	**0.634**	-0.388	-0.168	0.527	-0.209
30	1.012	-0.240	**-1.248**	0.469	0.156
31	**0.783**	0.099	-0.682	0.656	-0.513
32	1.046	1.008	0.898	0.008	**1.104**
33	0.848	**-1.888**	-0.121	-0.869	-0.410
34	0.037	**0.882**	-0.154	-0.370	0.522
35	-0.133	**1.229**	0.372	-0.468	0.561
36	-0.954	0.546	**-1.725**	-0.700	0.758
37	-0.612	1.255	**-1.727**	-0.070	-1.126
38	0.495	**1.018**	-0.168	-0.264	0.713
39	-0.555	0.834	0.618	-0.413	**-4.132**

Cluster analysis (R-mode Dendrogram)

It is a type of technique framed to classify detecting observations to groups so that each one is more or less homogeneous and distinct from the other group (Hussain et al., 2008). The adaptation generates the dendrogram using a ward connection process, a correlation coefficient of similarity distance. The cluster analysis of dendrogram indicates pollution source of each cluster in the study area. The first cluster includes EC, TDS which is attributed to the impact of all ions in groundwater. The second cluster includes pH, Cl- and SO_4^{2-} which is attributed to dissolution of chlorides and sulphates (Kaown et al., 2009). The third cluster includes hardness and alkalinity which is a hardness controlled cluster. The 4th cluster comprises of K^+, HCO_3-, CO_3^{2-} and 5th cluster comprises of $Ca^{2+,}$ Mg^{2+} and Na^+ which are attributed to weathering of silicate minerals and action of atmospheric carbon dioxide in silicate weathering (Figure 2).

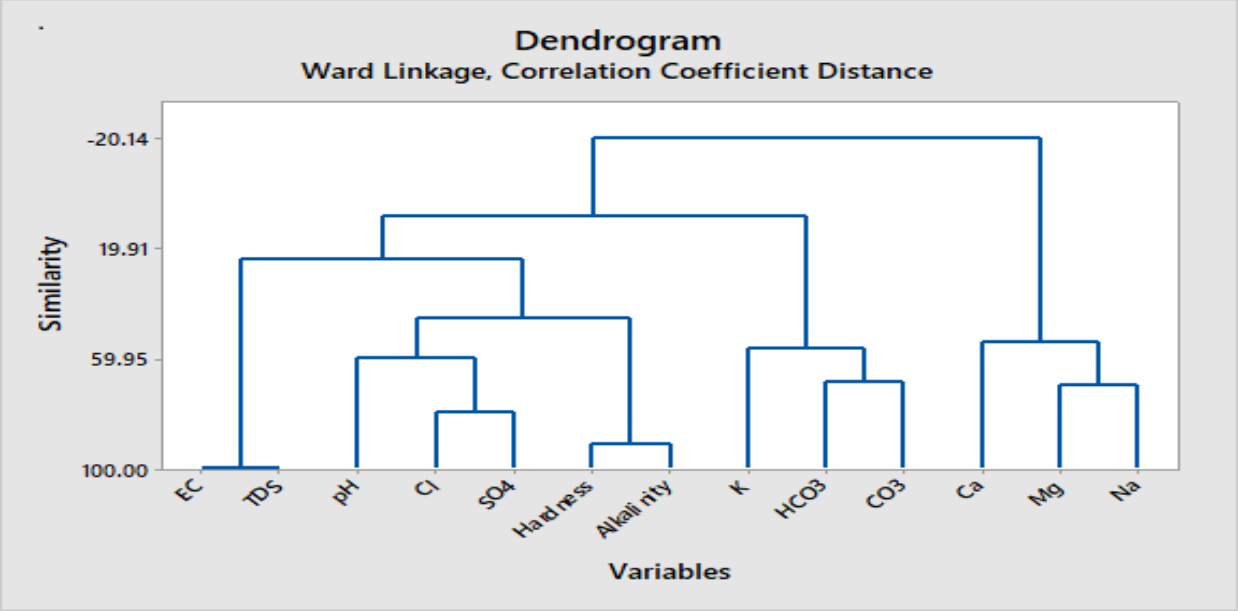

Figure 2. Dendrogram between variables

Hydrochemical facies

The general purpose of studying hydrochemical facies is to correlate the chemistry of groundwater with the lithological and hydrological environment.

Piper diagram and normalized bivariate plots

The groundwater facies were identified with the help of piper diagram (Piper, 1944). The geochemical evolution of groundwater can be obtained through Piper (1994) trilinear diagram is shown in Figure 3. These plots include two triangles, one for plotting cations and the other for plotting anions. The cations and anion fields are combined to show a single point in a diamond-shaped field, from which inference is drawn on the basis of hydro-geochemical facies concept. These tri-linear diagrams are useful in bringing out chemical relationships among groundwater samples in more definite terms rather than with other possible plotting methods. From this diagram, it is found that 90% samples fall in mixed Ca- Mg-Cl facies, while remaining 10%, fall in Ca-Cl facies type. Similarly, the normalized bivariate plots reveal that all the groundwater samples fall in the silicate weathering region (Figure 4), due to weathering of silicate minerals like biotite, chlorite, muscovite, talc, feldspars and amphiboles.

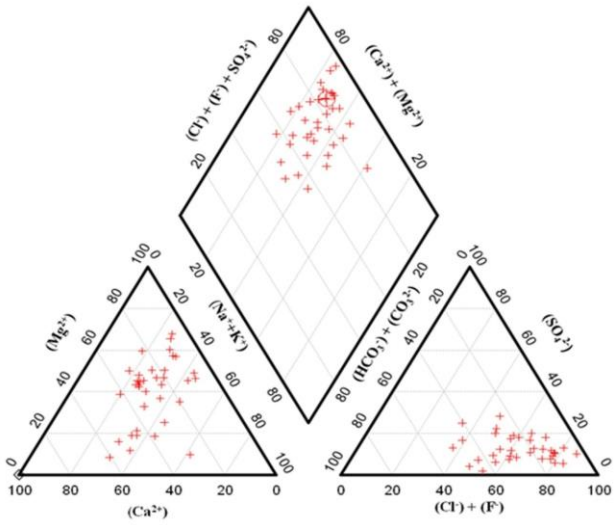

Figure 3. Piper Diagramme for descrimating hydro -geochemical facies

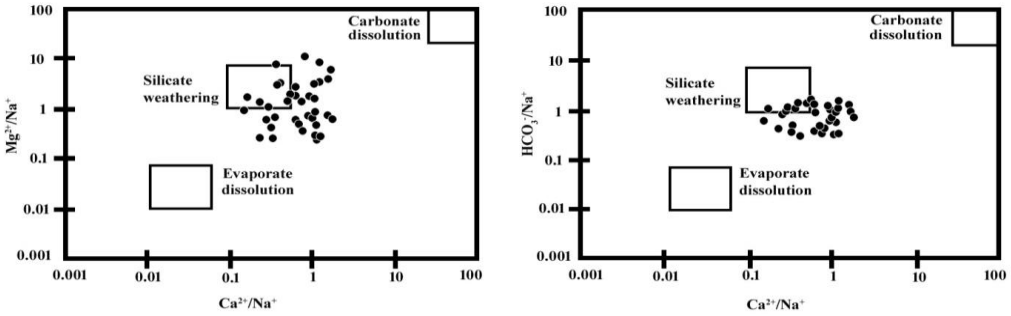

Figure 4. Normalized Bivariate plots

Gibb's Diagram

This Diagram is being extensively used to explain the relationship between water composition and aquifer lithological characteristics (Gibbs, 1970). The quality of groundwater is significantly distorted by the influence of weathering and anthropogenic inputs. The controlling mechanism of the surface water chemistry in terms of dissolved ions present in water like dominance of as evaporation-crystallization, rock weathering and atmospheric precipitation. Can be assessed by plotting hydrochemical data according to the variation in the ratios of $Na^+ + k^+/(Na^+ + K^+ + Ca^{2+})$ and $Cl^-/(Cl^- + HCO_3^-)$ as a function of TDS (Gibbs, 1970). This would provide meaningful information about the relative importance of major natural mechanisms controlling water chemistry (Figure 5).

The Gibbs ratios were calculated using the formulae:

Gibbs Ratio I (for anion) = $Cl^-/ (Cl^- + HCO_3^-)$

Gibbs Ratio II (for cation) = $(Na^+ + K^+) / (Na^+ + K^+ + Ca^{2+})$

Gibbs ratios for the groundwater samples were plotted against their respective total dissolved ions (Figure 5). Majority of the groundwater samples fall under the rock dominance area followed by evaporation dominance which suggests that the groundwater seems mostly to be controlled by chemical weathering of rock-forming mineral.

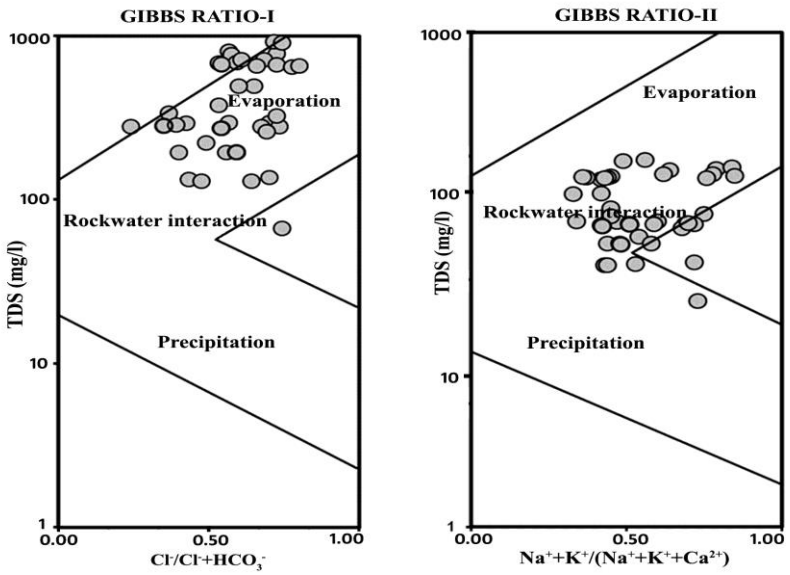

Figure 5. Gibb's Ratio Diagram.

CONCLUSION

In order to bring this study to a systematically organized conclusion, the analyzed groundwater samples were processed by factor and cluster analysis, which are reliable tools in groundwater studies while dealing with large data sets. The factor analysis reveals that most of the groundwater samples are highly contaminated with the sea water interaction induced salinity as the study area located on the coast of the Bay of Bengal. Secondly the groundwater samples are polluted with sulphates and chlorides due to the agriculture activity and household refuses. In addition to this carbonate and bicarbonates are released into aquifers due to the action of atmospheric carbon dioxide on the weathering of the peninsular gneissic complex. High TDS and EC values increased due to the dissolution of minerals in the study area. Analyzing the cluster 5 cluster are created. The data reduction techniques for instance the cluster and factor analysis, revealed that silicate weathering, dissolution of chlorides and sulphates and rock-water interaction, are the main processes governing the groundwater chemistry in the study area. The bivariate plots indicate the chemical elements released into the aquifer from silicate weathering processes. Piper diagram indicates that about 90% samples fall in mixed Ca- Mg-Cl and remaining the 10% fall in Ca-Cl facies type. Gibb's diagram shows that water has interacted has with the rock, as majority of samples fall in the field of rock-water interaction. The study concludes that the study area is heavily influenced and contaminated with the dissolution of silicate minerals, weathering processes and intrusion of sea water from the coastal aquifer. The data reduction techniques have help considerably in identifying the key governing factors, controlling the hydrogeochemistry of groundwater in the study area. Which may help decision makers in managing groundwater resources of the study area in a better way.

ACKNOWLEDGEMENT

I would like to thank Dr. A. Nagaraju, Professor of Geology, Sri Venkateswara University, Tirupati and Dr. Peiyue Li, professor, Chang'an University, School of Environmental Science and Engineering for supporting in my research work and anonymous reviewers, whose comments have greatly improved this manuscript.

Compliance with Ethical Standards

The authors declare that they have no conflict of interest and adhere to copyright norms.

REFERENCES

Kaila, K.L., Reddy, P.R., Mall, D.M., Venkateswarlu, N., Krishna, V.G. and Prasad, A.S.S.S.R.S., 1992. Crustal structure of the west Bengal Basin from deep seismic sounding investigations. Geophys. J. Int., 111, 45-66.

Beaulieu, B.T. and Savage, K.S., 2005. Arsenate adsorption structures on aluminium oxide and phyllosilicate mineral surfaces in smelter-impacted soils Environ. Sci. Technol., 39, 3571-3579.

APHA, 2012. Standard methods for the examination of water and wastewater, 22nd ed. American Public Health Association, New York.

Bhuiyan, A.H. Dampare, S.B., Islam, M.A. and Suzuki, S., 2015, Source apportionment and pollution evaluation of heavy metals in water and sediments of Buriganga River, Bangladesh, using multivariate analysis and pollution evaluation indices Environ. Monit. Assess., 187,4075, doi: 10.1007/s10661-014-4075-0.

Dalton, M.G. and Upchurch, S.B., 1978. Interpretation of hydrochemical facies by factor analysis. Ground Water, 16, 228-233. http://dx.doi.org/10.1111/j.1745-6584.1978.tb03229.x.

Davis, S.N. and Dewest, R.J., 1966. Hydrogeology. John Wiley and Sons, Inc. New York, 463.

Kaown, D., Koh, Dong-Chan, Mayer, B. and Kang-Kun Lee, 2009. Identification of nitrate and sulfate sources in groundwater using dual stable isotope approaches for an agricultural area with different land use (Chuncheon, mid-eastern Korea). Agriculture, Ecosystems and Environ., 132(3–4), 223-231, https://doi.org/10.1016/j.agee.2009.04.004.

Howladar, M.F., Al Numanbakth, M.A. and Faruque, M.O., 2017. An application of water quality index (WQI) and multivariate statistics to evaluate the water quality around maddhapara granite mining industrial area, Dinajpur, Bangladesh. Environ., Sys. Res., 6(1). doi:10.1186/s40068-017-0090-9

Gibbs R.J. (1970) Mechanism controlling world water chemistry. Science. 170, 1088–1090.

Halim, M.A., Majumder, R.K. and Nessa, S.A., 2010. Arsenic in the shallow aquifer in the eastern region of Bangladesh: insights from principal component analysis of groundwater compositions Environ Monit Assess, 161, 453-472. https://doi.org/10.1007/s10661-009-0760-9.

Hussain, M., Ahmad, S.M. and Abderrahman, W., 2008. Cluster analysis and quality assessment of logged water at an irrigation project, eastern Saudi Arabia. J. Environmental Manag, 86, 297-307.

Levins, I. and Gosk, G., 2008. Trace elements in groundwater as indicators of anthropogenic Impact. Environ. Geol, 55, 285–290.

Md. Bodrud-Doza, M., Towfiqul Islam, A.R.M., Ahmed, F., Das, S., Saha., N. and Safiur Rahman, M., 2016. Characterization of groundwater quality using water evaluation indices, multivariate statistics and geostatistics in central Bangladesh, Water Science, 30(1), 19-40, 1110-4929, https://doi.org/10.1016/j.wsj.2016.05.001.

Molla, M.A., Saha, N., Salam, S.A., and Rakib-uz-Zaman, M., 2015. Surface and groundwater quality assessment based on multivariate statistical techniques in the vicinity of Mohanpur, Bangladesh. Int. J. Environ, Health Eng., 4:18, DOI: 10.4103/2277-9183.157717.

Nagaraju A, Veeraswamy, G., Sridhar, Y. and Thejaswi, A., 2017. Assessment of groundwater quality in Gudur area of Andhra Pradesh, South India. Fresenius Environment. Bull., 26(5), 3597-3606.

National Research Council, 2000. A Review of the Draft of the NCI-CDC Working Group to revise the "1985 Radio epidemiological Tables" National Academy Press 2101.Constitution Avenue, NW, Washington DC, 2014.

Omo-Irabor, O.O., Olobaniyi, S.B., Oduyemi, K. and Akunna, J., 2008. Surface and groundwater water quality assessment using multivariate analytical methods: a case study of the Western Niger Delta, Nigeria. Phys. Chem. Earth, 33, 666–673.

Piper, A.M., 1944. A graphical procedure in the geochemical interpretation of water analysis. Trans .Am. Geophys .Union, 25, 914–923.

Rahman, M.S. and Gagnon, G.A., 2014. Bench-scale evaluation of drinking water treatment parameters on iron particles and water quality. Water Res, 48, 137–147.

Veeraswamy, G., Nagaraju, A., Balaji, E., Sridhar, Y. and Rajasekhar, A., 2018. Water quality assessment in terms of water quality index in gudur area, Nellore district, Andhra Pradesh. Int. J. of Technical Res. Sci., 3(1), 1-6, doi: 10.30780/IJTRS.V3.I1.2018.020.

Veeraswamy, G., Nagaraju, A., Balaji, E. and Sridhar, Y., 2017. Land use and land cover analysis using remote sensing and GIS: A case study in gudur area, Nellore district, Andhra Pradesh, India. Intr. J. Res, 4(17), 3145-3152.

Veeraswamy, G., Nagaraju,A., Balaji, E., Sreedhar,Y., Narasimhlu, K. and Harish, P., 2019. Data sets on spatial analysis of hydro geochemistry of Gudur area, SPSR Nellore district by using inverse distance weighted method in Arc GIS 10.1, Data in Brief, 22, 1003-1011, https://doi.org/10.1016/j.dib.2019.01.030.

Received on: 23.3.19; Revised on: 4.5.19; Accepted on: 14.5.19

Petrogenesis of A-type granite plutons of Gilkapadu and Ramreddipalem, area, Nellore Schist Belt, Eastern Dharwar Craton, India

Tushar M. Meshram[1*], Rajani Dharme[2], Sumit K. Mitra[3] and V.V. Sesha Sai[2]

[1]Petrology Division, Geological Survey of India, Central Region, Nagpur-440006 – India

[2] Geological Survey of India, Maharashtra, Central Region, Nagpur-440006 – India

[3] Director (Rtd.), Geological Survey of India, Southern Region, Hyderabad-India

*Corresponding author: tusharmeshram1984@gmail.com

ABSTRACT

We present the field, petrographic and geochemical characters of two thorite bearing A-type granite plutons that occur as detached bodies around Gilkapadu and Ramreddipalem (GR) in the southern part of the Neoarchean Nellore Schist Belt (NSB) of Eastern Dharwar Craton (India). These granites are oval to sub-oval in shape, leucocratic to mesocratic in nature and deformed along the margins. Interestingly, both the granites are thorite bearing and are outcropped along NE-SW trend and exhibit discordant relationship with the host Mesoproterozoic Rapur granite exposed SE of Ramreddipalem.

Petrographically, the GR granite consists essentially of K-feldspar, quartz and plagioclase with minor biotite. Zircon, epidote, apatite, titanite, monazite and opaques, constitute the accessory minerals. Textural studies indicate the presence of quartz-alkali feldspar intergrowths and micrographic textures. Mineral chemistry by EPMA studies helped in concluding the presence of uraninite and thorite. Major oxide analysis, indicate an average high SiO_2 (70.83 wt %) and Na_2O+K_2O content (8.42 wt %) and low CaO (1.46 wt %) and MgO (0.74 wt %). Relative enrichment of Ba (430-1499 ppm), Zr (118-541 ppm) Y (25-150 ppm) and HREE is observed as compare to Sr content (19 ppm to 119 ppm). LREEs are relatively enriched when compared to HREE and has negative Eu anomaly. In Zr+Nb+Ce+Y vs major oxide and 10000 Al*Ga/Al vs trace element plots, the samples fall in A-type field, while in the trace element tectonic discrimination diagram, these granite exhibit within-plate granite (WPG) characters. In contrast to this, the granite plots in A_2-type field of Y-Nb-Ce diagram, which is an indication that it is derived by differentiation of a continental tholeiite, with variable degrees of crustal interaction, or by direct melting of a crustal source.

Keywords: Thorite bearing granite, Nellore Schist Belt, Eastern Dharwar Craton, Anorogenic magmatism

INTRODUCTION

A-type igneous suites constitute a major component of the continental crust, with roughly 30% basic rocks, 18% intermediate rocks and 6% granites and syenites. In Precambrian continental terranes, most of A-type igneous rocks are referred to as anorogenic or cratonic (Lameyre et al., 1974) and are emplaced into non-orogenic settings – both within plate and along plate margins. These granites presumably represent the most voluminous intraplate silicic magmatism and are often aligned in a linear or semi-linear manner across Precambrian cratons and are known to occur in all continents (e.g: Anderson, 1983; Anderson and Morrison, 1992; Rämö and Haapala, 1995; Subba Rao et al., 1998; Rajesh, 2000).

Anorogenic granites are characterised by their distinct mineralogy, whole rock and trace element composition, form significant constituent of the Earth's continental crust and are emplaced in extension tectonic setting (e.g: Loiselle and Wones, 1979; Collins et al., 1982; Whalen

et al., 1987; Eby, 1990, 1992). The petrogenesis of the Proterozoic A-type granites play an important role during evolution of different terranes, which include: (1) crystal–liquid fractionation, (2) incomplete separation of melts and source materials, (3) reaction between melts and surrounding wall rocks, and (4) mixing or mingling of coexisting magmas. Of these processes, crystal–liquid fractionation is significant in A-type granite magmas (Clemens et al., 1986; Tatsumi et al., 1986; Collins et al., 1992; Stolz et al., 1996; Dall'Agnol et al., 1999; Dostal et al., 2004; Dostal and Chatterjee, 2000). Based on difference in petrogenetic pathways Eby (2004), suggested further division of A-type granitoids into A_1 and A_2-types. The group with lower Y/Nb ratios (group A_1, with Y/Nb<1.2) includes felsic rocks from oceanic islands and continental rifts; these granitoids were suggested to form an oceanic island basalt source in an intraplate or rift setting. Whereas, the group with higher Y/Nb (group A_2, with Y/Nb>1.2) was proposed to form by a number of different mechanisms: from an island arc or continental margin basalt source, or from crustal sources such as tonalite or granodiorite, or even by partial melting of crust from which a melt was previously extracted (Eby, 1992).

The Paleoproterozoic to Mesoproterozoic period has witnessed extensive anorogenic granite magmatism worldwide that resulted in events of significant crustal growth (e.g. Haapala, and Rämö, 1999). Southern India too witnessed extensive Proterozoic magmatism (e.g. French et al. 2008; Divakara Rao et al. 1999) while a significant event of Proterozoic granite magmatism was demarcated to the east of Cuddapah basin along the terrain boundary shear zone (Chetty and Murthy, 1994; Sesha Sai, 2013). Chetty and Murthy, (1994) further observed that the area between the Proterozoic Cuddapah basin to the west and the Eastern Ghats Mobile Belt (EGMB) to the east, defines a cryptic suture. Mesoproterozoic rift related magmatism resulted in the emplacement of alkaline complexes and mafic dykes in the EGMB and adjoining area in SE India (e.g. Ratnakar and Leelanandam, 1989; Ratnakar and Vijaya Kumar, 1995; Ratnakar, et al., 2008; Dobmeier and Raith, 2003; Upadhyay et al., 2006; Vijaya Kumar et al. 2011).

The study is aimed to present the succinct details of the field, petrographic and geochemical characters of a NE-SW trending sub oval granite pluton around Gilkapadu – Ramreddipalem (GR), situated to the north of Rapur in the southern part of NSB, Eastern Dharwar Craton (EDC), India. This newly demarcated granite pluton is disposed to the north of the well-known Kandra Ophiolite Complex (Leelanandam, 1990; Sesha Sai, 2009; Vijay Kumar et al, 2010) and is located close to the vicinity of the eastern margin of southern part of the Nallamalai Fold Belt (NFB).

GEOLOGICAL SETTINGS

The present study area is situated near the contact between the Nellore schist belt and Cuddapah basin/Nallamalai Fold Belt (Figure 1). The Neoarchean NSB of SE India mainly consists of metamorphosed volcano-sedimentary rocks that are intruded by syenites, alkali granites, granites and mafic rocks of Proterozoic age (e.g. Babu, 1998, Dobmeier and Raith, 2003; 2008; Dobmeier et al., 2006; Ghosh et al., 1994; Gupta et al., 1984; Ravikant, 2010; Vijaya Kumar et al., 2010; Sesha Sai, 2013). The belt is accreted along the southeastern margin of Eastern Dharwar craton along the Vellikonda thrust front (e.g. Venkatakrishnan and Dotiwala, 1987). The Rapur proto orbicular granite (Srinivasan and Roop Kumar, 1995), that are well exposed around Raviguntapalle area, is located to the SE of the present study area.

Granite gneiss that forms part of the unclassified Archean crystalline Complex are also exposed to the east and south east of Rapur, close to the eastern margin of Cuddapah basin (Meshram and Dharme, 2014). The thorite bearing GR granite bodies also falls within the Proterozoic granite magmatism zone, demarcated along the western margin of the NSB (Mitra et al., 2013; Sesha Sai, 2013). The Gilkapadu biotite granite is massive and occurs as semi oval outcrop occupying an area of about 5 sq km, while the Ramreddipalem biotite granite occur as circular body covering an area of about 3.5 sq km. The both granitic bodies are located along NE trending axial plane of regional fold (Figure 1). Field studies indicate that both these granites are massive; however, along their margins they are deformed.

Analytical Technique

Petrographic study and photomicrography were carried out using LEICA DM RX research microscope fitted with camera, at the Petrology lab, Geological Survey of India, Hyderabad. Whole rock major and trace element analyses were carried out at the Chemical laboratory, Geological Survey of India, Hyderabad. The X-ray fluorescence spectrometry was used to analyze major oxide, and ICP-MS (Perkin Elmer Sciex ELAN 600) was used to determine trace and rare-earth element concentration. The precision is <5% for all analyzed elements when reported at 100X detection limit. Several standards were run along with the studied samples to check accuracy and precision Whole rock chemical data is presented in Table 2.

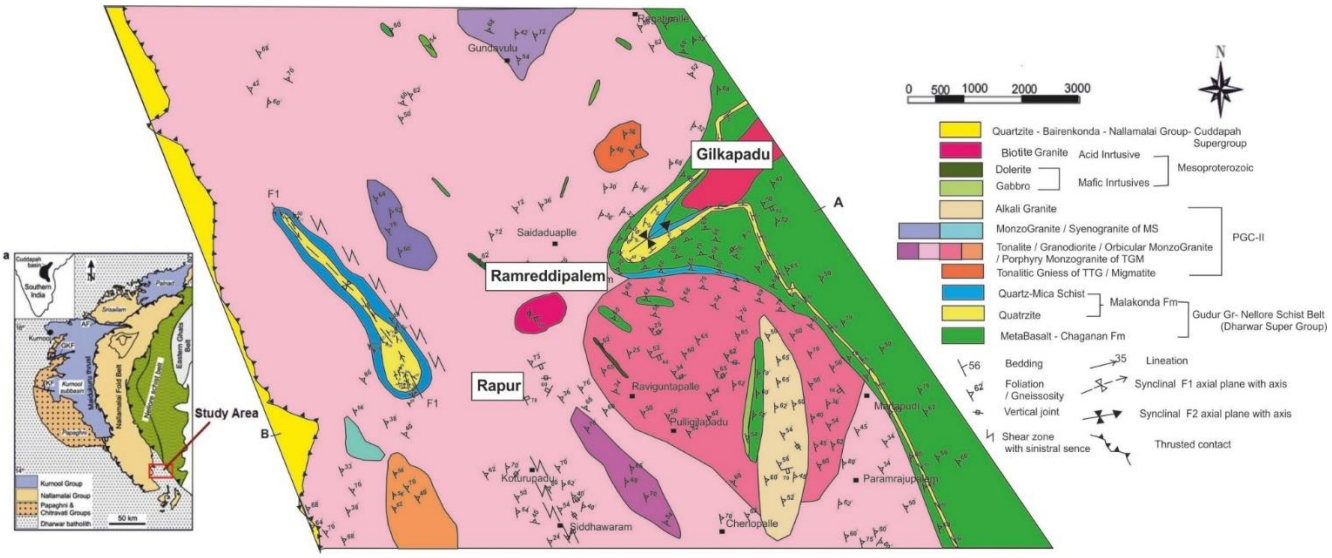

Figure 1. Geological map around Gilkapadu and Ramreddipalem (GR) area, showing different variants of Granitoids in the area. Inset map -Regional map of Cuddapah basin and Nellore schist belt (Meshram and Dharme, 2014).

PETROGRAPHY

Petrographic studies and modal compositions of representative samples (n-24) indicate that the Gilkapadu and Ramreddipalem granites fall in the granite field. In IUGS-QAP plot (Streckeisen, 1967), they fall close to the boundary of syenogranite-monzogranite field indicating their MS suite character (Figure 2). Thin section studies indicate that these biotite bearing granites show hypidiomorphic texture and are essentially composed of alkali feldspar and quartz, with sub ordinate plagioclase and interstitial biotite (Figure 3A and B). Zircon, allanite, titanite, monazite and opaques are the accessory phases (Figure 3C and D).

Modal analysis of 24 nos. of representatives thin sections indicate that these granites predominantly consist of microcline microperthite, indicating exsolution, while plagioclase exhibiting twining is mostly albite with minor oligoclase. Plagioclases are partly sausaritised at places, and shows development of epidote and zoisite. Quartz is relatively fine grained, anhedral and shows undulose extinction. At places quartz-alkali feldspar intergrowths are noticed in the form of micrographic texture (Figure 3B). Biotite shows flaky habit, brown pleochroism and occurs interstitial to quartz and feldspar grains (Figure 3A). The accessory phases mainly consist of zircon, uraninite, thorite, epidote, zoisite, apatite, titanite and monazite (Figure 3).

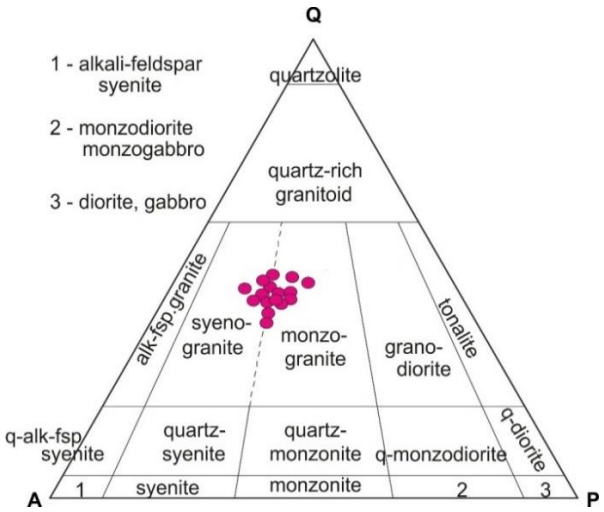

Figure 2. Position of the Gilkapadu and Ramreddipalem granites (n=24) in IUGS-QAP diagram

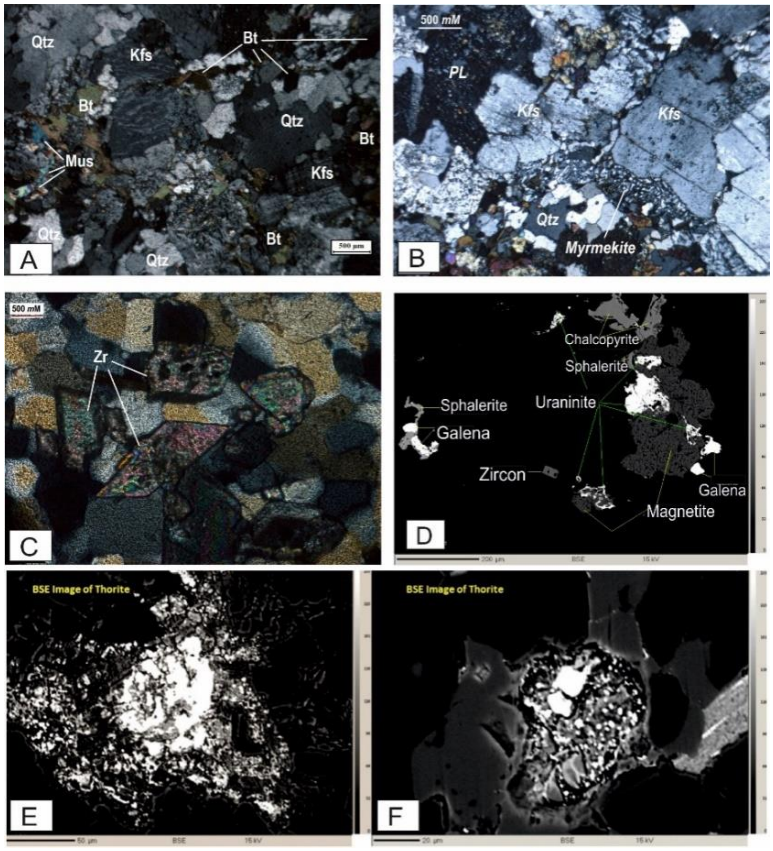

Figure 3. (A) Photomicrograph of Gilkapadu and Ramreddipalem biotite granite showing its two mica character, microcline shows tartan twin while at places it is perthitic in nature. (B) Photomicrograph showing development of myrmekite along the margin of microcline exhibiting characteristic cross hatched twinning in Biotite granite. (C) Photomicrograph of showing euhedral zircon in biotite granite of Gilkapadu and Ramreddipalem. (D) BSE image of Gilkapadu and Ramreddipalem biotite granite shows association of sphalerite, galena, pyrite, uraninite and magnetite. (E and F) BSE image of Gilkapadu and Ramreddipalem biotite granite shows presence of thorite.

MINERAL CHEMISTRY

Representative electron microprobe analyses of fresh feldspars, biotite, zircon, uraninite and thorite from granites are given in Table 1.

Biotite

Biotite is pleochroic, shows light brown to dark brown color and flaky habit. The biotite (n=3) (Gn/45, Table 1) in A-type granite shows average SiO_2 - 34.11 wt%, Al_2O_3- 14.97 wt%, FeO- 30.28 wt%, MgO- 4.56 wt%,K_2O- 8.73 wt% and TiO_2- 1.73 wt% and low contents of MnO, CaO and P_2O_5. Biotite is mainly annite in composition, which is common in A-type granites.

Feldspars

Potash feldspars are very common, shows tartan twining and fresh in nature. The potassic feldspar ($Or_{97.97}$) (n=8) (Gn/45, Table 1) shows SiO_2 - 63.37 wt%, Al_2O_3- 17.91 wt%, K_2O- 15.96 wt% with very minor amount of CaO-0.001 wt% and Na_2O-0.22 wt%. It also contain negligible amount of FeO, MgO, MnO, and TiO_2.

Plagioclase shows polysynthetic twining and fresh in nature. The plagioclase ($Ab_{98.25}$) (n=2) (Gn/45, Table 1) shows SiO_2 - 69.08 wt%, Al_2O_3- 19.57 wt%, Na_2O - 11.01 wt% and with low amount of CaO-0.31 wt%. It also contain negligible amount of K_2O, FeO, MgO, MnO, and TiO_2.

Accessory minerals: Zircon, Uraninite and Thorite

Accessory, Zircon (n=7) (Gn/45, Table 1) showing averages of ZrO_2 -65.91 wt% and SiO_2-31.46 wt%. Uraninite (n=1) (Gn/45, Table 1) shows UO_2-76.92 wt%, SiO_2-7.84 wt%, CaO-2.53%, Y_2O_3-2.66 wt%, La_2O_3-0.39 wt%, Ce_2O_3-0.99 wt%, Pr_2O_3-0.13 wt%, Nd_2O_3-1.4 wt%, SmO-0.18 wt%, PbO-0.21 wt%, TaO_2-4.04 wt%, and ZrO_2-1.45 wt%.

Similarly, thorite (n=4) (Gn/45, Table 1) shows average ThO_2-54.01 wt%, UO_2-6.2 wt%, SiO_2-18.89 wt%, Y_2O_3-5.86 wt%, CaO -1.45 wt%, La_2O_3-0.21 wt%, Ce_2O_3-3.1 wt%, Pr_2O_3-0.22 wt%, Nd_2O_3-1.9 wt%, SmO-0.47 wt%, PbO-0.08 wt%, ZrO_2-2.58 wt%, Yb_2O_3-0.22 wt%, and Ag_2O-0.25 wt%.

GEOCHEMISTRY

Geochemical studies indicate that GR biotite granites exhibit “calc alkaline trend” (Figure 4A) and characterized by high SiO_2 - 70.83 wt % and (Na_2O + K_2O)- 8.42 wt % and low CaO - 1.46 wt % and MgO - 0.74 wt % (average values, Table 2). Trace element analyses indicate enriched Ba (430-1499 ppm), Zr (118-541 ppm) Y (25-150 ppm) and high REE, while Sr content (19 ppm to 119 ppm) is relatively low, these are revealing characteristics of A-type granites (Whalen, 1987; Eby, 1990; 1992) (Table 2). REE geochemistry indicates relative enrichment of LREE and negative Eu anomaly. Enrichment of incompatible elements, particularly, high field strength elements (HFSE) and light rare earth elements (LREE) is a characteristic feature of the NSB Proterozoic granites (Sesha Sai, 2013). Most of the samples exhibit metaluminous to peraluminous nature (Figure 4B).

Table 1. EPMA analysis of mineral phases from Gilkapadu and Ramreddipalem granite.

Oxide	**Albite**	**K-feldspar**	**Oxide**	**Biotite**	**Oxide**	**Uraninite**	**Thorite**		**Zircon**	**Zircon**
SiO_2	69.084	63.372	SiO_2	34.116	SiO_2	7.84	18.894	23.625	31.462	31.552
TiO_2	0.008	0.005	TiO_2	1.731	P_2O_5	0.043	0.393	0.218	0.403	0.419
Al_2O_3	19.575	17.91	Al_2O_3	14.975	CaO	2.531	1.459	1.602	0.002	0.03
FeO^T	0.011	0.014	Cr_2O_3	0.037	Y_2O_3	2.667	5.869	6.953	0.08	0.077
MnO	0.001	0.001	FeO^T	30.281	La_2O_3	0.392	0.215	0.108	0.057	0.019
MgO	0.004	0.002	MnO	0.383	Ce_2O_3	0.99	3.109	2.86	0.019	0.039
CaO	0.313	0.001	MgO	4.569	Pr_2O_3	0.134	0.223	0.162	0.022	0.029
Na_2O	11.011	0.228	CaO	0.027	Nd_2O_3	1.403	1.981	1.174	0.066	0.075
K_2O	0.036	15.968	Na_2O	0.038	SmO	0.186	0.478	0.757	0.109	0.117
Total	100.08	97.42	K_2O	8.736	PbO	0.214	0.086	0.307	0.02	0.011
Fe_2O_3	0.00	0.00	NiO	0	UO_2	76.928	8.899	4.972	0.054	0.006
FeO	0.01	0.01	**Total**	**94.89**	ThO_2	4.049	58.018	54.746	0.044	0.032
Total	100.08	97.42	Fe_2O_3	0	ZrO_2	1.452	2.585	6.08	65.915	66.067
Cations:	8(O)	8(O)	FeO	30.28	Yb_2O_3	0	0.222	0.254	0	0
Si	3.0055	3.0043	Total	94.89	Ag_2O	0	0.253	0.271	0	0
Ti	0.0003	0.0001	Cations:	22(O)	**Total**	96.162	96.815	97.136	98.173	98.396
Al	1.0038	1.0008	Si	5.541						
Fe^{+3}	0	0	Ti	0.2114						
Fe^{+2}	0.0004	0.0006	Al	2.8668						
MN	0.0001	0	Cr	0.0048						
Mg	0.0003	0.0001	Fe^{+3}	0						
Ca	0.0146	-0.001	Fe^{+2}	4.1131						
Na	0.9289	0.021	MN	0.0527						
K	0.002	0.9658	Mg	1.1062						
Total	4.957	4.9897	Ca	0.0047						
Orthoclase	0.21	**97.97**	Na	0.012						
Albite	**98.25**	2.13	K	1.8102						
Anorthite	1.54	0.00	Ni	0						

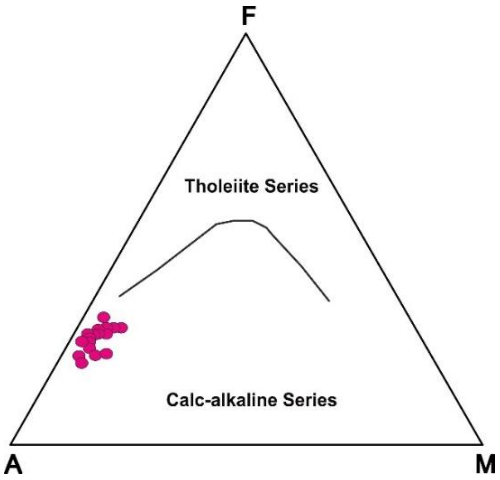

Figure 4(A). Plot showing the calc alkaline character of the GR biotite granites (Irvine and Baragar, 1971).

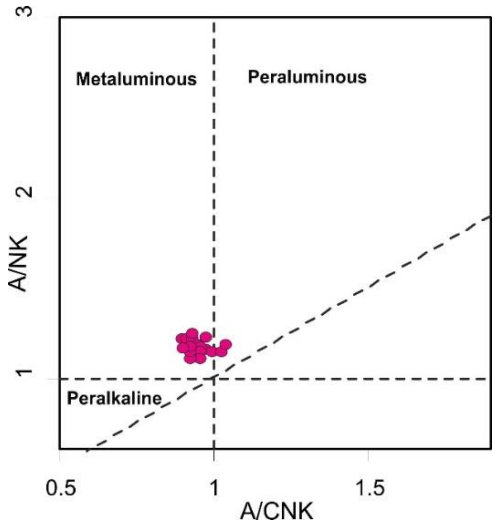

Figure 4(B). $Al_2O_3/(CaO+Na_2O+K_2O)$ vs $Al_2O_3/(Na_2O+K_2O)$ relationship of GR biotite granites suggest their metaluminous to peraluminous nature (Maniar and Piccoli, 1989).

Presence of high ($Na_2O+ K_2O/CaO$) ratio and high FeO^t content in typical metaluminous to mild peraluminous granites and enriched Ba, Zr, Y, Rb with high REE content and low Sr content indicate their anorogenic nature (Whalen, 1987) (Table 2 and 3). Further, in Zr+Nb+Ce+Y vs major oxide (Figure 6A-B) and 10000 Al*Ga/Al vs trace element plots (Figure 6C-D), the samples from this granite fall in A-type field, while in the Y vs Nb and Y+Nb vs Rb trace element tectonic discrimination diagrams (Pearce et al., 1984) the granite exhibit within plate granite (WPG) characters (Figure 6A and B). In Y-Nb-Ce diagram (Figure 6 C) the GR granites plot in A_2-type field (Eby, 1992). As suggested by Eby, (1992) this A_2-type may be derived by differentiation of a continental tholeiite, with variable degrees of crustal interaction, or by direct melting of a crustal source. In primitive-mantle normalized spidergrams, these granites exhibit enrichment of incompatible trace elements in the form of K, Ba and Rb; LILE and Th, U Zr, Nb, REE, HFSE. However, it is noticed that there is relative depletion of Sr, P, Tb and Eu. Chondrite normalized REE plots for the GR biotite

granites show enrichment of Light rare earth elements (LREE) with conspicuous negative europium anomaly (Figure 7), characteristic of anorogenic granites.

The heavy rare earth element (HREE) patterns are more or less flat. The ∑ REE contents vary from 294.62 ppm to 485.15 ppm and the Eu / Eu* ratio varies from 0.39 to 0.57 (Table 3). The high SiO_2 and Na_2O + K_2O content along with high incompatible element contents indicate an enriched lower crustal source that the GR biotite granites. The major- and trace-element compositions of the GR biotite granites are furnished in Table 2 and 3 for detail correlation.

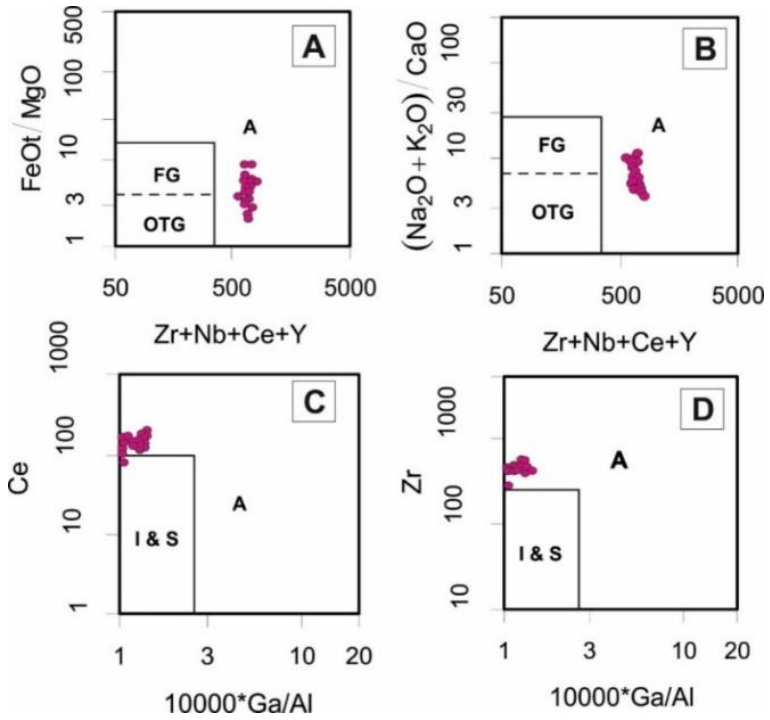

Figure 5. Plots showing A-type nature of Gilkapadu and Ramreddipalem biotite granite, (A) Zr+Nb+Ce+Y vs. FeOt/MgO, (B) Zr+Nb+Ce+Y vs. $(Na_2O+K_2O)/CaO$, (C) 10000*Ga/Al vs. Ce, (D) 10000*Ga/Al vs. Zr (Whalen et. al., 1987).

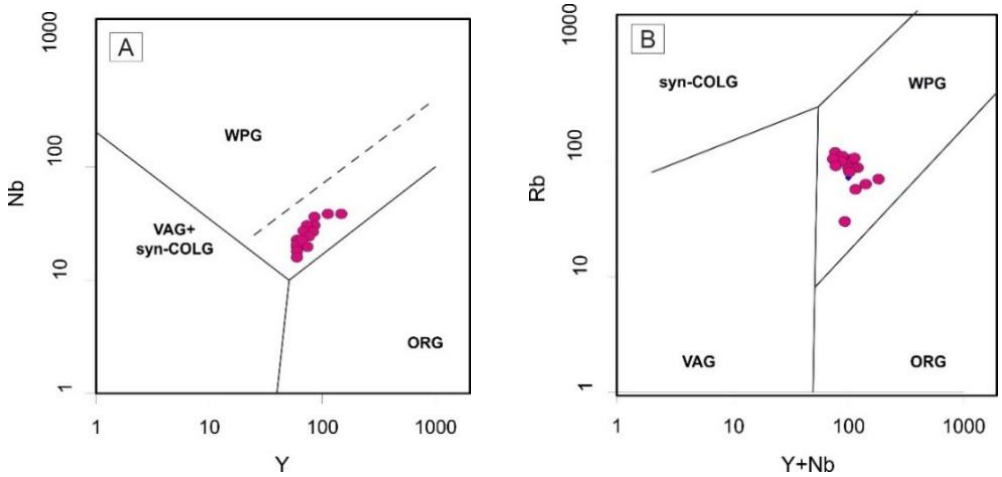

Figure 6 (A) (Nb-Y) and **(B)** (Y+Nb)-Rb plots showing the within Plate Granite (WPG) nature of the GR granites, north of Rapur, SE India (Pearce et al., 1984)

Table 2. Major oxide and trace element analyses of the Gilkapadu and Ramreddipalem granite.

Sample No	GN/37	GN/41	GN/42	GN/43	GN/45	GN/53	GN/54	GN/55	GN/56	GN/57	GN/58	GN/59	GN/61	GN/62	GN/63	GN/47
SiO2	69.99	70.48	70.61	70	70.94	71.2	70.48	72.57	70.29	70.83	70.47	69.5	69.5	70.66	71.06	70.68
Al2O3	12.31	13.32	13.64	13.85	13.19	12.05	13.32	12.33	13.66	13.73	13.71	13.23	13.83	13.09	13.19	14.11
Fe2O3	3.27	3.85	3.26	3.49	3.62	4.6	3.96	3.65	3.19	2.89	3.72	5.38	3.63	3.13	3.78	2.73
MNO	0.07	0.04	0.04	0.05	0.05	0.05	0.05	0.04	0.04	0.04	0.05	0.06	0.05	0.05	0.05	0.05
MgO	0.93	0.84	0.63	0.36	0.37	1.96	0.74	0.65	1.23	0.92	0.56	1.47	0.52	0.51	0.57	0.4
CaO	3.58	1.15	1.36	1.55	1.58	0.67	1.44	1.29	0.94	1.9	1.68	0.8	1.99	1.94	1.56	1.89
Na2O	5.24	4.2	4.14	4.01	3.75	3.95	3.53	3.74	4.37	4.47	4.01	3.63	4.17	3.7	4.04	4.05
K2O	1.35	4.34	4.61	4.95	4.9	3.71	4.75	4.52	4.42	3.96	4.77	4.32	4.6	4.35	4.18	4.62
TiO2	0.39	0.39	0.4	0.38	0.39	0.36	0.38	0.37	0.43	0.47	0.42	0.41	0.48	0.46	0.42	0.32
P2O5	0.07	0.08	0.08	0.08	0.08	0.07	0.08	0.07	0.08	0.1	0.09	0.08	0.13	0.09	0.08	0.12
LOI	1.98	0.47	0.48	0.45	0.64	0.48	0.58	0.42	0.57	0.43	-0.11	0.57	0.36	1.14	0.47	0.57
Total	99.18	99.16	99.25	99.17	99.5	99.1	99.31	99.64	99.22	99.74	99.37	99.44	99.25	99.12	99.39	99.54
Na2O+ K2O	6.59	8.54	8.75	8.96	8.65	7.66	8.28	8.26	8.79	8.43	8.78	7.95	8.77	8.05	8.22	
Ba	463.0	1056	1115	1026	1039	749.7	985.1	974.3	980	1499	1095	906	1009	1063	1247	815
Ga	8.6	9.6	8.7	7.6	9.5	5.9	10.0	8.4	9.3	8.2	9.0	7.3	5.5	8.9	7.1	7.8
Nb	27.0	27.4	27.8	26.2	25.9	19.9	24.4	25.4	29.7	34.2	26.5	21.7	17.5	38.0	29.0	15.9
Rb	29.5	83.4	73.7	108.3	108.7	107.9	102.8	106.0	89.8	57.3	89.9	122.0	96.1	64.9	86.5	103.1
Sr	119.8	56.8	65.9	71.0	84.8	34.2	70.5	70.0	52.2	87.3	75.7	42.2	83.0	97.4	71.6	92.2
Th	18.7	27.5	28.1	29.7	25.5	22.8	25.9	31.9	25.1	30.0	29.4	26.1	28.7	29.5	27.8	21.8
Y	69.5	76.3	74.4	79.2	79.1	70.0	74.9	71.9	81.2	84.2	80.5	57.8	58.7	109.3	71.6	57.9
Zr	387.5	447.1	433.2	436.0	448.0	394.6	407.4	465.5	452.2	465.3	478.9	438.3	275.2	519.7	420.5	281.1
Be	3.88	4.38	3.56	5.40	4.02	4.05	4.02	4.20	3.48	4.25	4.07	4.42	3.17	5.06	5.74	3.28
Ge	1.52	1.28	1.29	1.37	1.39	1.24	1.39	1.31	1.05	1.25	1.28	1.06	1.47	1.33	1.45	1.22
Cs	<0.2	1.74	1.06	0.67	1.37	0.61	1.41	1.85	0.99	1.08	1.21	0.88	1.46	1.42	1.40	1.69
Hf	17.83	17.74	16.35	15.73	17.20	19.81	17.49	19.26	15.89	21.21	19.58	18.13	23.45	18.04	20.42	11.44
Ta	2.51	2.35	2.33	2.24	2.39	2.27	2.48	2.80	2.12	2.64	2.66	2.48	3.28	2.82	2.76	1.70
10000 *Ga/Al	2.48	2.45	2.15	1.86	2.38	1.69	2.54	2.18	2.35	2.08	2.28	1.98	1.40	2.22	1.80	1.86

Table 3. Rare Earth Element analyses of the Gilkapadu and Ramreddipalem granite.

Sample No	GN/37	GN/41	GN/42	GN/43	GN/45	GN/53	GN/54	GN/55	GN/56	GN/57	GN/58	GN/59	GN/61	GN/62	GN/63	GN/47
La	67.63	65.30	69.12	51.08	88.67	120.76	98.83	76.97	59.28	89.60	63.23	73.60	77.03	74.52	79.69	60.97
Ce	148.30	130.56	140.34	107.93	168.37	226.22	194.09	148.79	119.57	172.52	134.06	146.19	191.77	147.62	161.63	116.78
Pr	15.97	15.43	16.65	14.16	20.33	26.65	22.15	18.25	14.70	20.30	16.89	17.51	20.74	17.12	19.99	13.50
Nd	59.42	59.36	62.67	58.03	76.09	98.94	80.67	68.15	56.73	75.45	67.04	66.41	81.76	64.62	76.49	49.78
Eu	1.93	1.99	2.06	1.98	2.17	2.68	2.19	2.30	1.80	2.37	2.30	2.11	2.66	1.90	2.29	2.00
Sm	12.91	14.16	14.19	14.83	16.68	21.19	17.11	15.79	13.61	16.67	16.16	14.72	20.74	15.00	18.10	11.11
Tb	2.27	2.53	2.39	2.65	2.85	3.22	2.87	2.82	2.37	2.80	2.91	2.51	3.88	2.66	3.25	1.90
Gd	12.88	13.95	13.55	14.73	16.25	19.43	16.37	15.82	13.27	15.92	15.81	14.25	21.05	14.58	18.08	10.48
Dy	13.85	15.47	14.60	16.21	17.02	18.76	17.45	17.56	14.63	17.18	18.09	15.04	24.93	16.44	19.85	11.11
Ho	3.01	3.39	3.13	3.48	3.72	3.89	3.78	3.86	3.20	3.75	3.98	3.23	5.38	3.57	4.34	2.35
Er	8.48	9.47	8.67	9.60	10.27	10.45	10.48	10.76	8.80	10.61	11.17	8.94	15.03	10.01	12.39	6.40
Tm	1.46	1.61	1.48	1.62	1.72	1.71	1.79	1.87	1.53	1.82	1.91	1.50	2.53	1.75	2.20	1.05
Yb	9.09	9.95	9.13	9.81	10.46	10.34	10.85	11.56	9.10	11.46	11.69	9.07	15.36	10.65	13.76	6.28
Lu	1.37	1.50	1.36	1.46	1.56	1.52	1.62	1.74	1.37	1.71	1.78	1.34	2.29	1.61	2.10	0.92
LREE	306.16	286.80	305.03	248.01	372.32	496.44	415.03	330.26	265.71	376.90	299.69	320.54	394.70	320.78	358.18	254.14
HREE	52.40	57.87	54.30	59.57	63.86	69.31	65.20	65.99	54.27	65.26	67.34	55.88	90.45	61.26	75.96	40.48
∑REE	358.56	344.66	359.33	307.58	436.18	565.75	480.23	396.25	319.97	442.16	367.03	376.41	485.15	382.04	434.15	294.62
LREE/HRRE	5.82	4.95	5.61	4.16	5.83	7.16	6.36	5	4.73	5.77	4.45	5.73	4.36	5.23	4.71	6.27
Eu/Eu*	0.46	0.44	0.46	0.41	0.41	0.41	0.40	0.45	0.41	0.45	0.44	0.45	0.39	0.39	0.39	0.57
La^N/Yb^N	4.96	4.38	5.05	3.47	5.65	7.79	6.07	4.44	4.34	5.21	3.61	5.41	3.34	4.66	3.86	6.47
La^N/Sm^N	3.22	2.84	3.00	2.12	3.27	3.51	3.55	3.00	2.68	3.31	2.41	3.08	2.28	3.06	2.71	3.38
Eu^N/Yb^N	0.61	0.57	0.64	0.58	0.59	0.74	0.58	0.57	0.57	0.59	0.56	0.66	0.49	0.51	0.48	0.91
Ce^N/Yb^N	4.12	3.34	3.91	2.80	4.09	5.56	4.55	3.27	3.34	3.83	2.92	4.10	3.18	3.53	2.99	4.73
Ce^N/Sm^N	2.70	2.16	2.32	1.71	2.37	2.51	2.66	2.21	2.06	2.43	1.95	2.33	2.17	2.31	2.10	2.47

DISCUSSION

A-type granites are interpreted to be derived from magmas that have an exclusively igneous source (Whalen et al., 1987), by partial melting of granodiorite or tonalite, or extreme fractionation of mafic magma (Loiselle and Wones, 1979). Most calc-alkalic ferroan granitoids have high silica contents (>70% SiO2) and are generally characterized by lower Al_2O_3 contents (12 to 13.5 wt %) when compared with typical I-type magnesian calc-alkalic granitoid series with Al_2O_3 of >14 wt %. Examples include granites from Carajas, Brazil (Dall'Agnol and Oliveira, 2007; Oliveira et al., 2009), which were interpreted to form by melting of anhydrous continental crust.

Experimental work by Shaw (1970) and Papousta et al. (2014) on whole-rock composition of A-type granite and intermediate rock applied batch partial melting geochemical models for specific highly incompatible trace elements (such as Nb, Rb, Th, and U), suggested that biotite granites could have been formed by similar degrees of partial melting, ranging between 20% and 40% of extracted melt. Similarly, the GR biotite granite have >1.2 Y/Nb and >3 Yb/Ta ratio, which suggest the significant role of crustal contamination or upper-crustal mixing or assimilation.

Eby (1990, 1992) further subdivided A-type granitoids into two groups on the basis of trace element abundances, particularly the Y/Nb ratio. The biotite bearing GR granites are classified as A_2-type granites in Y-Nb-Ce diagrams (Figure 6C) (Eby, 1992), suggesting that they are probably not fractionates of the mafic melts. A_2 granitoids include a greater diversity of compositions, from metaluminous to peraluminous or peralkaline, and from alkalic to calc-alkalic. For examples, the potassic series of Pikes Peak granites and some Gardar granites belong to group A_2 (Marks et al., 2003; Smith et al., 1999).

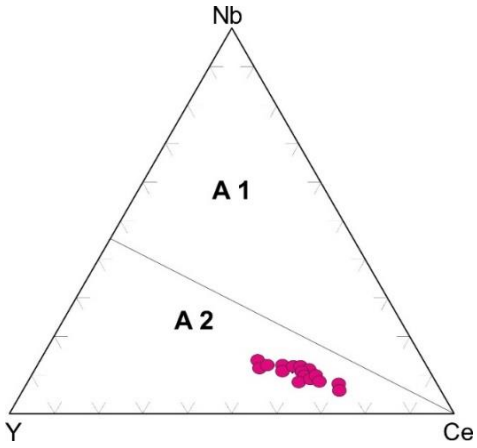

Figure 6(C). Y-Nb-Ce diagram (Eby, 1992) showing the A_2-type nature of the Gilakapadu and Ramreddipalem granites, north of Rapur, SE India

The A_2-type (often referred to as post-collisional or post-orogenic), represented all A-type granitoids not derived by fractionation of an OIB-like magma. These granitoids were generally emplaced shortly after an orogenic period and may have originated by melting of mantle material with crustal interaction or solely by the melting of crustal material. Y/Nb and Yb/Ta ratios are relatively useful to understand the source characteristic of A-type granites. A-type suites with Y /Nb < 1.2 are derived from sources chemically similar to those of oceanic Island basalts, while suites with Y /Nb > 1.2 are derived from sources chemically similar to island arc or continental margin basalts.

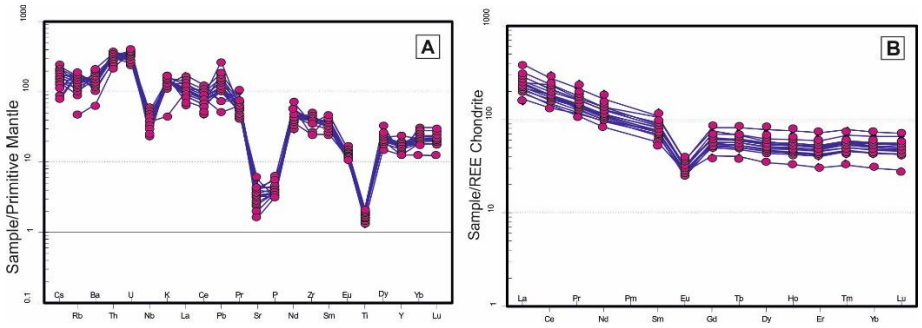

Figure 7. Primitive Mantle (Figure A) and Chondrite normalized (Figure 2) REE plots for the GR biotite granite north of Rapur, SE India.

The biotite bearing GR granite of study area is geochemically quite distinct from the other granitic variants of the study area (Figure 1). It shows strong depletion in Ba, Nb, Sr, P and Ti, and enrichment in Ga, which are indicative of strong fractionation. These granites, however, show low amounts of Zn (< 90 ppm; Table 1) (Figure 7). Zn is generally more concentrated in mafic melts, and many A-type granites interpreted as partial melts of intermediate feldspathic rocks, having lower amounts of Zn (Jung et al., 1998; Wenner and Lloyd, 2006). These observations are comparable to the results of present study. Annite-rich biotite composition and major oxide analyses i.e., high SiO_2, Na_2O+K_2O, Fe/Mg, Zr, Nb, Ga, Sn, Y and REE (except Eu) with low CaO and Sr contents, broadly indicate anorogenic nature of these granites. Textural evidence, and geochemical data suggest that biotite granite in the area formed from relative high temperature, water-undersaturated (Clemens et al. 1986), completely molten (i.e., restite free) magma. It displays petrological similarities to lower crustal rocks considered as A-type sources elsewhere, for example some of the Dharwar Craton biotite granites formed by anatexis of TTG-like sources (either old Peninsular gneisses or the TTG) (Subba Rao et al., 1992a,b). The overall geochemical characteristics of the GR biotite granites broadly indicate their anorogenic nature.

CONCLUSIONS

(i) Detailed field, petrological and geochemical studies brought to light on the new occurrence of A-type granite at Gilkapadu and Ramreddipalem areas, north of Rapur, along the contact between NFB and NSB (Eastern Dharwar Craton, India).

(ii) Field studies indicate that this GR granite is leucocratic to mesocratic and deformed along the margins. It is a new and younger anorogenic granitic event, after the known orbicular Rapur granite in the area.

(iii) Petrographic studies establish that they mineralogically form part of syenogranite-monzogranite field, indicating their MS suite nature. Mineral chemistry suggests that, K-feldspar is microcline (Or_{97}), plagioclase is albite (Ab_{98}) and biotite is annite (FeO^T – 29.14 to 30.28%; MgO - 4.20 to 4.56%) in composition. Textural studies indicate the presence of quartz-alkali feldspar micrographic intergrowth; a late stage magmatic texture.

(iv) EPMA studies established the presence of uraninite and thorite in the GR Granite.

(v) Their major and trace element characters shows high SiO_2 and $Na_2O + K_2O$ contents, low CaO and MgO contents along with enriched Ba, Zr, Y, Rb with high REE content and low Sr content indicate their anorogenic nature.

(vi) The crustal contamination or upper-crustal mixing or assimilation has played a significant role, as suggested by >1.2 Y/Nb and >3 Yb/Ta ratios.

(vii) The trace element ratios further suggest its A_2 nature, which are generally formed by partial melting of relatively anhydrous lower crustal rocks and are comparable with Pikes Peak granites, Colorado, USA and some Gardar granites, Gardar Province, Greenland that belongs to similar A_2 group granitic intrusion during Mesoproterozoic period.

(viii) Further in the trace element tectonic discrimination diagram, the Gilkapadu and Ramreddipalem granites exhibit within plate granite characters.

ACKNOWLEDGMENT

Shri. S. Balakrishnan, ADG (Retd.), GSI, Southern Region and Shri. M.S. Jairam, DDG, Andhra Pradesh, Hyderabad are thankfully acknowledged for valuable support. Dr. Santanu Bhattacharjee and Shri. S.T. Narhari is thanked for EPMA analysis. Officers of XRF and ICP-MS Lab, Chemical Division, GSI, Southern Region, Hyderabad are thankfully acknowledged for providing chemical analyses. The authors express his sincere thanks to Shri O P Pandey, Editor IGU and J. Ratnakar and Dr. Vikash Tripathy, reviewers for their suggestions and constructive comments during various stages.

Compliance with Ethical Standards

The authors declare that they have no conflict of interest and adhere to copyright norms.

REFERENCES

Anderson, J.L. 1983. Proterozoic anorogenic granite plutonism of North America. Geol. Soc. Am. Mem. 161, 133-154.

Anderson, J.L. and Morrison, J., 1992. The role of anorogenic granites in the Proterozoic Crustal development of North America. In: Condie, K.C. (Eds.), Proterozoic Crustal Evolution. Developments in Precambrian Geology, 10, 263–299.

Babu, V.R.R.M., 1998. The Nellore schist belt: an Archean greenstone belt, Andhra Pradesh, India. In: Rao, A.T., Divi, S.R., Yoshida, M. (Eds.), Precambrian Crustal Processes in East Coast Granulites—Greenstone regions of India and Antarctica within East Gondwana, Gondwan Research Group Memoir No. 4, 97–136.

Chetty, T.R.K. and Murthy, D.S.N., 1994 Collision tectonics in Eastern Ghats Mobile Belt: Mesoscopic to Satellite scale structural observations. TERRA NOVA, 6, 72-81.

Clemens, J.D., Holloway, J.R. and White, A.J.R., 1986. Origin of an A type granite: experimental constraints. American Mineralogist, 71, 317–324.

Collins, W.J., Beams, S.D., White, A.J.R. and Chappell, B.W., 1982. Nature and origin of A-type granites with particular reference to southeastern Australia. Contribution to Mineral. Petrol., 80, 189-200.

Collins, W.J., Beams, S.D., White, A.J.R., Chappell, B.W., 1992. Nature and origin of A-type granites with particular reference to southeastern Australia. Contributions to Mineralogy and Petrology, 80, 189–200.

Dall'Agnol, R., Scaillet, B. and Pichavant, M., 1999. An experimental studies of a lower Proterozoic A-type granite from the Eastern Amazonian Craton, Brazil. J. Petrol., 40, 1673–1698.

Dall'Agnol, R. and Oliveira, D.C., 2007. Oxidized, magnetite-series, rapakivi-type granites of Carajás, Brazil: implications for classification and petrogenesis of A-type granites. Lithos 93, 215–233.

Divakara Rao, V., Subba Rao, M.V. and Murthy, N.N., 1999. Granite forming events and their role in crust formation of India Shield. Revista Brasileira de Geociências, 29, 33-40.

Dobmeier, C.J. and Raith, M.M., 2003. Crustal architecture and evolution of the Eastern Ghats Belt and adjacent regions of India. In: Yoshida, M., Windley, B.F., Dasgupta, S. (Eds.), Proterozoic East Gondwana: Supercontinent Assembly and Breakup. Geol. Soc. London Spl. Publ. no. 206, 145–168.

Dobmeier, C., Lutke, S., Hammerschmidt, K. and Mezger, K., 2006. Emplacement and deformation of the Vinukonda metagranite (Eastern Ghats, India): Implications for the geological evolution of peninsular India and for Rodinia reconstructions. Precamrian Res., 146, 165-188.

Dostal, J. and Chatterjee, A.K., 2000. Contrasting behaviour of Nb/Ta and Zr/Hf ratios in a peraluminous grantic pluton Nova Scotia, Canada. Chemical Geology, 123, 67–88.

Dostal, J., Chatterjee, A.K. and Kontak, D.J., 2004. Chemical and isotopic (Pb,Sr) zonation in a peraluminous granite pluton:role of fluid fractionation. Contributions to Mineralogy and Petrology, 147, 58–73.

Eby, G.N., 1990. The A-type granitoids: a review of their occurrence and chemical characteristics and speculations on their petrogenesis. Lithos, 26, 115–134.

Eby, G.N., 1992. Chemical subdivision of A-type granitoids: petrogenetic and tectonic implications. Geology, 20, 641–644.

French, J.E., Heamen, L.M., Chacko, T. and Srivastava, R.K., 2008. 1891–1883 Ma Southern Bastar–Cuddapah mafic igneous events, India: a newly recognized large igneous province. Precambrian Res., 160, 308-322.

Ghosh, S., Das, J.N., Rao, A.K., Ray Barman, T., Kollapuri, V.K. and Sarkar, A., 1994. Fission-track and K–Ar dating of pegmatite and associated rocks of Nellore schist belt, Andhra Pradesh: evidence of middle- to late-Protrozoic events. Indian Minerals 48, 95–102.

Gupta, J.N., Pandey, B.K., Chabria, T., Banerjee, D.C. and Jayaram, K.M.V., 1984. Rb-Sr geochronological studies of the granites of Vinukonda and Kanigiri, Prakasam district, Andhra Pradesh, India. Precambrian Res., 26, 105-109.

Haapala, I. and Rämö, O.T., 1999. Rapakivi granites and related rocks: an introduction. Precambrian Research, 95, 1–7.

Irvine, T.N. and Baragar, W.R.A., 1971. Aguide to the chemical classification of the common volcalnic rocks. Canadian J. earth sci., 8, 523-548.

Jung, S., Mezger, K. and Hoernes, S., 1998. Petrology and geochemistry of syn- to post-collisional metaluminous A-type granites – a major and trace element and Nd–Sr–Pb– O-isotope study from the Proterozoic Damara Belt, Namibia; Lithos, 45, 147–175.

Lameyre, J., Rocci, G. and Didier, J., 1974. Granites orogéniques et granites cratoniques: réflexions sur un aspect fondamental de la géotectonique. Géologie des Domaines Cristallins, Centenaire de la Société Géologique de Belgique, Liège, 183–221.

Leelanandam, C., 1990. Kandra volcanics: possible ophiolite. Current Science 59, 785–788.

Loiselle, M.C. and Wones, D.R., 1979. Characteristics and origin of anorogenic granites. Geological Society of America, Abstracts 11, 468.

Maniar, P.D. and Piccoli, P.M., 1989. Tectonic discriminations of granitoids. Geol. Soc. Amer. Bull., 101, 635-643.

Marks, M., Vennemann, T., Siebel, W. and Markl, G., 2003. Quantification of magmatic and hydrothermal processes in a peralkaline syenite–alkali granite complex based on textures, phase equilibria, and stable and radiogenic isotopes. J. Petrol., 44, 1247–1280.

Meshram, T. and Dharme, R., 2014. Report on specialized thematic mapping of the granitoids in southern part of the Nellore Schist Belt, Nellore and Cuddapah dist, A.P, unpubl. report, F.S. 2012-14. GSI. Hyd.

Mitra, S.K., Meshram, T.M., and Dharme, R.G., 2013. Uraninite associated with Thorite and REE minerals in the younger granites of Rapur area, Nellore district, Andhra Pradesh, National Conference on Earth Sciences in India: Challenges and Emerging Trends (ESICET-2013), 7-9.

Oliveira, D.C., Dall'Agnol, R., Barros, C.E.M. and Oliveira, M.A., 2009. Geology, geochemistry and magmatic evolution of the Paleoproterozoic, anorogenic oxidized A-type Redenção granite of the Jamon Suite, eastern Amazonian Craton, Brazil. The Canadian Mineralogist 47, 1441–1468.

Papousta, A., and Pe-Piper, G., 2014 Geochemical variation of amphiboles in A-type granites as an indicator of complex magmatic systems, Wentworth pluton, Scotia, Canada; Chem. Geol., 384, 120–134.

Pearce, J.A., Hams, N.B.W. and Tindle, A.G., 1984. Trace element discrimination diagrams for the tectonic interpretation of granitic rocks. J. Petrol., 25, 956-983.

Rajesh, H.M., 2000. Characterization and origin of compositionally zoned aluminous A-type granite from South India. Geological Magazine 137, 291–318.

Rämö, O.T. and Haapala, I., 1995. One hundred years of rapakivi granites. Mineralogy and Petrology, 52, 129–185.

Ratnakar, J., Vijaya Kumar, K. And Rathna, K., 2008. Geochemical investigation of the alkaline mafic dykes in the environs of the Prakasam alkaline province, Eastern Ghats belt, India. In: Rajesh K. Srivastava, Ch. Sivaji, and N.V. Chalapathi Rao (Eds.), Indian dykes: Geochemistry, Geophysics and Geochronology. Narosa Publishing House, New Delhi, 291-308.

Ratnakar, J. and Vijaya Kumar, K., 1995. Petrogenesis of quartz-bearing syenite occurring within nepheline syenite of the Elchuru alkaline complex, Prakasam Province, Andhra Pradesh. J. Geol. Soc. Ind., 46(6), 611-618.

Ratnakar, J. and Leelanandam, C., 1989. Petrology of the alkaline plutons from the eastern and southern Peninsular India. In: C. Leelanandam (Ed.), Alkaline Rocks. Mem. Geol. Soc. India, 15, 145-176.

Ravikant, V., 2010. Palaeoproterozoic (1.9 Ga) extension and breakup along the eastern margin of the Eastern Dharwar Craton, SE India: new Sm–Nd isochron age constraints from anorogenic mafic magmatism in the Neoarchean Nellore greenstone belt. J. Asian Earth Sci., 37, 67–81.

Sesha Sai, V.V., 2009. Sheeted dykes in Kandra ophiolite complex, Nellore Schist Belt, Andhra Pradesh, vestiges of Precambrian oceanic crust. J. Geol. Soc. India, 74, 509–514.

Sesha Sai V.V., 2013. Proterozoic Granite Magmatism along the Terrane Boundary Tectonic Zone to the East of Cuddapah basin, Andhra Pradesh – Petrotectonic Implications for Precambrian Crustal Growth in Nellore Schist Belt of Eastern Dharwar Craton, Geol. Soc. India, Bangalore, 81, 167-182.

Shaw, H.R., 1970. Trace element fractionation during anatexis. Geochemica et Cosmochimica Acta, 34, 237-243.

Smith, D.R., Noblett, J., Wobus, R.A., Unruh, D., Douglass, J., Beane, R., Davis, C., Goldman, S., Kay, G., Gustavson, B., Saltoun, B. and Stewart, J., 1999. Petrology and geochemistry of late-stage intrusions of the A-type, mid-Proterozoic Pikes Peak batholiths (Central Colorado, USA): implications for petrogenetic models. Precambrian Research, 98, 271–305.

Srinivasan, K.N. and Roop Kumar, D., 1995. Orbicular structures from a diorite body within the Granitoid Complex of Nellore Schist Belt. J. Geol. Soc. India, 45, 277-283.

Stolz, A.J., Jochum, K.P., Spettel, B. and Hofmann, A.W., 1996. Fluid and melt-related enrichment in the subarc mantle:evidence from Nb/Ta variations in island-arc basalts. Geology 24, 587–590.

Streckeisen, A., 1967. Classification and nomenclature of igneous rocks. Final report of an inquiry. Neues Fahrbuch fur Mineralogie, Abhandhlungen, 107, 144-204.

Subba Rao, M.V., Divakara Rao, V., Balaram, V. and Ganeshwara Rao, T., 1992a. Source characteristics, petrogenesis and evolution of the LILE-enriched granitic terrain of the Kadiri region in Anantapur district, Andhra Pradesh. Proc. 28th Annual Convention and the Seminar on ‘Geophysics for Rural Development, Hyderabad, India, Dec. 1991, 108–117.

Subba Rao, M.V., Divakara Rao, V., Govil, P.K., Balaram, V. and Pantulu, G.V.C., 1992b. Geochemical and Sr isotopic signatures in the 2.6 By Lepakshi granite, Anantapur district, Andhra Pradesh: implications for its origin and evolution. Indian Minerals, 46, 289–302.

Subba Rao, M.V., Narayana, B.L., Diwakar Rao, V. and Reddy, G.L.N., 1998. Petrogenesis of the protolith for the Tirodi gneiss by A-type granite magmatism: the geochemical evidence. Curr. Sci. 76, 1258–1262.

Tatsumi, Y., Hamiliton, D.L. and Nesbitt, R.W., 1986. Chemical characteristics of fluid phase released from a subducted lithosphere and origin of arc magams: evidence from high pressure experiments and natural rocks. J. Volcanology and Geothermal Research 29, 293–309.

Venkatakrishnan, R. and Dotiwala, F.E., 1987. The Cuddapah salient: a tectonic model for the Cuddapah basin, India, based on Landsat image interpretation. Tectonophysics 136, 237–253.

Upadhyay, D., Raith, M.M., Mezger, K. and Hammerschmidt, K., 2006. Mesoproterozoic rift-related alkaline magmatism at Elchuru, Prakasam Alkaline Province, SE India. Lithos, 89, 447–477.

Vijaya Kumar, K., Ernst, W.G., Leelanandam, C., Wooden, J.L. and Grove, M.J., 2010. First Paleoproterozoic ophiolite from Gondwana: geochronologic–geochemical documentation of ancient oceanic crust from Kandra, SE India. Tectonophysics, 487, 22–32.

Vijaya Kumar, K., Leelanandam, C. and Ernst, W.G., 2011. Formation and fragmentation of the Palaeoproterozoic supercontinent Columbia: evidence from the Eastern Ghats Granulite Belt, southeast India. Int. Geol. Rev., 53, 11-12.

Vijaya Kumar, K., Ernst, W.G., Leelanandam, C., Wooden, J.L. and Grove, M.J., 2011. Origin of ~2.5 Ga potassic granite from the Nellore Schist Belt, SE India: textural, cathodoluminescence, and SHRIMP U-Pb data. Contrib. Mineral. Petrol., 162, 867-888.

Whalen, J.B., Currie, K.L. and Chappell, B.W., 1987. A-type granite: Geochemical characteristics, discrimination and petrologenesis. Contrib. Mineral. Petrol., 95, 407-419.

Wenner, J.M. and Lloyd, M.A., 2006. Trace element signatures and tectonic affinities of Proterozoic Atype granites and rhyolites in east-central Wisconsin, Geoscience Wisconsin, 17, 35-51.

Received on: 4.3.19; Revised on: 1.5.19; Accepted on: 27.5.19

Long term (1984-2013) winter temperature variability and cold wave analysis over Varanasi City

Priyanshu Gupta[1], Sunita Verma[1]*, R. Bhatla[2], Swagata Payra[3], and Pramod Kumar Yadava[1]

[1]Institute of Environment and Sustainable Development, Banaras Hindu University, Varanasi-221005, Uttar Pradesh, India.

[2]Depatment of Geophysics, Banaras Hindu University, Varanasi-221005, Uttar Pradesh, India.

[3]Department of Physics, Birla Institute of Technology Mesra, Jaipur Campus, Jaipur-302017, Rajasthan, India.

*Corresponding author: verma.sunita@gmail.com

ABSTRACT

Cold wave frequency (CWF), minimum temperature trend and their anomalies for the winter season (December-February) over Varanasi (India), have been studied for the period 1984-2013. Conventional and robust statistical methods have been applied to analyze the winter temperature trends. The maximum and minimum value of mean minimum temperature ranges from 8.39˚C/year and 11.26˚C/year in 1997 and 2009 respectively. Minimum temperature anomalies in winter season show 15 warmer and 15 colder conditions for the study period. The result indicates a systematic decrease in cold wave percentage from earlier (1984-1993) to last two decades (1994-2003 and 2004 to 2013) 52.1%, 26.1%, and 21.7%, respectively. The temperature analysis depicts that over Varanasi, average minimum temperature shows increasing trends with a change of + 0.039˚C/year during 30 years period. The cold waves are however marked by decreasing trend with 58.3% frequency change from earlier to recent decade and have become less frequent which may be due to the rapid growth of urbanization, industrialization and heavy pollution loads. But in contrary, a special occasion happened on 8th and 9th January 2013, which shows a long lasting with stronger intensity severe cold wave compared to last 30 years, which may be due to long spelled strong western disturbance. The cumulative wind speed and wind direction analysis shows that wind blows most commonly from the western side with an average wind speed of 1.98 knots for the period 1991 to 2013 over Varanasi.

Keywords: Cold wave events, Mann-Kendall test, Wind rose, Relative Humidity, Western Disturbance.Varanasi (india)

INTRODUCTION

Cold waves during winter are marked by a sharp and rapid fall of minimum and daily average surface temperature below certain thresholds. The northern parts of India especially the hilly regions and the adjoining plains are influenced by transient disturbances in the mid-latitude westerlies, which often have weak frontal characteristics. These are known as western disturbances (WDs). Nair et al. (2016) in their study, have described WDs as transient disturbances in the mid latitude westerlies and are followed by occurrence of cold waves mostly over the areas north of 20º N and rarely in areas south of this latitude. Varanasi lies in western Uttar Pradesh region of India and has a humid subtropical type of climate with some disparity in the temperatures of the seasons. Continental type of climate and winter rain arises due to western disturbance, may be the key factors in causing cold wave conditions in the city.

Dash and Mamgain (2011) in their study have found significant decreasing trends in the frequency and spells of cold nights in the country as a whole and in the north except western Himalaya for the period of 1969-2005. Long-term changes in local and regional weather patterns are observed in many regions of the country. Yan et al., (2002) have studied extreme

temperature trends of Europe and China. They concluded increases of warm extremes and decreases of cold extremes have accompanied the strong warming since 1961. Roy and Chatterji (1929) have also studied the probable origin of the cold wave in India. They have found an intense cold wave in the whole of the north-west and central part of India during the period Jan. 28 - Feb. 3, 1929. Based on different climatological features of cold wave and heat wave, many meteorological studies have been reported like, Raghavan (1966, 1967), Bedekar et al. (1974), Subbaramayya and Surya Rao (1976), De and Sinha Ray (2000), Pai et al. (2004) and De et al. (2005). Changes in the characteristics of surface air temperature over seven homogeneous regions in India, during the last century, have been examined by Dash et al. (2007) and Dash and Hunt (2007). There are earlier studies too that examined the analysis of trends in intensity and frequency of heat and cold waves (e.g. Alexander et al., 2006; Wang and Ding, 2006; Varfi et al., 2009; Spinoni et al., 2015). Some studies have been carried out to understand the patterns of long-term temperature change across India.

Similarly, Pramanik and Jagannathan (1954) studied maximum and minimum temperatures over India and they found that there is no general tendency for an increase or decrease in these temperatures. Jagannathan and Parathasarathy (1973), who analyzed the time series of mean annual temperatures over a set of eight Indian stations, concluded an increasing trend in the mean annual temperatures of Kolkata, Mumbai, Bangalore and Allahabad, and a decreasing trend at Cochin. Pant and Kumar (1997) in their study for the period 1881–1997 also reported that there is a significant warming trend of 0.57°C per hundred years. The magnitude of warming is higher in the post-monsoon and winter seasons. Attri and Tyagi (2010) and Rathore et al., (2013) in their studies over India show steadily increasing trend of minimum temperature since 1991. This rate of increase is slightly more during winter than the rate of increase in maximum temperature. Besides, Bhatla et al., (2016) analyze the frequency of the cold wave and severe cold wave events for post-Monsoon and winter season during 1971-2010 over different stations of Eastern Uttar Pradesh, India. Apart from these studies, Gupta et al., (2018) carried out characteristic analysis and decadal variability of cold wave and severe cold wave events over Indo Gangetic Plain. Their study indicated a more frequent occurrence of the cold wave over Amritsar followed by Delhi, Agra and least over Kolkata, as Kolkata is adjacent to the ocean. Their result shows that in Amritsar, minimum temperature ranges from 4.3^{0}C to 9.7 ^{0}C with a mean of 6.4 ^{0}C, while over Kolkata the spread of minimum temperature is rather on the higher side, with a minimum temperature of 12.62 ^{0}C, maximum of 19.15 ^{0}C and a mean of 15.06 ^{0}C for 1984-2013.

The main objective of this study is to analyze mean minimum temperature anomalies, trends and cold wave frequency during December, January, February (DJF) period over Varanasi, India since 1984-2013. The role of relative humidity in temperature change is also analysed during the study period. The wind rose plot gives an overview of dominant wind direction and speed for the winter period of 1991-2013.

DATA AND METHODOLOGY

Long term daily minimum temperature dataset at 1˚x1˚ grid resolution for period 1984-2013 during winter season (DJF) over Varanasi (25.34 ˚N and 82.97 ˚E) was obtained from Indian Meteorological Department (IMD). From this data, we have extracted Varanasi minimum temperature data at 25.34 ˚N and 82.97 ˚E. Averages of daily minimum temperature data have been calculated for the December, January, and February (DJF period), which implies (December previous year to February of reference year). Minimum temperature trends for the winter season (DJF) have been analysed by seasonal Mann-Kendall test. To find cold wave frequency, the IMD criteria (http://www.imd.gov.in/doc/termglossary. pdf) is followed. In this study, cold wave frequency was analysed for three different decades i.e. D1 (1984-1993), D2 (1994-2003), and D3 (2004-2013). For the study of minimum temperature anomalies, we have taken yearly average temperature and climatology difference. Comparative study of daily maximum and minimum value of

relative humidity and minimum temperature during 1991-2013 has also done in the present study. Relative humidity, wind speed and wind direction data for the

STUDY AREA

Uttar Pradesh is the most populous and the fourth largest state of India. It lies towards the north-central part of the country. It is divided into Western and Eastern Uttar Pradesh. Varanasi lies in the Eastern Uttar Pradesh, having coordinates 25.3˚ N and 83.0 2˚ E, and elevation, 86 meter . It is one of the seven sacred cities of Ancient India. It is located on the bank of River Ganga and expanded to 1528 Sq. km of area and cover 1.05% of forest. According to Köppen climate classification, climatic condition is humid subtropical type, with hot and humid summer and mild winter. Winter in Varanasi started from months of December to February, which slowly started freezing cold with the 5˚C temperature, because of cold winds from the Himalayas. The average rainfall is 1110 mm. The Different features and characteristics of Varanasi prove invaluable for temperature and cold wave frequency trend analysis.

RESULTS AND DISCUSSION

Trend Analysis of mean minimum temperature during winter

Time series of average minimum temperature, presented in Figure 1 for the winter season of 1984-DJF period was taken from IMD Observatory Ozone unit, Department of Geophysics BHU, Varanasi.

2013 over Varanasi, has been analysed. A positive trend was observed in the average minimum temperature of Varanasi, which indicates an increase in minimum temperature from 1984 to 2013. The Mann-Kendall test confirmed increasing trends at 5% significance level with a variation of minimum and maximum winter temperature between 8.39˚C/year to11.26˚C/year in 1997 and 2009, respectively. Sen's slope defined the magnitude of the trend, which reveals average minimum temperature changed by +0.039˚C/year during 30 years period. Average minimum temperature anomalies for the period 1984 to 2013 are shown in Figure 2. These anomalies are defined as yearly mean minimum surface temperature minus climatology (30 years average) of winter months. Warmer and colder temperatures from average values are defined as positive and negative departures. During 30 years studied period, Figure 2 depicts that year 2009 shows maximum temperature departure by +1.5˚C, while 1997 observed as the coldest year during which temperature departed by -1.3 ˚C. Further, it is also observed that the years 1987, 1994 to 1996, 1998, 2005 and 2009 shows the significant positive anomaly of value more than 0.5˚C. Similarly, the years having less than 0.5˚C anomaly are 1985, 1989, 1992, 1997, 2001 and 2013.

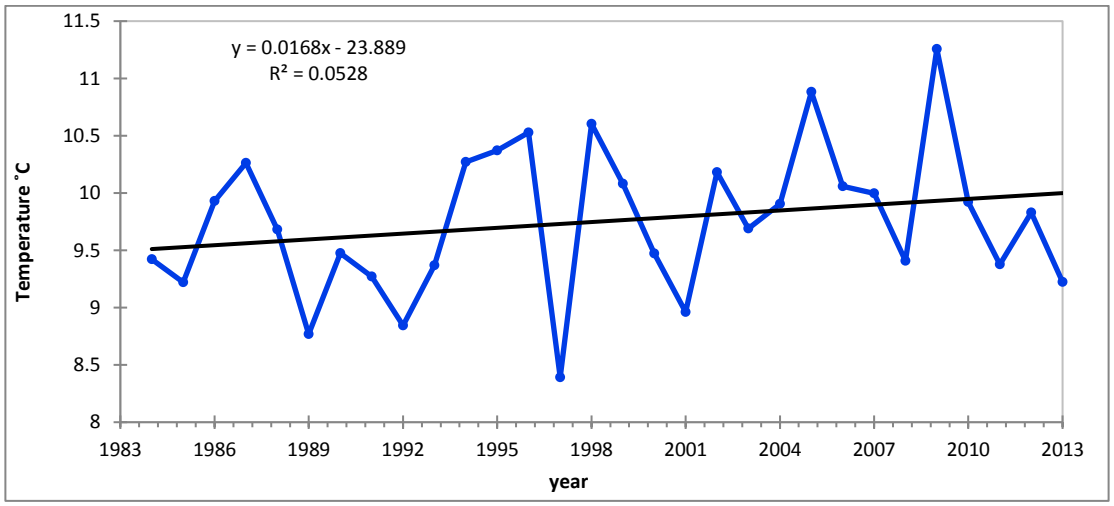

Figure 1. Trend analyses of winter mean minimum temperature over Varanasi.

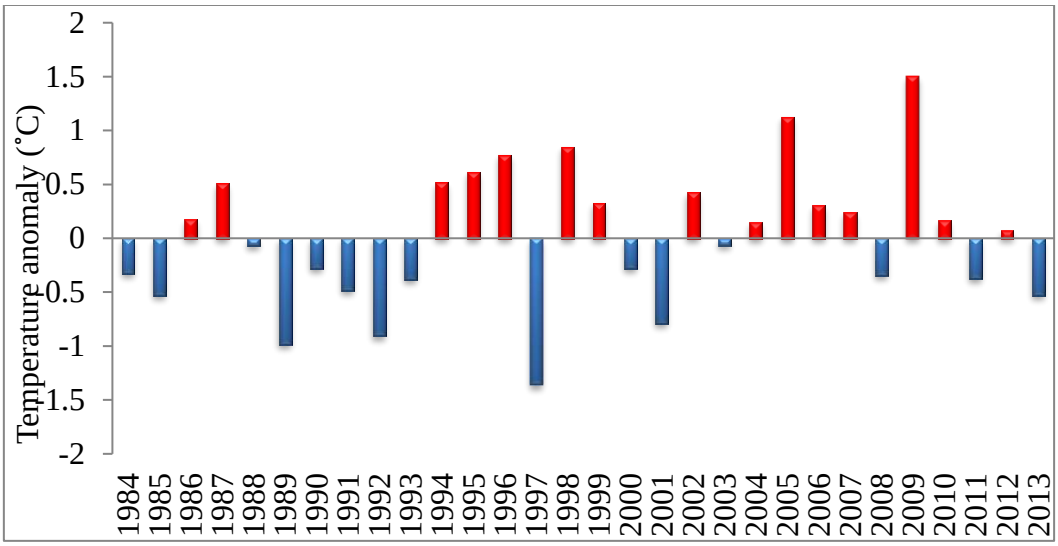

Figure 2. Mean minimum temperature anomalies in Varanasi during DJF period.

The dataset in Table 1 indicates that Varanasi experienced a decrease in both maximum (0.85˚C) and minimum (-1.36°C) value of mean minimum temperature during the 1994-2003 period. While the later period of 2004-2013 is dominated by upward trends that are most strongly evident in mean minimum temperature (1.5°C for the maximum value of minimum temperature and -0.53°C for the minimum value of mean minimum temperature). This signifies that decadal variations of winter season mean minimum temperature has an increasing pattern from D1 to D3 decades. Earlier 1984-1993 decade, indicates minimum temperature decreased by -0.33˚C/decade, while recent two decades D2 (1994-2003) and D3 (2004-2013), show an increase in mean minimum temperature by 0.11˚C/decade and 0.23˚C/decade respectively. Based on these results, it appears very likely that much of Varanasi has experienced an increase in the average temperature.

Table 1. Maximum, minimum and average minimum temperature and their departure for D1, D2 and D3 decades.

	D1(1984-1993)		D2(1994-2003)		D3(2004-2013)	
	Temperature	Departure	Temperature	Departure	Temperature	Departure
Maximum of mean T_{min}(˚c)	10.26	0.51	10.6	0.85	11.26	1.5
Minimum of mean T_{min} (˚c)	8.77	-0.98	8.39	-1.36	9.22	-0.53
Average of mean T_{min}(˚c)	9.42	-0.33	9.85	0.11	9.98	0.23

Frequency Analysis of cold wave during winter

Comparative multi-decadal variations of cold wave percentage frequency for three different decades of DJF; D1 (1984-1993), D2 (1994-2003) and D3 (2004-2013) over Varanasi, are shown in Figure 3. There is a systematic decrease in cold wave percentage from earlier (D1) to last two decades (D2 and D3). 52.1%, 26.1% and 21.7%, respectively.

Table 2 shows the temperature departure of daily minimum temperature from daily normal. During 30 years of climatology; year 1984, 1985, 1986, 1989, 1990, 1991, 1992, 1993, 1997, 1998, 2001, 2003,2008, 2012 and 2013 recorded temperature drop of -4˚C to -5˚C for less than 10˚C and -5˚C to -6˚C for more than10˚C normal temperature, which reveals cold wave conditions, While the years 1987, 1988, 1994, 1995, 1996, 1999, 2000, 2002, 2004, 2005, 2006, 2007, 2009, 2010 and 2011 indicates the complete absence of CW days. In 1984 cold wave is observed on 31st January and 23rd February, whereas in 1985, CW prevailed on 20th December. In the year 1986 and 1989, CW persists for two consecutive days i.e. 6th January and 7th January and 13th to 14th January respectively. During 1991, CW was prevalent on 3rd and 15th January. The year 2003 recorded the maximum number of CW days on 14th, 16th, and 23rd January during which daily actual temperature from daily normal was departed by -4.4˚C, -4.77˚C and -4.15˚C respectively. In the year 2013, CW events occurred on 7th January and severe cold wave on 8th and 9th January which shows daily temperature departure of -4.55˚C, -6.19˚C and -6.86˚C respectively. During 1984 to 2013 periods Varanasi recorded a low temperature of 3.2˚C during January. The present study indicates that the occurrence of cold wave events during the winter season was more intensified in the month of January.

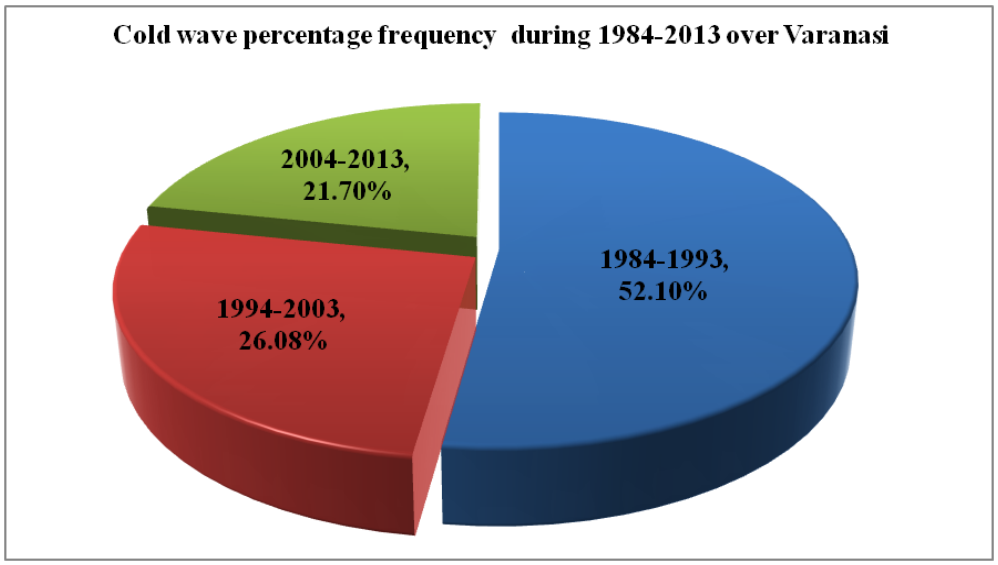

Figure 3. Decadal variation of cold wave percentage frequency over Varanasi during 1984-2013.

Table 2. Daily minimum temperature departure during winter period of 1984-2013 over Varanasi.

Varanasi				
Year	**Date**	**Daily actual temperature (˚C)**	**Daily normal temperature (˚C)**	**Departure**
1984	Jan-31	5.26	9.64	-4.38
	Feb-23	6.65	12.34	-5.56
1985	Dec-20	5.09	9.1	-4.0
1986	Jan-06	3.24	7.7	-4.5
	Jan-07	3.71	7.8	-4.15
1989	Jan-13	4	8.07	-4.07
	Jan-14	3.6	8.19	-4.58
1990	Jan-03	4.1	8.2	-4.1
1991	Jan-03	4.12	8.17	-4.05
	Jan-15	4.27	8.4	-4.17
1992	Jan-02	3.97	8.16	-4.19
1993	Feb-22	6.69	12.2	-5.5
1997	Dec-10	5.34	10.57	-5.24
1998	Dec-23	5.17	9.23	-4.06
2001	Feb-04	5.05	9.72	-4.67
2003	Jan-14	3.77	8.19	-4.4
	Jan-16	3.91	8.67	-4.77
2008	Jan-23	4.35	8.5	-4.15
	Dec-18	5.41	9.5	-4.1
2012	Feb-01	5.63	9.76	-4.13
	Dec-22	4.85	9.05	-4.2
2013	Dec-25	5.14	9.21	-4.07
	Jan-07	3.31	7.85	-4.55

Overall, cold waves are less frequent, with short intensity over the past 30 years, which may be due to the rapid growth of urbanization, industrialization and heavy pollution loads which restricts cooling by restricting the outgoing long wave radiation (OLR).

Comparative analysis of Temperature and Relative Humidity

Figure 4 shows the minimum temperature and Relative Humidity (RH) over Varanasi during 1991-2013, as the data is available only for that time period. The RH trend in Figure 4 indicates an inverse relationship with temperature, as temperature increases, the relative humidity is observed to decrease during most of the study period. This may be due to the fact that as the temperature increases, air can hold more water molecules and its relative humidity decreases. These decreasing trends of cold wave also reveal that presence of water molecules which trapped the OLR.

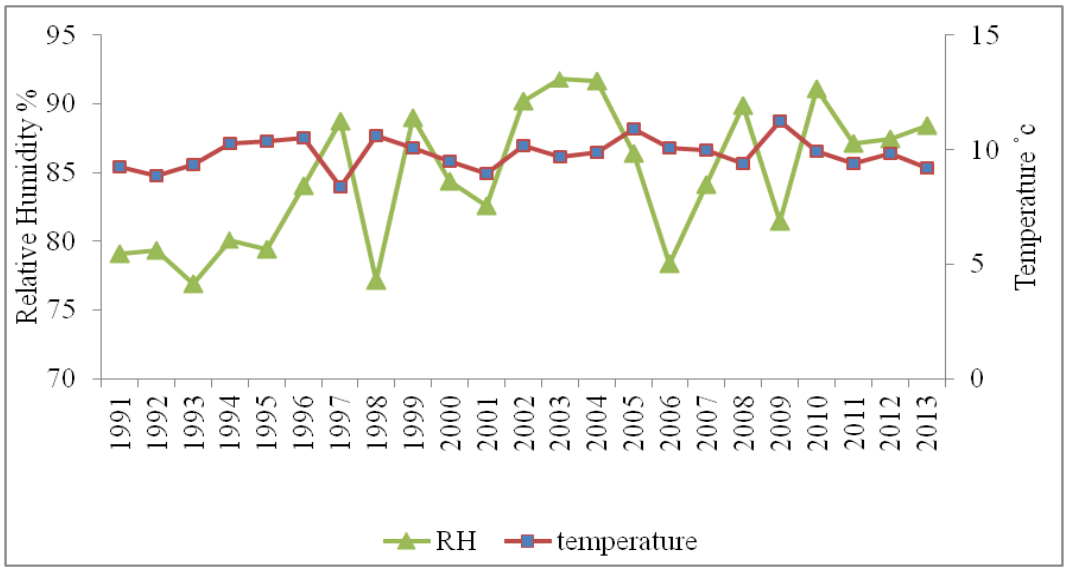

Figure 4. Comparative study of mean minimum temperature and relative humidity during 1991-2013.

Analysis of wind speed directions over Varanasi during DJF period

Figure 5 shows the wind direction conditions for winter season of 1991-2013, distributed over 16 wind directions and 6 wind speed classes, including calm conditions. The wind direction indicates that the wind blows mostly from western side (approximately 23% of the time). In general, average wind speed remains 1.98 knots during the study period. From the wind speed distribution shown in the wind rose plot, it is evident that wind speed ranges between 0.97-4.08 knots are most common, whereas wind speed above 4.08 knots are relatively weak.

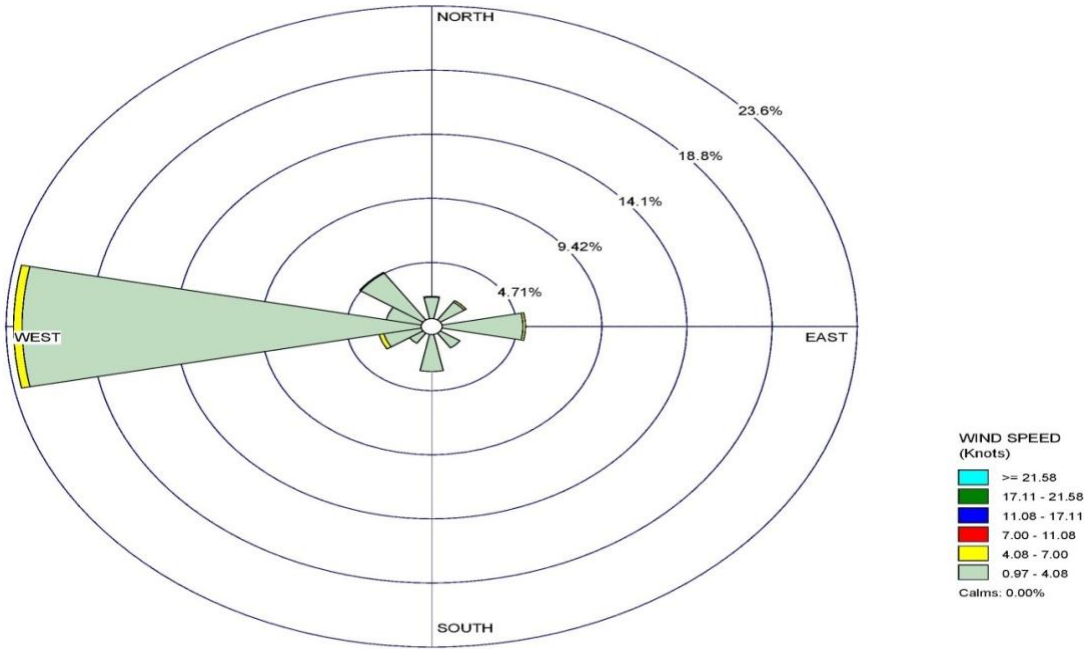

Figure 5. Prominent wind direction over Varanasi during winter period.

CONCLUSIONS

This study investigated the trend of the winter temperature, cold wave frequency and minimum temperature anomalies for the DJF period over Varanasi during 1984-2013. The following conclusions may be drawn from the present analysis:

- For Varanasi, the statistical trend was assessed at the 5% significance level. Varanasi, average minimum temperature shows increasing trends with a change of + 0.039˚C/year during 30 years period.
- A maximum and minimum value of mean minimum temperature during 1997 and 2009 ranges from 8.39˚C/year and 11.26˚C/year respectively.
- During 1984-2013, the study of winter minimum temperature anomalies, 15 year shows positive anomalies and 15 years as negative anomalies.
- The year 2009 shows maximum temperature departure by 1.5˚C, while 1997 observed as the coldest year during which temperature departed by -1.3 ˚C.
- A decadal variation of cold wave percentage frequency reported for the period 1984-1993, 1994-2003 and 2004-2013. Study regions reveal a gradual decrease in the percentage of cold extremes from previous to recent decades. In Varanasi, 52.1%, 26.1% and 21.7% of CW percentage observed during D1, D2 and D3 decades respectively.
- Overall, the average minimum temperature for the DJF period increases and cold wave events has been decreased during 1984-2013 years of Varanasi and it is also observed that relative humidity is inversely related to minimum temperature.
- The wind analysis over Varanasi shows that the most dominant wind direction is westerly (23%) with an average wind speed of 1.98 knots. These westerly winds may be responsible for the western disturbance, which causes winter rain towards the northern part of India and responsible for cold wave phenomena.

ACKNOWLEDGEMENTS

The authors wish to express sincere thanks to India Meteorological Department for providing the necessary data. The first author likes to thank Ms. Shruti Verma and Mr. Barunava Mandal for the support and extending help during the study. The corresponding author would also like to thank funding support under MoES (MoES/16/18/2017-RDEAS) project.

Compliance with Ethical Standards

The authors declare that they have no conflict of interest and adhere to copyright norms.

REFERENCES

Alexander, L.V., Zhang, X., Peterson, T.C., Ceaser, J. et al., 2006. Global observed changes in daily climate extremes of temperature and precipitation, J. Geophys. Res., 111, D05109, doi: 10.1029/2005JD006290.

Attri, S.D. and Tyagi, A., 2010. Climate profile of India, Met Monograph, Environment meteorology No. 01/2010, Indian Meteorological Department**.**

Bedekar, V.C., Dekate, M.V. and Banerjee, A.K., 1974. Heat and cold waves in India, Forecasting Manual-Part-IV-6, India Meteorological Department.

Bhatla, R., Gupta, P. and Tripathi, A., 2016. Cold wave/severe cold wave events during post-Monsoon and winter season over some stations of eastern Uttar Pradesh, India, J. Clim. Change, 1(2), 27-34.

Dash, S.K. and Hunt, J.C.R., 2007. Variability of climate change in India, Curr. Sci., 93(6), 782–788.

Dash, S.K., Jenamani, R.K., Kalsi, S.R. and Panda, S.K., 2007.Some evidence of climate change in twentieth-century India, Clim. Chang. 85, 299–321, DOI 10.1007/s10584-007-9305-9

Dash, S.K., and Mamgain, A., 2011. Changes in the frequency of different categories of temperature extremes in India, J. Appl. Meteorol. Climatol., 50, 1842-1857.

De, U.S. and Sinha, Ray, K.C., 2000. Weather and climate related impacts on health in mega cities, WMO Bulletin, 44(4), 340-348.

De, U.S., Dube, R.K. and Prakasa Rao, G.S., 2005. Extreme weather events over India in last 100 years, J. Indian Geophys. Un., 9(3), 173-187.

Gupta, P., Bhatla, R., Payra, S., Yadava, P.K. and Verma, S., 2018. Cold wave and severe cold wave events over Indo-Gangetic Plain: Analysis and comparison for decadal variability, Int. J. Earth Atmos. Sci., 5(2), 101-109.

Jagannathan, P. and Parthasarathy, B., 1973. Trends and periodicities of rainfall over India, Monthly Weather Rev., 101, 691–700.

Nair, A.S., Pai, D.S. and Rajeevan, M., 2016. Climatology and trend of cold waves over India during 1971-2010, MAUSAM, 67(3), 651-658.

Pai, D.S., Thapliyal, V. and Kokate, P.D., 2004. Decadal variation in the heat and cold waves over India during 1971-2000, MAUSAM, 55(2), 281-292.

Pant, G.B. and Kumar K.R., 1997. Climates of South Asia. John Wiley and Sons Ltd., Chichester, UK.

Pramanik, S.K. and Jagannathan, P., 1954. Climatic changes in India rainfall, Ind. J. Meteorol. Geophys, 4, 291–309.

Raghavan, K., 1966. A climatological study of severe heat waves in India, Indian J. Met. Geophys., 17(4), 581-588.

Raghavan, K., 1967. A climatological study of severe cold waves in India, Indian J. Met. Geophys., 18(1), 91-96.

Rathore, L.S., Attri S.D. and Jaswal A.K., 2013. State level climate change trends in India", Meteorological Monograph, No. ESSO/IMD/EMRC/02/2013.

Roy, S.C. and Chatterji, G., 1929. Probable origin of the cold wave in India, Nature, 124, 579.

Spinoni, J., Lakatos, M., Szentymrey, T. et al., 2015. Heat and cold waves trends in the Carpathian Region from 1961 to 2010", Int. J. Climatol., 35, 4197-4209.

Subbaramayya, I. and Rao Surya, D.A., 1976. Heat wave and cold wave days in different states of India, Indian J. Met. Hydrol. and Geophys., 27(4), 436-440.

Varfi, M.S., Karacostas, T.S., Makrogiannis, T.J. and Flocas, A.A., 2009. Characteristics of the extreme warm and cold days over Greece, Adv. Geosci., 20, 45-50.

Wang, Z.Y. and Ding, Y.H., 2006. Climate change of the cold wave frequency of China in the last 53 years and the possible reasons, Chinese J. Atmos. Sci., 30(6), 1068–1076.

Yan, Z., and Co-authors, 2002. Trends of extreme temperatures in Europe and China based on daily observations, Clim. Change, 53, 355–392.

Received on: 6.2.19; Revised on: 6.4.19; Accepted on: 8.5.19

Accuracy assessment of land use/land cover classification in parts of Kadapa district (Andhra Pradesh, India), using remote sensing and GIS

M. Rajasekhar, G. Sudarsana Raju*, R. Siddi Raju, M. Ramachandra and B. Pradeep Kumar

Dept. of Geology, Yogi Vemana University, Kadapa, Andhra Pradesh, India-516005.
*Corresponding author: gsraju05@gmail.com

ABSTRACT

This study assesses land use/land cover (LULC) with Accuracy Assessment (AA) in Chennur mandal of the Kadapa district (Andhra Pradesh), using satellite images and socio-economic data. Spatial and temporal elements of LULC were measured using Landsat 8 OLI/TIS images, following a supervised classification algorithm technique in ERDAS Imagine software. Accuracy of the Landsat-derived LULC maps are about 84%. The study indicated that considerable evolution of built-up areas and barren/waste lands in the study area of the Kadapa district resulted in significant decrease in the area of water bodies, agricultural land and the forest cover. The built-up land growth has been large due to rising population growth. Fast urban development through infilling of low-lying zones and clearing of forest regions affected the environment, as well as its economic development. The major LULC groups include agricultural land (55.28%), water bodies (5.45%), and built-up land (6.65%), forest (2.61%) and wastelands (30.01%). The present study can be used by decision makers to develop economically sustainable plan for the protection of environment.

Keywords: Land use/Land cover, Accuracy Assessment, Remote Sensing, GIS, Kappa coefficient, Kadapa district

INTRODUCTION

LULC are two unique advances in recent past, which are being consistently used (Rawat, et.al., 2013). Land cover deals with the physical characteristics of the Earth's surface, like forest, water bodies, soil and other physical features, including those made by man-made activities. While, Land use, insinuates the way by which individuals and their characteristic environment, uses the land for beneficial needs (Rwanga and Ndambuki, 2017) The LULC case of a region is a result of characteristic and financial related factors and their utilization by the man in all actuality. LULC is also related to the demands of increasing urbanization and thus, resulted into increase of population in present's years. Changes in LULC use, don't really always suggest a degradation of the land (Rajasekahr et.al , 2017). In any case, LULC is driven by collection of social causes, impact biodiversity, water, and radiation spending plans, pursue gas releases and distinctive methodology, that get together to impact the air and biosphere and affects the regular environment (Rajasekhar et al., 2018a).

The current technology of Remote Sensing (RS) incorporates both, aerial as well as satellite-based frameworks, which gather physical information on a redundant premise with speed alongside Geographical Information System (GIS), which encourages us to break down the information and streamlining the entire planning process. Application of RS data has made it possible to study the changes in land cover in lesser time, at low cost and with better accuracy (Rawat, 2015). Further, geospatial methods are used to determine precise and convenient data on the spatial appropriation of LULC changes over a large region

(Rajasekhar et al., 2018b). Landsat 8 OLI/TIS images have been found useful to study the world's surface since last three decades (USGS, 2014). Furthermore, the entire Landsat record is now available for recognizing and checking changes in man-made and physical circumstances (Treitz and Rogan, 2004). Thus , LULC information is essential for the approval of land use plans in a growing population scenario (Sudhakar et al., 2006).

As a matter of fact, several articles have been written on LULC analysis of the surrounding areas, in particularly the semi- arid regions of Kadapa district, Andhra Pradesh, India, (Siddi Raju et al., 2018). Traditionally, the LULC approach in the regions depends on topographic and classification on LULC. However, in recent decades, field studies on the characteristics and behaviour of the LULC, as well as developments in the field of RS and GIS have strengthened the mode of detection of such changes (Rajasekhar et al., 218c). Generally the reference data is represented in the matrix columns, which are compared with the map data, represented in the matrix rows. The values in the matrix diagonal represent the agreement between the two data sets. The confusion matrix is considered a valid method to represent the accuracy of LULC maps (Thenkabail et al., 2007).

STUDY AREA

The study area is located in the Survey of India (SOI) topo sheet No's: 57 J/14, 57 J/13 and 57 N/2 on 1:50,000 scale, and lies between 78^0 44' 25" to 78^0 54' 25" E and 14^0 30' 0" to 14^0 36' 28" N (Figure 1), comprising a total geographical area of about 98.27 km^2. A prevalent examination soil overview of Kadapa district displays the event of selective soil grouping and their relationship in the study region. The Penna River is the source of water for agriculture, drinking and different activities for the people, who are living on the two sides of the stream. The groundwater table has radically gone down because of sinking of bore wells and sparse rain and the non availability of any surface water bodies. The location map of the study region is shown in Figure 1.

METHODOLOGY

The present study has been categorised into two groups: LULC classification and AA. The LULC grouping and AA, was done according to the procedure exhibited in Figure 2.

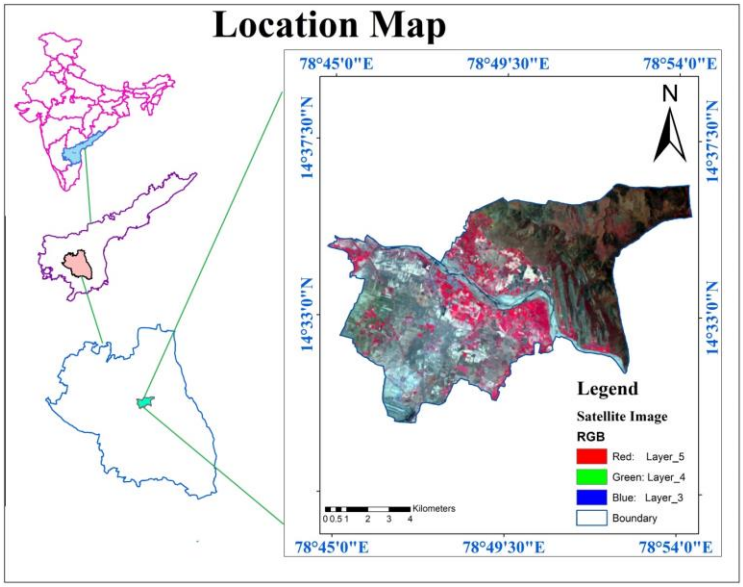

Figure 1. Location map of the Study area

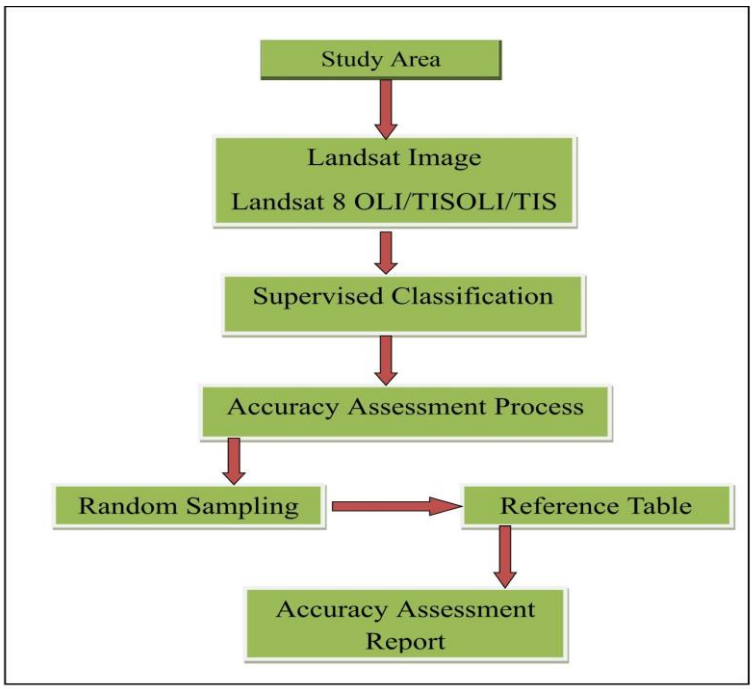

Figure 2. Schematic of work flow for LULC and accuracy assessment.

Table 1. Details of Landsat 8 OLI/TIS used for classification.

Types of data/Software	Details of data	Sources
Landsat 8 Satellite Imagery	Path/row: 144/50 dated:	https://earthexplorer.usgs.gov/

Land use/Land cover Classification

Image Pre-Processing

LULC classification carried out through supervised image classification in Erdas Imagine 2014 software, using Landsat 8 OLI/TIS satellite imageries over the study area, which were acquired form USGS Earth Explorer (https://earthexplorer.usgs.gov/). In the present study, an integrated use of multispectral satellite data is utilized for the generation of database and extraction of numerous LULC patterns. Details of the data used are shown in Table 1. LULC parameters were analysed and classified into 5 classes, associated with their orientation in space (Sreenivasulu, et al., 2014). The determination of the Landsat 8 OLI/TIS images was impacted by low cloud cover over the study area (Table 1). These images are pre-processed by clip methods using geospatial techniques such as, Erdas Imagine 2014 and ArcGIS 10.4 software's.

Land use/Land cover (LULC): Supervised Classification

ERDAS Imagine 2014 software carried with supervised classification using maximum likelihood algorithm method, resulted into the LULC classification in the studied area. The underlying theory shows that these probabilities are the equivalent for all classes and typical dispersion of info groups. According to the signatures classification, five LULC types have been recognized in the present study: (i)

Forest (ii) Irrigated land (iii) Barren /Wastelands (iv) Built-up land (v) Waterbodies. The supervised classification was associated after chosen Area of Interest (AOI), which is called training sites (Wolch et al., 2014). More than one training site was used to address a particular class. Figure 3 describes the four categories, Figures 3a to 3d. Figure 3a denotes the pixel reflection in the satellite imagery as red colour, which indicates agricultural fields in the earth surface. Figure 3b and 3c, shows blue colour in satellite image, indicating built-up land on the Earth surface as shown in Figure 3d. The training sites were selected in agreement with the Landsat Image, Google Earth and Google Map.

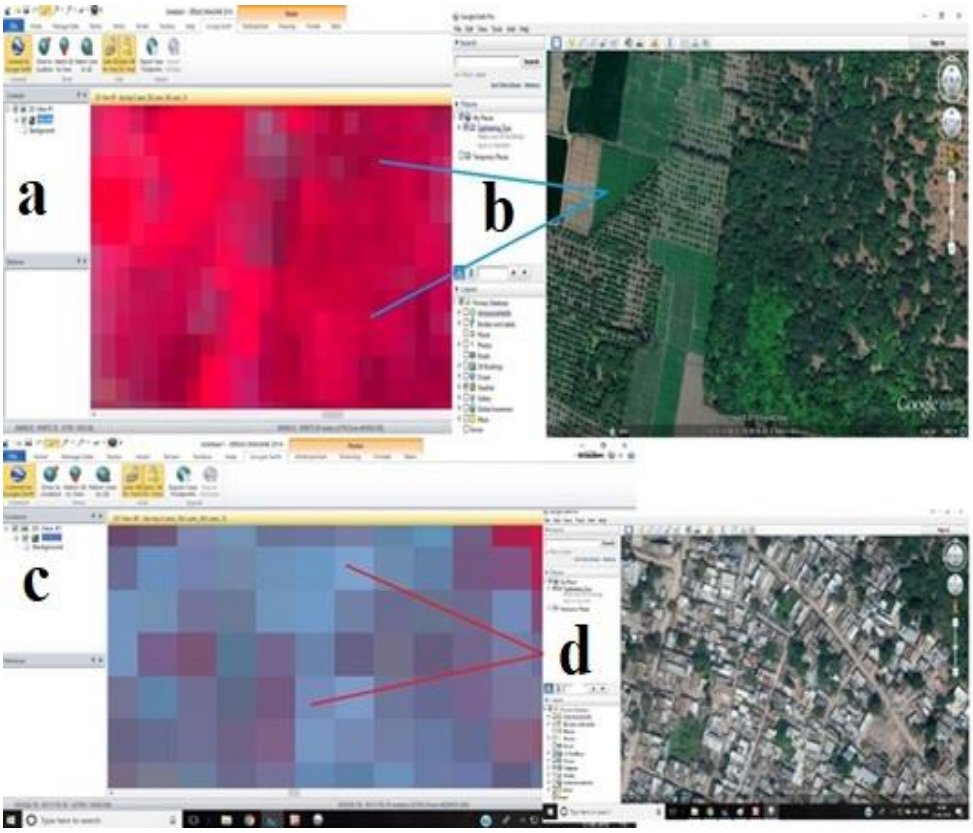

Figure 3. Identification of training sites using Landsat image (Erdas Imagine 2014) and Google earth

Training Sites

The first step in undertaking a supervised classification is to define the areas that will be used as training sites for each land cover class. This is usually done by using the on-screen digitized features. The created features are called Area of Interest (AOI).The selection of the training sites was based on those areas which are clearly identified in all sources of images. In this study, one hundreds training sites have been identified.

Extraction of Signatures

It is usually done by using the on-screen digitized features (Punia et al., 2011), which are called as AOI. In the present study, as mentioned earlier, one hundred training sites were recognized (Figure 4).

Class #	Signature Name	Color	Red	Green	Blue	Value	Order	Count	Prob.	P	I	H	A	FS
1	Forest-Deciduous (Dry/Moist/Th		0.000	0.392	0.000	14	34	1342	1.000	✔	✔	✔	✔	
2	Waste Lands-Scrub Land- Open		0.647	0.165	0.165	11	75	379	1.000	✔	✔	✔	✔	
3	Built-up Land (Rural)		1.000	0.000	0.000	6	79	20	1.000	✔	✔	✔	✔	
4	Waterbodies		0.000	0.000	1.000	1	80	48	1.000	✔	✔	✔	✔	
5	Agriculture Land		1.000	1.000	0.000	2	81	118	1.000	✔	✔	✔	✔	

Figure 4. Schematic Signature Editor for LULC and accuracy assessment.

RESULTS AND DISCUSSION

Land use / Land cover by using Remote Sensing data

Geospatial techniques are important to identify LULC in a certain area. In order to identify RS data, the selection of an appropriate method for detecting changes, is essential (Areendran et al., 2013). The LULC classifications in the present study were done utilizing Landsat 8 OLI/TIS, at a resolution of 30 m. The satellite information was used in the wake of a thourough field check (Malaviya et al., 2010). The different LULC classes deciphered in the present study incorporate, agricultural land, built-up land, barren/waste land, forest, and water bodies (Figure 5).

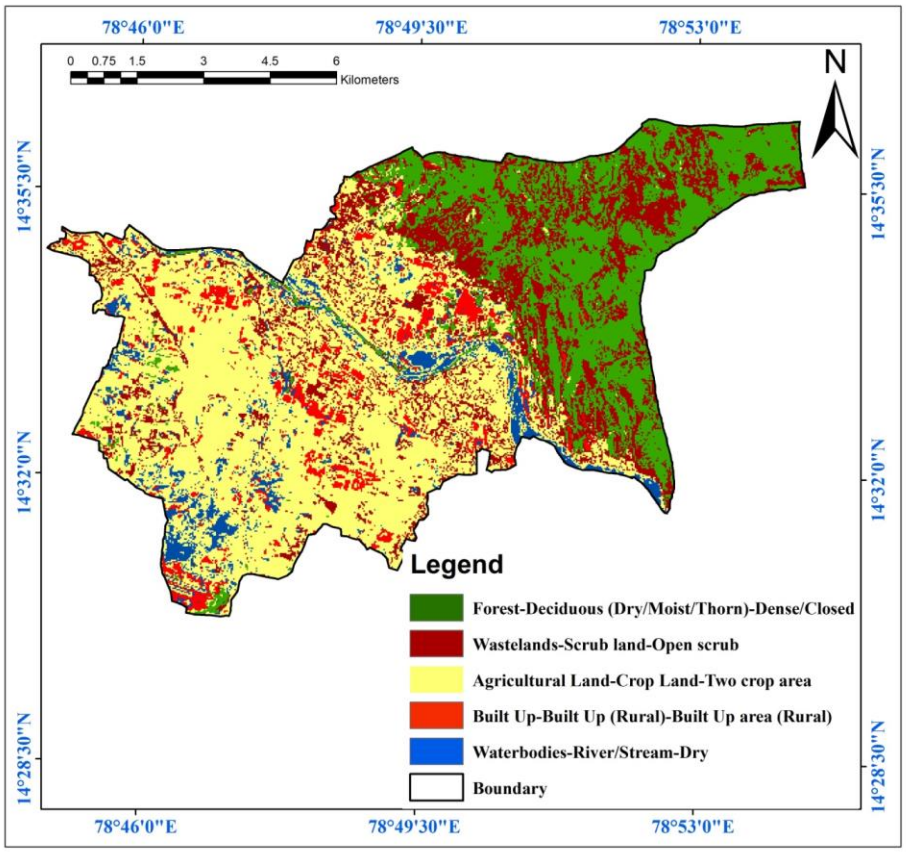

Figure 5. Classified map of study area.

Agriculture Land

Agricultural land with plantations and manors, are considered in this category. The agricultural land of the studied region is about 55.28% (54.33 km^2). Irrigated lands are categorised as areas with yield. Wet cultivated regions include areas with rice, paddy, groundnut, and vegetables plantation. Similarly, dry cultivation incorporates, Bengal gram, red gram, and groundnut, and etc. A total of 11 points collected on the basis of field work

Forest

Forest land includes thick and dense scrub of trees. The forest is recognized by their red to diminish green tone and moving in size having an irregular in shape with smooth texture. The forest lands are found on the N-W and N-E parts of the present study area. The complete region of vegetation is about 2.61% (2.56 km^2), which covers thick and scrub backwoods. The general grouping of forest lands is scrubs and littler trees which are dominating in this class. In the satellite images, such vegetation/scrub is distinguished by the green tone with a smooth surface. These terrains are liable to degradation and disintegration. Such territories are distinguished from their yellowish tone and their relationship with uplands, and their unpredictable shapes. Land with such scrubs are found in the N-E part of the present study region.

Built up Land

Built up land is the land covered by settlements and in the present study area, they cover 6.6% (6.53 km^2). It covers urban areas, towns, villages, industrial and commercial complexes and institutions, including towns and villages like Chinnamachu Palli, Obulama Palli, Kanuparty, Dowthapuram, Duggana Palli, Balasingani Palli, Nazeera Palli, Rudgrabharathi Petta etc. The transportation in such areas is by roads.

Water bodies

The consolidated water bodies included both intrinsic and man-made water features, like rivers, streams, lakes, channels, tanks, and reservoirs, which appear dark in tone in the satellite imagery. The shallow water and significant water features appear in light blue to diminish blue in shading. Tanks with plantation are recognized by the square shape in blue shading tone, which includes little streams in forest regions. Tanks are generally concentrated in the centre of the region, with a few dry tanks disseminated around the eastern parts. Water bodies constitute about 5.45% (5.36 km^2) of the area.

Barren/Waste Land

The wastelands, which do not bolster any vegetation, are categorized into salt-affected land, sandy regions, and rocky lands with and without scrublands. Such terrains are framed because of the physical properties of soil, temperature, precipitation, and neighbourhood characteristics conditions. In the present study area, it constitutes almost 30.01% (29.49 km^2), major part of which occur in the south-western part.

Accuracy Assessment

In grouping procedure, the role of Accuracy Assessment (AA) is quite vital. For the significant accentuation for exactness evaluation, pixel choice was on zones that could be obviously distinguished on Landsat high-resolution image, Google Earth and Google Map (Schull et.al, 2005). Image was characterised at 50 points. Topographical guides and Google Earth maps were utilized as a kind of perspective source to group the selected features (Dewan and Yamaguchi, 2016). Table 2 demonstrates the connection between ground truth information and the relating characterized information, revealed through the error matrix report. The Accuracy assessment can be computed by:

$$\text{The overall accuracy assessment} = \frac{\text{No.of correct points}}{\text{Total number of points}} = \frac{42}{50} = 84\%$$

Table 2. Theoretical error matrix in LULC classification.

Classified	Wastelands	Waterbodies	Agriculture	Forest	Built-up Land	Total Classified Points
Wastelands	5	0	0	1	0	6
Waterbodies	0	10	0	2	0	12
Agriculture	0	2	9	0	0	11
Forest	0	0	1	13	1	15
Built-up Land	0	0	1	0	5	6
Total Classified Points	5	12	11	16	6	50
Total Corrected Reference Points	42					
Total "True" Reference Points	50					

Table 2 shows a theoretical confusion matrix (error matrix) of a LULC classification. The columns of the confusion matrix show to which classes the pixels is in the validation set belong (ground truth) and the rows show to which classes the image pixels have been assigned to in the image. The diagonal show the pixels that are classified correctly. Pixels that are not assigned to the proper class do not occur in the diagonal and give an indication of the confusion between the different land-cover classes in the class assignment.

Furthermore, the off-diagonal elements in the rows of the confusion matrix, divided by the total number of pixels assigned to the Landsat image class corresponding to the row, represent the commission errors and describe the confusion between that image class and describes the other land-cover classes. The commission errors describe the chance that a pixel that has been assigned to a particular class actually belongs to one of the other classes.

Moreover, this study considered other metrics derived from the error matrix to further describe accuracy assessments including; commission and omission error, sensitivity and specificity, positive and negative predictive power and Kappa statistics. Information on these concepts can be found in Fielding and Bell (1997)

KAPPA analysis is a discrete multivariate technique used in accuracy assessments (Jenness, et al, 2007). The Kappa statistics are also computed based on formulation given below:

Sensitivity = $\frac{a}{a+b}$ (Equivalent to Producer's Accuracy)

Specificity = $\frac{d}{c+d}$

Commision Error = 1- Specificity

Ommision Error = 1- Sensitivity

Positive predictive Power = $\frac{a}{a+b}$ (Equivalent to User's Accuracy)\

Negative predictive Power = $\frac{d}{c+d}$

where:

a = number of times a classification agreed with the observed value

b = number of times a point was classified as X when it was observed not to be X.

c = number of times a point was not classified as X, when it was observed to be X.

d = number of times a point was not classified as X when it was not observed to be X.

Total points = $N = (a + b + c + d)$

KAPPA analysis yields a Khat statistic (an estimate of KAPPA), that is a measure of agreement or accuracy (Congalton, 1991). The Khat statistics can be computed as;

$$K = \frac{N \sum ir=1 xii - \sum ir=1 (xi + Xx+1)}{N\ 2 - \sum ir=1 (xii\ Xx+1)}$$

Where;

r = number of rows and columns in error matrix, N = total number of observations (pixels)

X_{ii} = observation in row i and column i,

Xx = No. of points correctly classified

Xi = marginal total of row i, and X+i = marginal total of column i.

A Kappa coefficient close to 1 suggests impeccable affirmation, whereas close to zero, infers that the comprehension is no better than would be ordinary by chance. As indicated by (Treitz and Rogan, 2004), rating criteria of Kappa statistics is reproduced in Table 3.

Table 3. Rating criteria of Kappa statistics.

S.No	Kappa statistics	Strength of agreement
1	<0.00	Poor
2	0.00 - 0.20	Slight
3	0.21 - 0.40	Fair
4	0.41 - 0.60	Moderate
5	0.61 - 0.80	Substantial
6	0.81 - 1.00	Almost perfect

Using the formulae equipped accuracy assessment section, diverse precision evaluating parameters were enrolled and arranged in Table 4 and Table 5. The results from the AA showed a general accuracy found from random sampling process for the images to be about 84%. User's accuracy extended from 81.82% to 86.67% while producer's accuracy ranged from 81.25% to 100% (Berberoglu and Akin, 2009). The wide scope of accuracy demonstrates extreme disarray of barren/waste land with other LULC classes. The proportion of producer's accuracy (sensitivity) reflects the precision of forecast of the particular classification.

Table 4. Category wise accuracy assessment statistical parameters.

Observed proportion of agreements (Po)	Expected proportion of agreement (Pe)	Kappa coefficient (**K**)
0.9674	0.85	0.782
0.8795	0.613	0.689
0.8632	0.805	0.298
0.9609	0.818	0.785
0.9674	0.793	0.843
0.9707	0.547	0.935

Table 5. Category wise accuracy assessment statistical parameters.

Percentage Accuracy	**84.00**	
User Accuracy		**Producer Accuracy**
Wastelands	83.33	100.00
Waterbodies	83.33	83.33
Agriculture	81.82	81.82
Forest	86.67	81.25
Built-up Land	83.33	83.33

The User's accuracy replicates the unwavering quality of the grouping to the user. User's is the more important proportion of the classification's real utility in the field. Barren/Waste land was observed to be progressively dependable with 100% of user accuracy. The commission error replicates the focuses which are incorporated into the classification while they truly don't belong to that category. For example, the commission error is most astounding in the built-up zones which implied that increasing number of points (Rwanga and Ndambuki, 2017) which don't fall under this classification are classified as built up areas. Similarly, the omission replicates the number of points which are excluded in the class while they truly have a place with the classification.

The omission error, if there should be an occurrence of Barren/uncovered land, is increasingly (0.7333) with 10 which really have a place with this classification not being sorted in this class. In this present study, a general Kappa coefficient of 0.722 was estimated which is evaluated as significant. Aside from generally characterization accuracy, the above-individualized parameters give a classifier an increasing point by point depiction of the model execution of the specific class or classification in study, as appears in Figure 6.

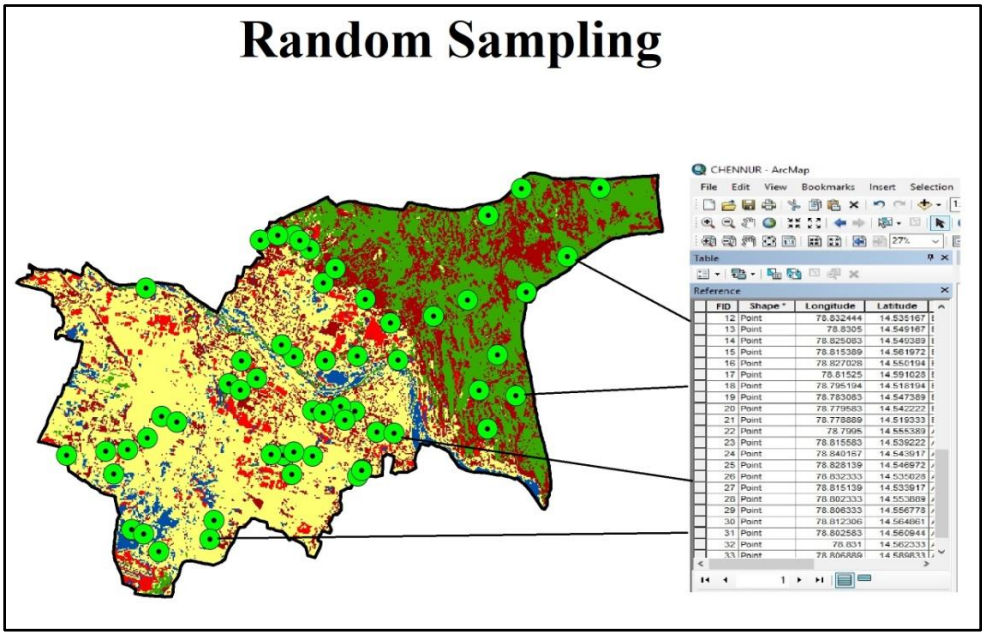

Figure 6. Landsat (classified) image of the study area covered with 50 points from random sampling.

CONCLUSIONS

Remote sensing is vital for the generation of LULC maps which should be possible through a strategy called image classification. The goal of this research was to characterize and outline LULC of the study region utilizing RS and GIS technologies and furthermore to complete precision evaluation so as to survey how well classification functioned. The supervised classification was performed utilizing Non-Parametric Rule. The image was grouped into five classes; agriculture (54.33 km^2), water bodies (5.36 km^2), built-up land (6.53 km^2), forest land (2.56 km^2) and barren/waste land (29.49 km^2). The agriculture land was the prevailing kind of Land use, which covers about 55.28% of the total investigation. The likewise classified image should be evaluated for accuracy, before the equivalent could be utilized as the contribution for any applications. Individual accuracy assessment parameters are valuable to survey the model execution in regard to a specific classification/ class of specific interest for the study. In this investigation, the accuracy assessment was performed utilizing error matrix. The present study had an overall classification accuracy of 84% and kappa coefficient of 0.722. The kappa coefficient is evaluated as considerable and henceforth the grouped image observed to be fit for further research.

ACKNOWLEDGEMENT

Mr. M. Rajasekhar is thankful to the University Grants Commission (UGC), Government of India, New Delhi, for the financial support in the form of Fellowship (Grant No. 201718-RGNF-2017-18-SC- AND-37117).

Compliance with Ethical Standards

The authors declare that they have no conflict of interest and adhere to copyright norms.

REFERENCES

Areendran, G., Rao, P., Raj, K., Mazumdar, S. and Puri, K., 2013. Land use / land cover change dynamics analysis in mining areas of Singrauli district in Madhya Pradesh , India, 54(2), 239–250.

Pradeep Kumar, B., Raghu Babu, K., Rajasekhar, M., Ramachandra M., 2019. Assessment of land degradation and desertification due to migration of sand and sand dunes in Beluguppa Mandal of Anantapur district (AP, India), using remote sensing and GIS techniques. J. Ind. Geophys. Union. 23(2), 173-180.

Berberoglu, S. and Akin, A., 2009. International Journal of Applied Earth Observation and Geoinformation Assessing different remote sensing techniques to detect land use / cover changes in the eastern Mediterranean, 11, 46–53. https://doi.org/10.1016/j.jag.2008.06.002

Congalton, R.G., 1991. A review of assessing the accuracy of classifications of remotely sensed data. Remote Sensing of Environment, 37, 35-46. https://doi.org/10.1016/0034-4257 (91)90048-B

Dewan, A.M. and Yamaguchi, Y., 2016. Land use and land cover change in Greater Dhaka, Bangladesh: Using remote sensing to promote sustainable urbanization. Appl. Geography, 29(3), 390–401. https://doi.org/10.1016/j.apgeog.2008.12.005

Foody, G.M., 2002. Status of land cover classification accuracy assessment, 80, 185–201.

Jenness, J. and Wynne, J.J. (2007) Kappa Analysis (kappa_stats.avx) Extension for ArcView 3.x. Jenness Enterprises.
http://www.jennessent.com/arcview/kappa_stats.htm

Malaviya, S., Munsi, M., Oinam, G. and Kumar, P., 2010. Landscape approach for quantifying land use land cover change (1972 – 2006) and habitat diversity in a mining area in Central India (Bokaro , Jharkhand), 215–229. https://doi.org/10.1007/s10661-009-1227-8

Punia, M., Joshi, P.K. and Porwal, M.C., 2011. Expert Systems with Applications Decision tree classification of land use land cover for Delhi , India using IRS-P6 AWiFS data. Expert Systems With Applications, 38(5), 5577–5583. https://doi.org/10.1016/j.eswa.2010.10.078

Rajasekhar, M., Sudarsana Raju, G. Siddi Raju, R. and Imran Basha, U., 2017. Landuse and Landcover analysis using Remote Sensing and GIS : A case study in Uravakonda , Anantapur District , Andhra Pradesh , India. Int. Res. Journal of Engineering and Technology, 4(9), 780-785.

Rajasekhar, M., Sudarsana Raju, G., Siddi Raju, R. and Imran Basha, U., 2018a. Data on artificial recharge sites identified by geospatial tools in semi-arid region of

Anantapur District, Andhra Pradesh , India. Data in Brief. 19(2018), 462-474. https://doi.org/10.1016/j.dib.2018.04.050.

Rajasekhar, M., Sudarsana Raju G., Bramaiah, C., Deepthi, P., Amaravathi, Y. and Siddi Raju R., 2018b. Delineation of groundwater potential zones of semi-arid region of YSR Kadapa District, Andhra Pradesh, India using RS, GIS and Analytic Hierarchy Process. Remote Sensing of Land, 2(2), 76-86, 2018. http://dx.doi.org/10.21523/gcj1.18020201

Rajasekhar, M., Sudarsana Raju G, Siddi Raju R, Ramachandra M, and Pradeep Kumar B. 2018c. Data on comparative studies of lineaments extraction from ASTER DEM , SRTM, and Cartosat for Jilledubanderu River basin, Anantapur district, A.P , India by using remote sensing and GIS. Data in Brief, 20(2018), 1676–1682. https://doi.org/10.1016/j.dib.2018.09.023.

Rawat, J.S., 2015. Monitoring land use / cover change using remote sensing and GIS techniques : A case study of Hawalbagh block, district Almora, Uttarakhand, India. The Egyptian J. Rem. Sens. Space Sci., 18(1), 77–84. https://doi.org/10.1016/j.ejrs.2015.02.002

Rawat, J.S., Biswas, V. and Kumar, M., 2013. Changes in land use / cover using geospatial techniques : A case study of Ramnagar town area , district Nainital , Uttarakhand , India. The Egyptian J. Rem. Sens. Space Sci., 16(1), 111–117. https://doi.org/10.1016/j.ejrs.2013.04.002

Rogan, J. and Chen, D., 2004. Remote sensing technology for mapping and monitoring land-cover and land-use change. Progress in Planning, 61, 301–325. https://doi.org/10.1016/S0305-9006(03)00066-7

Rwanga, S.S. and Ndambuki, J.M., 2017. Accuracy assessment of land use / land cover classification using remote sensing and GIS, Int. Journal of Geosci., 8, 611-622.

Siddi Raju, R., Sudarsana Raju, G. and Rajasekhar, M., 2018. Land use / land cover change detection analysis using supervised classification , Remote Sensing and GIS In Mandavi River Basin , YSR, Kadapa District , Andhra Pradesh , India. J. Rem. Sens. and GIS, 9(3), 46–54.

Sreenivasulu, G., Jayaraju, N. and Lakshmi Prasad, T., 2014. Landuse and landcover analysis using remote sensing and GIS: A case study in and around Rajampet, Kadapa District, Andhra Pradesh, India. IJMRD 2015; 2(1), 186-191

Sudhakar, S., Srinivas, T., Palit, A., Kar, S.K. and Battacharya, S.K., 2006. Mapping of risk prone areas of kala-azar (Visceral leishmaniasis) in parts of Bihar state , India : an RS and GIS approach, (September). 43(3), 115-122.

Schull, M. and Turral, H., 2005. Ganges and Indus river basin land use / land cover (LULC) and irrigated area mapping using continuous streams of MODIS data, 95, 317–341. https://doi.org/10.1016/j.rse.2004.12.018

Thenkabail, P.S., Gangadhararao, P., Biggs, T.W., Krishna, M. and Turral, H., 2007. Spectral matching techniques to determine historical land-use / land-cover (LULC) and irrigated areas using time-series 0 . 1-degree AVHRR Pathfinder Datasets, (October).

Treitz, P. and Rogan, J., 2004. Remote sensing for mapping and monitoring land-cover and land-use change — an introduction, 61, 269–279. https://doi.org/10.1016/S0305-9006(03)00064-3

Wolch, J.R., Byrne, J. and Newell, J.P., 2014. Landscape and urban planning urban green space , public health , and environmental justice : The challenge of making cities ' just green enough.' Landscape and urban planning, 125, 234–244. https://doi.org/10.1016/j.landurbplan.2014.01.017

Yadav, P.K., Kapoor, M. and Sarma, K., 2012. Land use land cover mapping, Change detection and conflict analysis of Nagzira-Navegaon corridor , Central India using geospatial technology, 1(2), 90–98.

Fielding, A.H. and Bell, J.F., 1997. A review of methods for the assessment of pre-diction errors in conservation presence/absence models. Environmental Conservation, 24, 38-49. https://doi.org/10.1017/S0376892997000088.

Received on: 12.3.19; Revised on: 31.5.19; Accepted on: 6.6.19

Petrography of the quartz feldspar porphyry dyke from Patagundemgollapalle (Kadiri Mandal, Anantapur District), Andhra Pradesh, India

R. Maheswara rao, S. Srinivasa Gowd*, and G. Harish Vijay
Department of Geology, Yogi Vemana University, YSR Kadapa-516006, Andhra Pradesh
*Corresponding author: ssgowd@gmail.com

ABSTRACT

Quartz Feldspar Porphyry (QFP) occurs as a dyke body intruding into the granitoid country, located near Namala Gudi temple, on the way to Kadiri from Pulivendula. It runs for about 6-8 km in the NNE-SSW direction. It has phenocrysts of quartz and feldspars in a fine grained matrix of the same material. Due to the higher incidence of K-feldspar, the rock has more pink color. At Namalagudi area, this shows extensive brittle deformation. All along the strike, the features remain same, but not the brittle deformation. The quartz appears to have two populations, viz., phenocrysts – the average size is 5 mm (maximum 7 mm) with the ground mass containing grains of less than 0.1mm. The larger grains appear to have nucleation for the growth of the crystal and commonly contain melt inclusions and secondary fluid inclusions.

Key words: QFP, Phenocrysts, K-feldspar, Brittle deformation, Fluid inclusions.

INTRODUCTION

The QFP (Quartz feldspar porphyry) (Rose, 2007) dyke body is located in the topographical map of 57J/3 of Survey of India. It is covered between the 14º 18´ 48´´ and 14 º 20´ 20´´ North latitude and 78 º 10´ 21´´ and 78° 12´ 35´´ East longitude, there by covering nearly an area of about 12 km^2. This appears to be the first report of QFP occurring as dyke body in this area. The nearest township is Pulivendula of the Kadapa district. This granitoid terrain is traversed by number of basic dykes ranging in composition from olivine dolerite to normal dolerite. But there is the conspicuous Quartz Feldspar Porphyry (QFP), seen intruding into the granitoid terrain and further going below the sediments of the Cuddapah Super group, indicating that it is younger than the granitoids and older than the Cuddapah sediments, i.e., the Gulcheru Quartzite of the Papaghni Group. The dyke body occurs as strike ridge dipping steeply towards the west. The outcrop occurring near the temple Namalagudi, is the major one. It is located on the right side of the Pulivendula–Kadiri new road (SH–28). This outcrop runs nearly for about 1.75km in the NNE - SSW direction and has a height of 20 m. After 1.75 km, it occurs as discontinuous outcrops and runs further for about 1km in the SSW direction having a height less than 20 m. The third QFP is located south of the Vepalapalle village, where the outcrops have an almost east–west trend and runs for less than 500 m with a height of 20 m.

Petrologically, this rock consists of quartz and feldspar occurring as phenocrysts. The matrix is also of the same material but is of fine grained nature. Due to the higher incidence of K-feldspar, the rock has more pink color. On way to the village Subbanaguntapalle, the QFP has dark brown matrix with phenocrysts of feldspar. This is overlain by the pink variety of QFP. In addition, in the stream section, adjacent to the road on way to Subbanaguntapalle, there are a few outcrops of QFP with enclaves of green chloritic material. In addition, there are many dolerite dyke events that criss-cross the granitic terrain. In fact the basic dyke cuts the QFP, reflecting that the latter is the first event of dyking activity. The country rock is represented by peninsular gneiss in the southern part, intruded by younger various granitoid events in the northern part of the area under report. The event stratigraphy of the granitoids and the dyking activity has also been worked out. Quartz veins trending mainly east-west, represent the youngest phase of igneous activity.

GEOLOGICAL SETUP

Event stratigraphy of the granitoids (Early Units)

The country rock is mainly granitoid in nature. There

are nearly seven phases of granitic activity in this area, established mainly by the nature of occurrence in the form of xenoliths and cross cutting nature. The first two phases of granitoids, i.e., G_1 and G_2 (Figure 1a) are of mainly tonalitic in composition. The G_3 is medium to coarse grained and is more like granodiorite with higher incidence of plagioclase feldspar (Figure 1b). The mafic mineral is mostly hornblende and its incidence increases to make it as mesocratic at places, which can be seen in good number in hills. The G_4 is granitic in composition and can be called grey granite (Figure 1c). Compared to G_3, this is fine grained and has limited occurrence. The G_5 is fine grained pink granite that has intruded other granitoids (Figure 1d). Its end phase is pegmatoidal in nature and has impregnated the coarse grained pink feldspars in to the other granitoids. The G_6 is more like leucogranite with insignificant mafic minerals (Figure 1e). It is fine to medium grained and occupies the maximum area under the study. The entire western part of the study area is covered by this. The G_7 is the pegmatoidal event (Figure 1f), related to G_7. These may form the early units of the area (Javier Gil, 2010).

Dyking activity in the study area (late units)

All the dyke bodies when viewed in the satellite image, have similar spectral signatures, i.e., have similar tone and morphology (land form) – i.e., linear ridges, but slight difference in texture. Hence close and detailed field study is essential to record the differences between them. As mentioned before, the QFP forms one of the most interesting dyke body, hence forms the main aspect of the present study. The other dyke bodies are also studied. 5 dyking events have been identified by studying the cross cutting relation of the dykes. All the dyking events are considered as late units (Javier Gil, 2010).

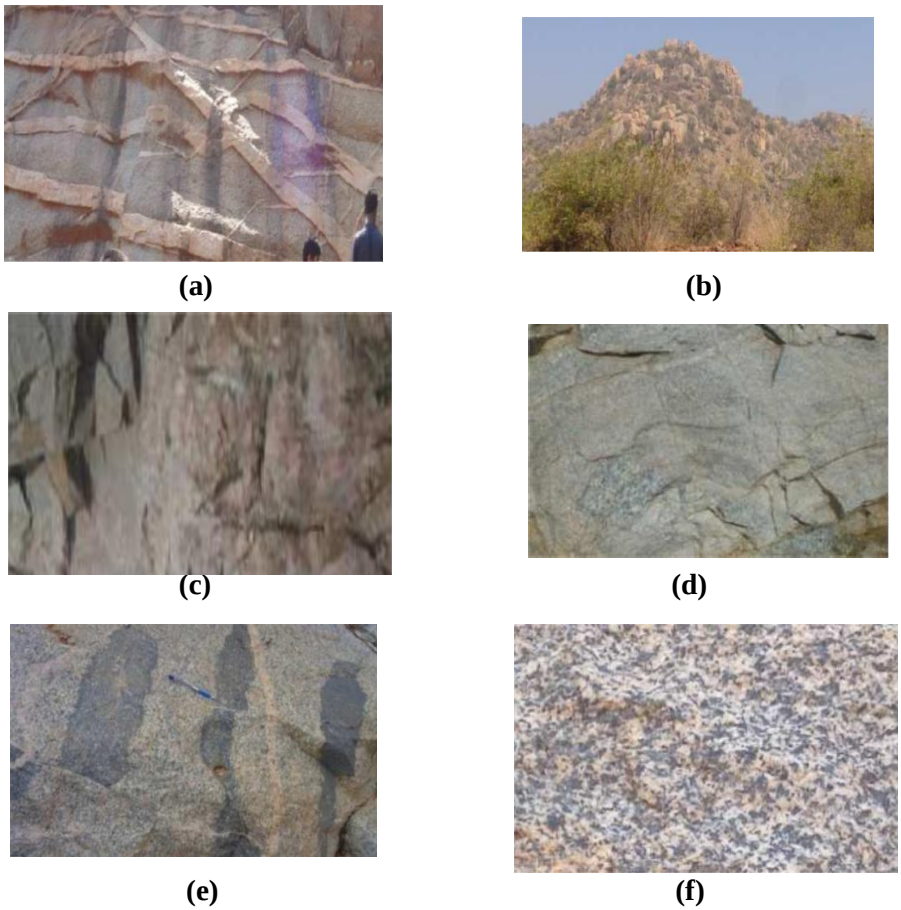

Figure 1. Event stratigraphy of the granitoids. (a) The youngest is the seventh phase G_7 is pegmatitic,

(b) The sixth phase G_6 is represented by leuco granite, (c) The fourth phase G_4 intrude by the fifth phase G_5, (d) The third phase G_3 as enclave in the fourth phase G_4, (e) The first phase, G_1 and G_2 in the third phase, G_3. (f) The close-up of the G_3

Quartz Feldspar Porphyry Dyke (QFP)

Based on the field evidence, i.e., cross cutting relationship between the dykes, the relative ages of the dyking episodes have been worked out. The dykes of Quartz - Feldspar Porphyry (QFP) are considered to be of the first episode. (Dy1). Further, the 5 phases of dyking activity can be seen in the area through the Google Earth satellite image (Figure 2).

The QFP has intruded into the country rock that is a granitoid. (Figure 3) The contact between the QFP and the country rock near the temple is marked by a brittle shear zone. It trends NNE-SSW and the rock is highly shattered. The contact also shows fine grained nature of QFP, reflecting the contact effect.

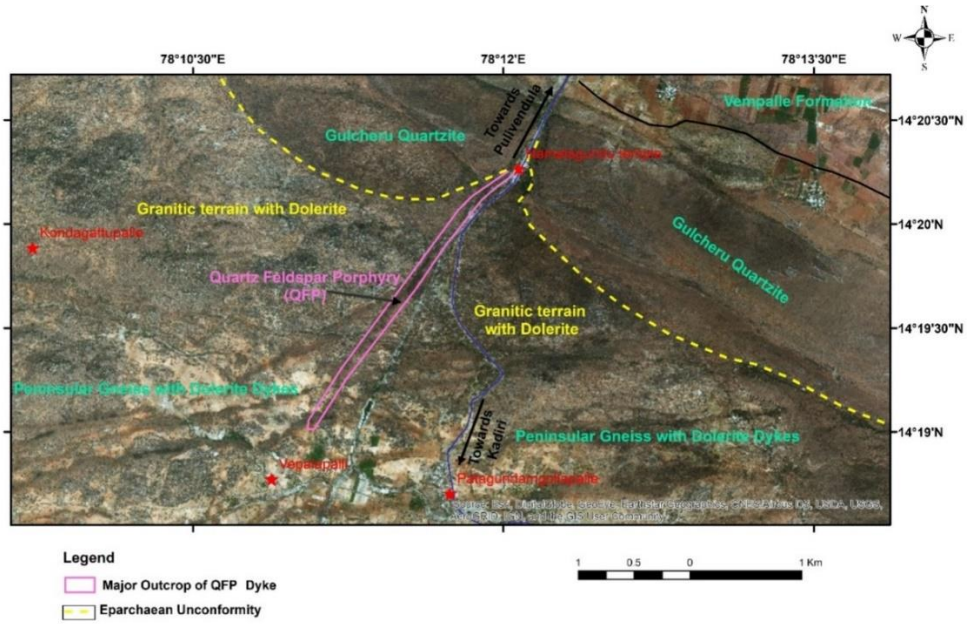

Figure 2. Study area showing QFP and other field details on Google Earth Image.

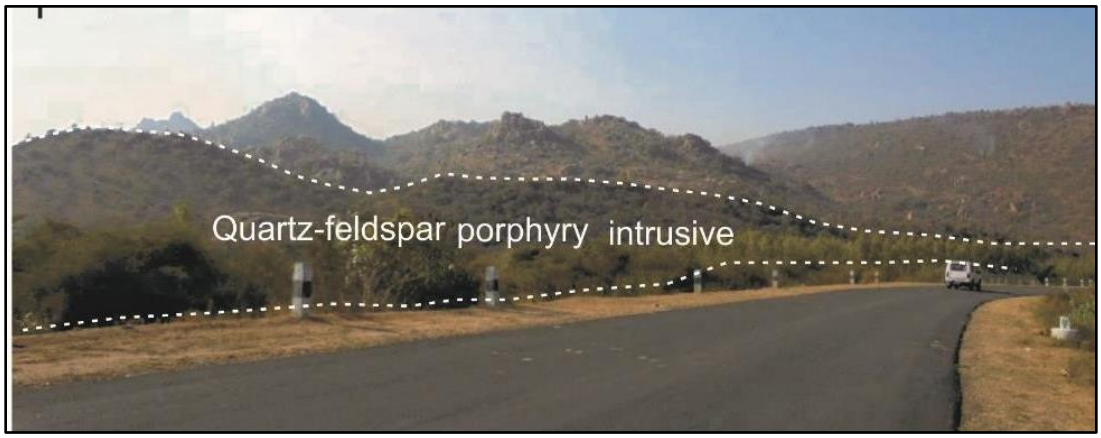

Figure 3. The field set up of the QFP (Dy1).

MEGASCOPIC CHARACTERISTICS

Near the temple Namalagudi area, the porphyry has flesh red color with the porphyries of K- feldspar, quartz and plagioclase feldspar (Figure 4). The matrix is fine to medium grained and is also pink in color, indicating the presence of fine to medium grained k-feldspar. The quartz appears to have two populations of phenocrysts (Figure 4) and the average size is 5 mm with the ground mass containing grains of less than 0.1mm. The larger grains measure up to 7mm and appear to have nucleation for the growth of the crystal. The quartz grains are sub-rounded (Leonard et al., 2005).

In the photograph (Figure 4) the quartz reflects half white color, whereas the K-feldspar reflects pink to light pink color. Matrix also varies from light pink to deep pink. The matrix at few places, that is seen at the lower of the hills of QFP, is fine grained and greenish material with phenocrysts and of quartz and feldspar, the later invariably show nuclei. There are phenocrysts that show sub-hedral to euhedral shape and the phenoclasts are mostly anhedral with angular fragments (Figure 5). There are a few feldspar crystals that show dark colored nuclei (Figure 5). This is seen on way to the village Subbanaguntapalle (Figure 5), where it is overlain by the pink variety of QFP (Figure 4). In addition in the stream section, adjacent to the road on way to Subbanaguntapalle, there are a few outcrops of QFP with enclaves of green chloritic material.

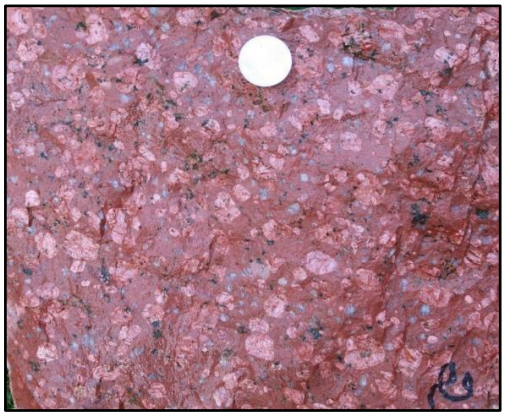

Figure 4. Megascopic features of QFP. (Field Feature).

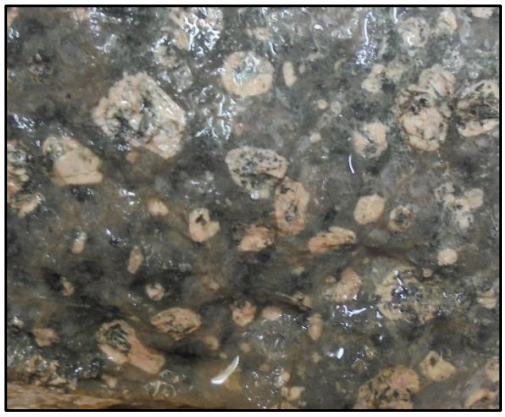

Figure 5. A variety of QFP with greenish grey matrix (Field Feature).

MICROSCOPIC CHARACTERISTICS

Mineralogy

Amongst the major minerals quartz and feldspar form the major constituents. Anhedral quartz and anhedral to subhedral feldspar phenocrysts constitute major percentage in a thin section. Sub-rounded to rounded quartz is seen as phenocrysts, with a groundmass consisting of grains <0.1mm in size (Figure 6a-c). The minerals appear to have grown around a black colored nucleus. Similar views were expressed by Leonard et al., (2005).

Further, two populations of quartz is seen, (i) a large subhedral quartz phenoclasts in contact with smaller numerous quartz grains,and (ii) a large phenocryst with melt and fluid inclusions, where the surrounding melt was seen trapped by the growing quartz along the grain boundary (Leonardetal., 2005). These features are reflected in the Photomicrographs (Figures 7a-b). Feldspars are present in major proportions in every sample, but have undergone extensive serisitization. Orthoclase phenocrysts are frequently glomeroporphyritic and form clusters of numerous crystals (Figure 8). Inclusions of aggregates of opaques and titanite (?) are found in the cores of many orthoclase crystals (Leonard et al., 2005).

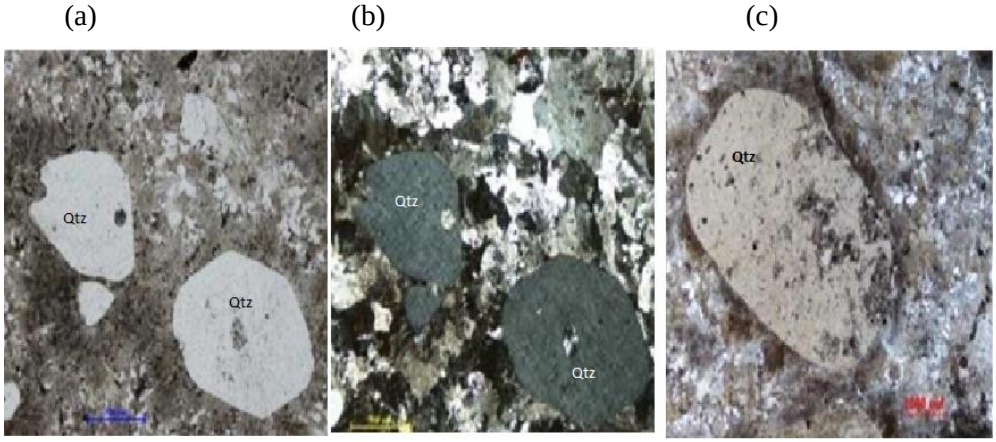

Figure 6. Photomicrographs showing euhedral and subhedral quartz (Qtz), with secondary fluid inclusions. The subhedral quartz reflects that they are corroded and sorbed (Figures a,b) (a) Under polarized light, (b) under crossed nicols, (c) Under crossed nicols.

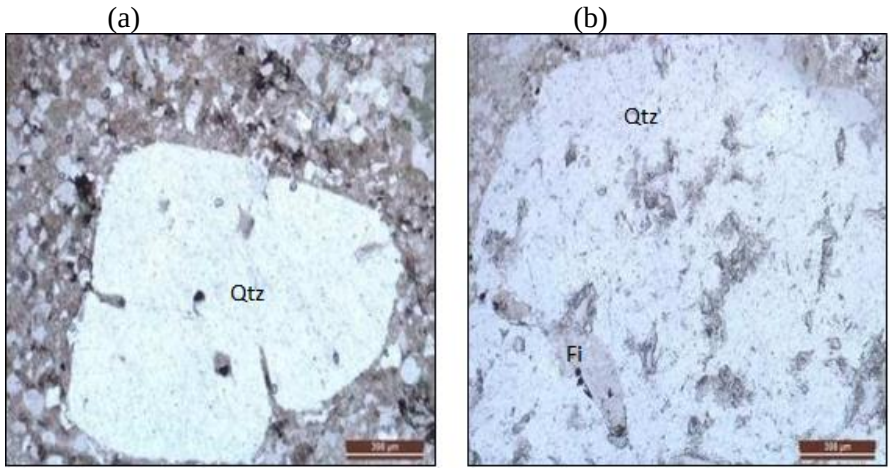

Figure 7. (a) Photomicrographs reflecting large subhedral quartz Phenocryst in contact with smaller numerous quartz grains, (b) Photomicrographs showing a large phenocryst with melt and fluid inclusions (Fi).

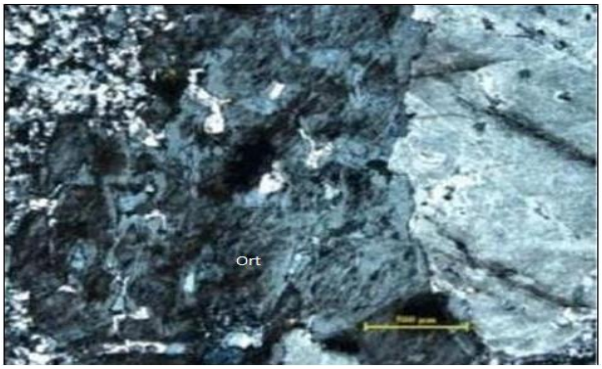

Figure 8. Photomicrograph reflecting the Glameroporphyritic orthoclase (Ort) (form of clusters of numerous crystals) - Under crossed nicols.

Groundmass / Matrix

The ground mass is constituted mainly by the quartz and feldspar of minor size and are mostly subhedral to euhedral, as observed in the figures (6) to (9). Inclusions of apatite, zircon, chlorite, Fe- sulphide and rutile are observed (Figure 9a-9f). The dyke's groundmass mineralogy generally consists of fine

grained quartz, plagioclase and orthoclase with accessory biotite, chlorite, muscovite, pyrite, and calcite, and rutile, ilmenite. Chlorite appears to be local alteration product of reddish brown biotite. Chlorite is associated with calcite and arrow calcite veins occupy micro fractures, suggesting late paragenesis. Individual calcite grains contain pyrite inclusions (Leonard et al., 2005).

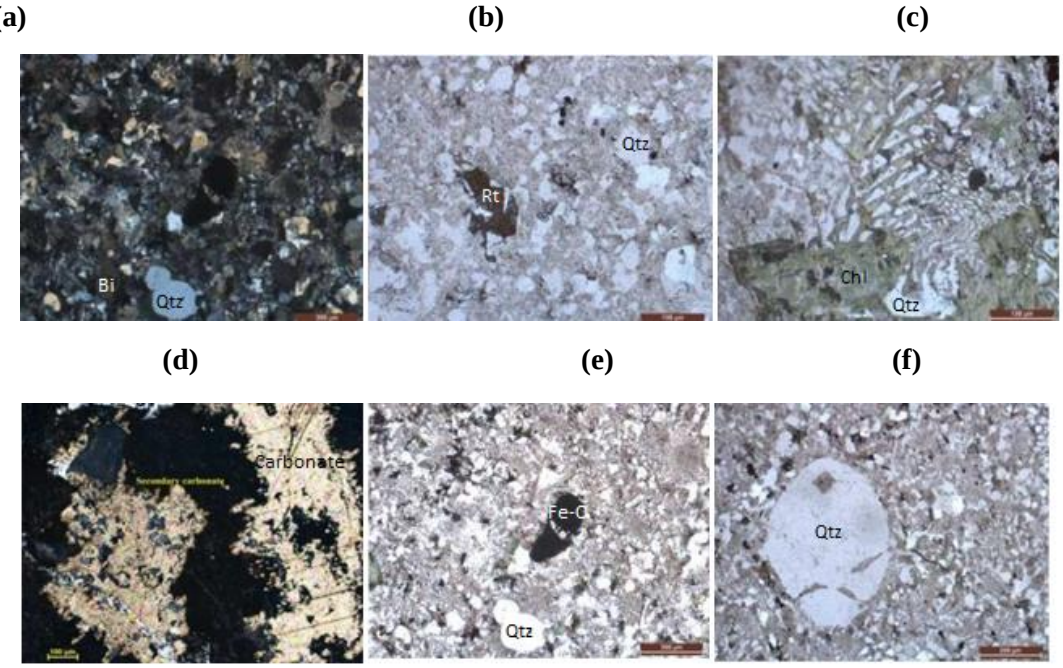

Figure 9. Photomicrographs of Quartz Feldspar Porphyry. (a) Biotite (Bi) with other accessories, (b) Rutile (Rt) with other accessories, (c) Chlorite (Chl) with other accessories, (d) Carbonate with other accessories, (e) Fe-oxide (Fe-O) with other accessories, (f) Quartz (Qtz) with melt-inclusions

Texture

The study of textures is essential to understand the history of cooling and solidification (Bryon et al 1995). The Quartz Feldspar Porphyry exhibits resorbed quartz phenocrysts, graphic texture and granophyric textures (Streckinson, 1974; Vernon, 2018). Resorbed texture is very well reflected by the quartz phenocrysts (Figure 10). The margins of the clasts / crystals are affected by the residual liquid, resulting in the formation of dents in the outline of the mineral**.** Graphic or runic intergrowth between quartz and feldspar (Leonard et al., 2005) is very conspicuous in almost all the thin sections (Figure 11). Granophyric intergrowth between quartz and feldspar is also seen in almost all the thin sections (Figure 12).

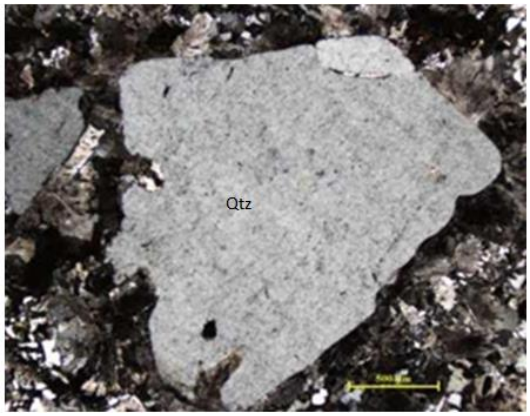

Figure 10. Photomicrographs showing resorbed quartz phenocryst.

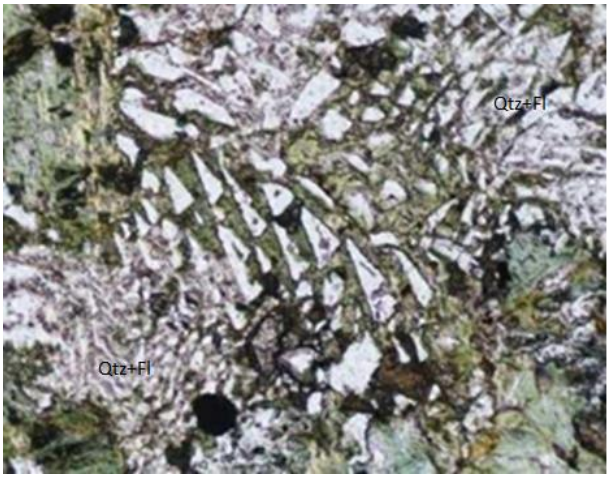

Figure 11. Photomicrograph showing graphic or runic intergrowth between quartz (Qtz) and feldspar (Fl).

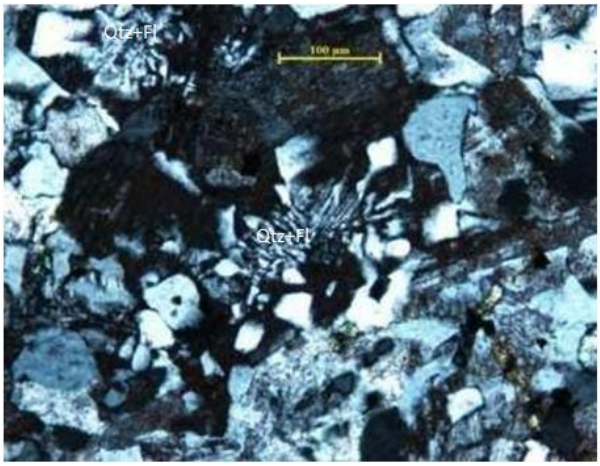

Figure 12. Photomicrograph showing granophyric intergrowth between quartz (Qtz) and feldspar (Fl).

CONCLUSIONS

The study of the QFP has led to the following conclusions.

(i) It is a unique rock in the local geological set up.
(ii) There are seven events of the granitoid activity that can be recognized as early units.
(iii) Intruding the granitoids is the QFP, that has very clear reflection of porphyritic nature and it is seen as a first phase of intrusive into the granitoid country. In addition to this, there are nearly four phases of basic intrusives that could be identified by the crosscutting relation in the field. These are recognized as late units.
(iv) The phenocrysts are K-feldspar, quartz and plagioclase feldspar. Quartz has two populations, viz., the smaller and the bigger. The main outcrop is pink in color with the matrix reflecting light pink to pink color indicating the same composition, (higher incidence of k-feldspar) but finer in grain size.
(v) Another variety of QFP, with dark grey matrix and phenocrysts of plagioclase feldspar is noticed occurring below the pink variety. The phenocrysts have dark colored nucleus.
(vi) Fluid inclusions are seen in almost all phenocrysts. Texturally, this rock exhibits glameroporphyritic K-feldspar and graphic and granophyric intergrowths between quartz and alkali feldspar are also seen extensively.

ACKNOWLEDGEMENTS

The authors express their sincere thanks to the reviewers for their valuable comments towards improving the quality of the manuscript. We are also grateful to the Chief Editor of JIGU for useful suggestions and appropriate editing.

Compliance with Ethical Standards

The authors declare that they have no conflict of interest and adhere to copyright norms.

REFERENCES

Bryon, D.N., Atherton, M.P. and Hunter. R.H., 1995. The interpretation of granitic textures from serial thin sectioning, image analysis and three-dimensional reconstruction. Mineralogical Magazine, 59, 203-211.

Javier Gil–Rodriguez., 2010. Igneous petrology of the Colosagold-rich porphyry system (Tolima, Colombia), Department of Geosciences, University of Arizona.

Leonard, P.R.R., Lentz, D.R. and Poujol, M., 2005. Petrology, geochemistry, and U- Pb (zircon) age of the quartz-feldspar porphyry dyke at the Lake George antimony mine, New Brunswick: implications for origin, emplacement process, and mineralization, Atlan. Geol., 42, 1-14.

Rose, W.I., 2007. Porphyry. In McGrew Hill Encyclopedia of science and technology, 10th Edition. Mc.Graw-Hill., 14, 254-255.

Strckeisen, A.L., 1974. Classification and nomenclature of Plutonic rocks. Geol. Rundschau, 63, 773-786.

Vernon, R.H., 2018. A practical guide to rock microstructures Macquarie University, Sydney.

Received on: 8.3.19; Revised on: 17.5.19; Accepted on: 26.5.19

GUIDE FOR AUTHORS

The Journal of Indian Geophysical Union (J-IGU), published bimonthly by the Indian Geophysical Union (IGU), is an interdisciplinary journal from India that publishes high-quality research in earth sciences with special emphasis on the topics pertaining to the Indian subcontinent and the surrounding Indian Ocean region. The journal covers several scientific disciplines related to the Earth sciences such as solid Earth geophysics, geology and geochemistry, apart from marine, atmosphere, space and planetary sciences. J-IGU welcomes contributions under the following categories:

- Research papers and short notes reporting new findings.
- Review articles providing comprehensive overview of a significant research field.

In addition, J-IGU also welcomes short communications, after communications and report on scientific activity, book reviews, news and views, etc.

The manuscript should be submitted electronically as a single word format (.doc file) including the main text, figures, tables, and any other supplementary information along with the signed "Declaration Letter". The manuscript should be submitted by email (jigu1963@gmail.com) to the Chief Editor.

After acceptance of the manuscript the corresponding author would be required to submit all source files (text and Tables in word format) and figures in high resolution standard (*.jpg, *.tiff, *.bmp) format. These files may be submitted to J-IGU as a single *.zip file along with the "Copyright Transfer Statement".

IMPORTANT INFORMATION

Ethics in publishing
J-IGU is committed to ensuring ethics in publication and takes a serious view of plagiarism including self-plagiarism in manuscripts submitted to the journal. Authors are advised to ensure ethical values by submitting only their original work and due acknowledgement to the work of others used in the manuscript. Authors must also refrain from submitting the same manuscript to more than one journal concurrently, or publish the same piece of research work in more than one journal, which is unethical and unacceptable. Editor of J-IGU is committed to make every reasonable effort to investigate any allegations of plagiarism brought to his attention, as well as instances that come up during the peer review process and has full authority to retract any plagiarized publication from the journal and take appropriate action against such authors if it is proven that such a misconduct was intentional.

Similarly, Editor and Reviewers are also expected to follow ethical norms of publishing by ensuring that they don't use any unpublished information, communicated to them for editorial or review purpose, in their own research without the explicit written consent of the author. They are also expected to keep manuscript/ data/ observations/ any other information related to the peer review confidential to protect the interest of the authors. Reviewers should refrain from reviewing the manuscripts in which they have conflicts of interest resulting from competitive, collaborative, or other relationships or connections with any of the authors, companies, or institutions connected to the manuscript.

Conflict of interest
All authors are requested to disclose any actual or potential conflict of interest including any financial, personal or other relationships with other people or organizations within three years of beginning the submitted work that could inappropriately influence, or be perceived to influence, their work.

Submission declaration
Submission of a manuscript implies that the work has not been published previously and it is not under consideration for publication elsewhere, and that if accepted it will not be published elsewhere in the same or any other form, in English or in any other language, without the written consent of the publisher. It also implies that the authors have taken necessary approval from the competent authority of the institute/organization where the work was carried out.

Copyright
After acceptance of the manuscript the corresponding author would be required to sign and submit the "Copyright Transfer Statement".

MANUSCRIPT PREPARATION

The corresponding author should be identified (include E-mail address, Phone/Mobile number). Full affiliation and postal address must be given for all co-authors.

Abstract:
An abstract of not more than 300 words must be included.

Text:
The manuscript should be structured to include a front page containing the title, Author(s) name, affiliation and address of the institute, where the work was carried out, a short title, and 5-to-6 Key words. Author(s) present address, if different from the above mentioned address, may be given in the footnote. The corresponding author should be identified with an asterisk and his/her email ID should be provided. This page should be followed by the main text consisting of Abstract, Introduction, Methods/ Techniques/ Area description, Results, Discussion, Conclusions, Acknowledgements, and References. Tables and Figures with captions should be inserted at the end of main text. It should not be inserted in the body of the text.

Figures/ Illustrations:
All figures should be provided in camera-ready form, suitable for reproduction (which may include reduction) without retouching. Figures in high-resolution (at least 300 dpi) standard formats (*.jpg, *.tiff, *.bmp) are acceptable. Figures should be numbered according to their sequence in the text. References should be made in the text to each figure. Each figure should have a suitable caption.

Tables:
Authors should take note of the limitations set by the size and layout of the journal. Table should not exceed the printed area of the page. They should be typed on separate sheets and details about the tables should be given in the text. Heading should be brief. Large tables should be avoided and may be provided as supplementary information, if required.

Equations:
Equations should be numbered sequentially with Arabic numerals and cited in the text. Subscripts and Superscripts should be set off clearly. Equation writing software that presents each equation as an object in MS Word will be accepted. Style and convention adopted for the equations should be uniform throughout the paper.

References:
All references to publications cited in the main text should be presented as a list of references in order following the text and all references in the list must be cited in the text. References should be arranged chronologically, in the text. The list of references should be arranged alphabetically at the end of the paper.

References should be given in the following form:
Kaila, K.L., Reddy P.R., Mall D.M., Venkateswarlu, N., Krishna V.G. and Prasad, A.S.S.S.R.S., 1992. Crustal structure of the west Bengal Basin from deep seismic sounding investigations. Geophys. J. Int., 111,45-66.

REVIEW PROCESS:

All manuscripts submitted to the journal are peer-reviewed. It is advisable to send the contact details of 4 potential reviewers along with the manuscript to expedite the review process. Editor has the option to select reviewers from the list or choose different reviewers. The review process usually takes about 3 months. All enquiries regarding the manuscript may be addressed to the Editor.

GALLEY PROOF:

Technical editing of manuscripts is performed by the editorial board. The author is asked to check the galley proof for typographical errors and to answer queries from the editor. Authors are requested to return the corrected proof within two days of its receipt to ensure uninterrupted processing. The editor will not accept new material in proof unless permission from the editorial board has been obtained for the addition of a "note added in proof". Authors are liable for the cost of excessive alterations to galley proof.

PUBLICATION CHARGES:

There are no page charges for publication and printing charges for b/w figures. However, in view of substantial cost involved in printing of color figures, author will be charged for printing of pages containing color figures @ Rs. 2,500/- per page. The charges may be revised at any time based on cost of printing and production. Author will receive an estimate/ invoice of the color figures reproduction cost along with the galley proof. It is the responsibility of the author to remit the color figures reproduction cost within one month of the receipt of the estimate/invoice.

The corresponding author will receive a soft copy (pdf format) of his/her published article. Should the author desire to purchase reprints of his/her publication, he/she must send the duly signed Reprint Order Form (accompanies the galley proof and contains price details) along with the corrected galley proof to the Editor. The reprint charges must be paid within one month of sending the Reprint Order Form.

Any payment related to printing of color figures and/or purchase of reprints should be made in the form of a Demand Draft in the name of Treasurer, Indian Geophysical Union, payable at Hyderabad.

You may download the pdf file from: http://www.j-igu.in/IGU-Guide-forAuthors.pdf